# ANALYSIS AND VERIFICATION OF A PYROSHOCK TEST SYSTEM

A THESIS SUBMITTED TO
THE GRADUATE SCHOOL OF NATURAL AND APPLIED SCIENCES
OF
MIDDLE EAST TECHNICAL UNIVERSITY

BY

ANIL İSMAİL KÜÇÜKBAYRAM

IN PARTIAL FULFILLMENT OF THE REQUIREMENTS
FOR
THE DEGREE OF MASTER OF SCIENCE
IN
MECHANICAL ENGINEERING

FEBRUARY 2021

Approval of the thesis:

**ANALYSIS AND VERIFICATION OF A PYROSHOCK TEST SYSTEM**

submitted by **ANIL İSMAİL KÜÇÜKBAYRAM** in partial fulfillment of the requirements for the degree of **Master of Science** i**n Mechanical Engineering, Middle East Technical University** by,

Prof. Dr. Halil Kalıpçılar
Dean, Graduate School of **Natural and Applied Sciences** _____

Prof. Dr. M. A. Sahir Arıkan
Head of the Department, **Mechanical Engineering** _____

Assoc. Prof. Dr. Mehmet Bülent Özer
Supervisor, **Mechanical Engineering, METU** _____

**Examining Committee Members:**

Assoc. Prof. Dr. Yiğit Yazıcıoğlu
Mechanical Engineering, METU _____

Assoc. Prof. Dr. Mehmet Bülent Özer
Mechanical Engineering, METU _____

Assist. Prof. Dr. Gökhan Osman Özgen
Mechanical Engineering, METU _____

Assist. Prof. Dr. Orkun Özşahin
Mechanical Engineering, METU _____

Assoc. Prof. Dr. Selahittin Çağlar Başlamışlı
Mechanical Engineering, Hacettepe University _____

Date: 03.02.2021

**I hereby declare that all information in this document has been obtained and presented in accordance with academic rules and ethical conduct. I also declare that, as required by these rules and conduct, I have fully cited and referenced all material and results that are not original to this work.**

Name, Last name : Anıl İsmail Küçükbayram

Signature :

# ABSTRACT

## ANALYSIS AND VERIFICATION OF A PYROSHOCK TEST SYSTEM

Küçükbayram, Anıl İsmail
Master of Science, Mechanical Engineering
Supervisor : Assoc. Prof. Dr. Mehmet Bülent Özer

February 2021, 121 pages

In the aerospace industry, systems, subsystems, and units are exposed to explosive events during their lifecycle. Any explosive event creates shock in the structure, and it propagates until it is damped. This shock wave may be hazardous for some electronic and optical components. It may damage a component and cause failure in the equipment. For this reason, satellite equipment has to be qualified to withstand all static and dynamic loads encountered during launch and operational life. Thus, one of the challenging tests in the qualification process is the pyroshock test, which is performed on aerospace structures to ensure equipment functionality and integrity against shock load. There are several methods to perform a pyroshock test. The commonly used method is by mechanical impact. A resonant plate is excited by a hammer, and shock waves propagate through the plate. This type of test system is suitable for testing space equipment that will be exposed to mid-field and far-field shock. Test system configuration parameters such as plate thickness, mass, geometry, etc., are adjusted to obtain an appropriate Shock Response Spectrum (SRS) profile. Some of these parameters are less effective, and some are highly effective in obtaining the desired shock profile. The test operator has to perform long trials with the dummy model to obtain the target test profile. In order to minimize this preparation time, the effects of the configuration parameters must be well

known. Therefore, this study was started by analyzing the effect of configuration parameters on the SRS profile in ABAQUS/Explicit finite element software. The requested SRS profile for testing is predicted by optimizing configuration parameters in the analysis. In this manner, it is aimed to complete the profile fitting process performed on the dummy model in a much shorter time. In this study, measurement, and characterization of pyroshock test system, requirements for various experimental simulations, resonant plate excitation and measurement techniques, data acquisition, and an overview of numerical simulation are reviewed. The developed components of the shock test system and the corresponding finite element model are experimentally validated. The shock tests are simulated using ABAQUS/Explicit finite element software. As a result of this research, an accurate finite element modeling technique for future shock test simulation and prediction of test results was developed.

Keywords: Pyroshock Simulation, Shock Response Spectrum, Impact Force Profile, Shock Testing, Space Equipment.

# ÖZ

## PİROŞOK TEST SİSTEMİNİN ANALİZİ VE DOĞRULANMASI

Küçükbayram, Anıl İsmail
Yüksek Lisans, Makina Mühendisliği
Tez Yöneticisi: Doç. Dr. Mehmet Bülent Özer

Şubat 2021, 121 sayfa

Havacılık ve uzay endüstrisinde sistemler, alt sistemler ve birimler hizmet ömrü boyunca patlayıcılı olaylara maruz kalır. Herhangi bir patlayıcı olay yapıda şok yaratır ve sönümlenene kadar yayılır. Bu şok dalgası, bazı elektronik ve optik bileşenler için tehlikeli olabilmektedir. Bir bileşene zarar verebilir ve ekipmanda arızaya neden olabilir. Bu sebeple uydu ekipmanı, fırlatma ve operasyonel ömrü boyunca karşılaşılan tüm statik ve dinamik yüklere dayanacak şekilde kalifiye edilmelidir. Bu nedenle yeterlilik sürecindeki zorlu testlerden birisi de piroşok testidir. Havacılık ve uzay endüstrisinde, ekipmanın şok yüküne karşı bütünlüğünü ve işlevselliğinin sağlandığını göstermek amacıyla gerçekleştirilir. Piroşok testi birkaç yöntemle yapılabilir. Yaygın olarak kullanılan yöntem mekanik çarpmadır. Bir rezonant plakaya bir çekiç çarptırılır ve şok dalgaları plakanın içinde yayılır. Bu tip test sistemi, orta ve uzak alan şokuna maruz kalacak uzay ekipmanlarının test edilmesi için uygundur. Test sisteminde, uygun bir Shock Response Spectrum (SRS) profili elde etmek için plaka kalınlığı, kütle, geometri vb. gibi test sistemi konfigürasyon parametreleri ayarlanır. Bu parametrelerin bazıları daha az etkilidir ve bazıları da istenilen şok profilini elde etmede çok etkilidir. Test operatörü, hedeflenen test profilini elde etmek için kukla modelle uzun denemeler yapması

gerekir. Bu hazırlık süresini en aza indirmek için konfigürasyon parametrelerinin etkilerinin iyi bilinmesi gerekir. Bu çalışma, konfigürasyon parametrelerinin SRS profillerine etkisi ABAQUS/ Explicit sonlu elemanlar yazılımında analiz edilerek başlamıştır. Test için istenen SRS profili, analizdeki konfigürasyon parametrelerinin optimize edilmesiyle tahmin edilir. Böylelikle kukla model ile yapılan profil ayarlama işleminin çok daha kısa sürede tamamlanması hedeflenmektedir. Bu çalışmada, piroşok test sisteminin ölçümü ve karakterizasyonu, çeşitli deneysel simülasyonlar için gereksinimler, rezonant plakayı uyarma ve ölçüm teknikleri, veri toplama ve sayısal simülasyona genel bir bakış gözden geçirilmiştir. Şok test sisteminin geliştirilen bileşenleri ve ilgili sonlu elemanlar modeli deneysel olarak doğrulanmıştır. Şok testleri ABAQUS/Explicit sonlu eleman yazılımı kullanılarak simüle edilmiştir. Bu araştırmanın bir sonucu olarak, gelecekteki şok testi simülasyonu ve test sonuçlarının tahmini için doğru sonuç veren bir sonlu eleman modelleme tekniği geliştirilmiştir.

Anahtar Kelimeler: Piroşok Simülasyonu, Shock Response Spectrum, Çarpma Kuvvet Profili, Şok Testi, Uzay Ekipmanı.

*To my family*

## ACKNOWLEDGMENTS

I would like to express my sincere appreciation to my supervisor, Assoc. Prof. Dr. Mehmet Bülent Özer, for his unique guidance and continuous support during my M.Sc. The door to his office was always open whenever I ran into a trouble spot or had a question about my research.

The physical and technical contribution of 'TUBITAK Space Technologies Research Institute' is truly appreciated. Without their support, this study could not have reached its goal.

I would like to thank Bilal Atar, Mert İşler, Metin Biçer, and Muhammed Çakır for their irreplaceable friendship, assistance, and guidance. I am also grateful to Bekir Solak, Emre Gavuz, Dr. Osman Akkoyunlu and Yavuz Selim Sancaktar for their contributions to my studies, in addition to their marvelous companionship.

Finally, I would like to acknowledge the support and great love of my family, my mother, Yasemin; my father, Ekrem; and my sister, Şevval. They kept me going on, and this work would not have been possible without their input. Thank you.

## TABLE OF CONTENTS

## LIST OF TABLES

TABLES

## LIST OF FIGURES

FIGURES

## LIST OF ABBREVIATIONS

ABBREVIATIONS

DOF : Degree of Freedom

ECSS : European Cooperation for Space Standardization

EKP : Estimated Knee Point

ESA : European Space Agency

FE : Finite Element

FEA : Finite Element Analysis

FEM : Finite Element Method

FMT : Force Measurement Test

FRF : Frequency Response Function

IP : In-Plane

N/A : Not Applicable

NASA : National Aeronautics and Space Administration

OOP : Out-Of-Plane

PCB : Printed Circuit Board

SDOF : Single Degree of Freedom

SRS : Shock Response Spectrum

## LIST OF SYMBOLS

SYMBOLS

$c$ : Damping coefficient

$c_f$ : Flexural wave speed

$E$ : Modulus of elasticity in tension and compression (Young's modulus)

$f$ : Frequency

$g$ : Acceleration of gravity

$G$ : Modulus of elasticity in shear

Hz : Hertz

$k$ : Spring constant, stiffness

$m$ : Mass

$Q$ : Quality factor

$t$ : Time

$\zeta$ : Damping ratio

$\lambda$ : Wavelength

$\rho$ : Mass density

# CHAPTER 1

# INTRODUCTION

Aerospace is an important field of engineering and technology that enables us to understand the world beyond our earth. With the developments in this field, communication, transportation, media, climate forecasts, positioning systems, and new scientific developments have enormously changed human beings' daily lives. Aerospace structures face numerous and serious loads from the challenging launch environment to the severe space environment throughout their service life, as shown in Figure 1.1. Vibration and acoustic loads from rocket engines during the launch environment and pyroshock loads caused by the separation of stages and fairings make space structures very challenging in their design phase. After the launch, satellites and spacecraft continue their journeys in difficult space circumstances with vacuum, radiation, high-temperature differences, and space debris. Besides, thrust systems and deployment mechanisms in orbit are also sources of a shock for spacecraft. Therefore, systems have to be designed sufficiently strong considering the launch and the shock conditions. On the other hand, structures should be as light as possible for the minimization of the launch cost. These conflicting requirements make the design of space structures challenging and increase the importance of avoiding overly designed structures.

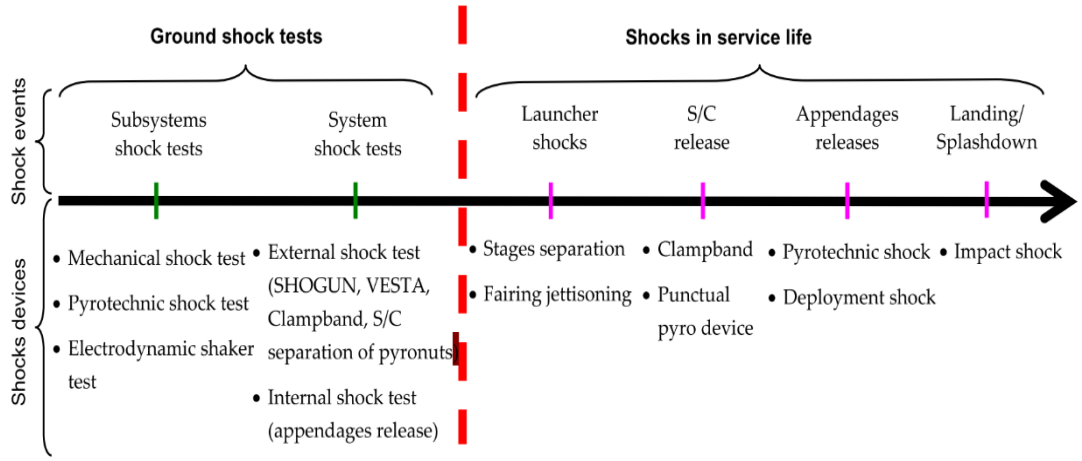


Figure 1.1. Shock events in the spacecraft project [1]

Developed units have to complete various environmental tests to be qualified. One of the environmental tests in the category of a dynamic test is the pyroshock test. Shock loads from the pyrotechnical valves and fasteners are simulated with this test. The unit under test is subjected to shock load transiently, and the resulting stress waves are reflected, refracted, and dissipated as they progress through the structure. As a result of pyroshock load, fragile and sensitive components may be damaged [1, Ch. 17.5].

The shock environment is typically categorized in three fields [1]. These are near-field, mid-field, and far-field shocks. The difference between these classifications is based on the shock magnitude and its spectral composition.

- Near-field: The near-field environment is dominated by direct stress wave propagation from the source. Maximum frequency content extending beyond 100 kHz and peak amplitudes greater than 5,000 g. The near-field usually includes structural locations within approximately 15 cm of the source. Shock-sensitive hardware should not be mounted in this environment.

- Mid-field: The mid-field environment is characterized by a combination of wave propagation and structural resonances. Maximum frequency is above 10,000 Hz and peak amplitudes between 1,000 and 5000 g.

- Far-field: Structural resonances dominate the far-field environment. The Maximum frequency is less than 10,000 Hz, and peak amplitudes less than 2,000 g.

The simulation of the pyroshock can be performed using different test methods. The appropriate method is decided according to the qualification level requirement.

- Pyroshock test by pyrotechnic device: The pyrotechnic shock test method is carried out using a pyrotechnic detonator. The test item is subjected to the shock load by activating the detonator, which is mounted on the back of a fixture. With the pyrotechnic test method, near field shock simulation is usually performed. This test method is suitable when a high shock level is required.

- Pyroshock test by mechanical impact: Shock is generated by applying mechanical impact on the resonant structure. The impact can be performed using dropping mass, pendulum, or projectile (pneumatic piston, cannon, or powder-actuated tool) systems. With the mechanical impact test methods, mid-field and far-field shock simulations are performed.

The most common pyroshock simulation method is excitation with mechanical impact. In this study, the pneumatic and pendulum type test systems are used in experimental studies, and the pneumatic type is shown in Figure 1.3. Basically, a resonant plate is excited by a hammer in a barrel, and waves propagate through the plate. Detailed information about the test systems used in this study is given in Section 4.2.1.1. Consequently, acceleration responses that occur according to the modal characteristics of the plate are measured. This type of test system is suitable for generating pyroshock load, which is similar to aerospace pyro-equipment.

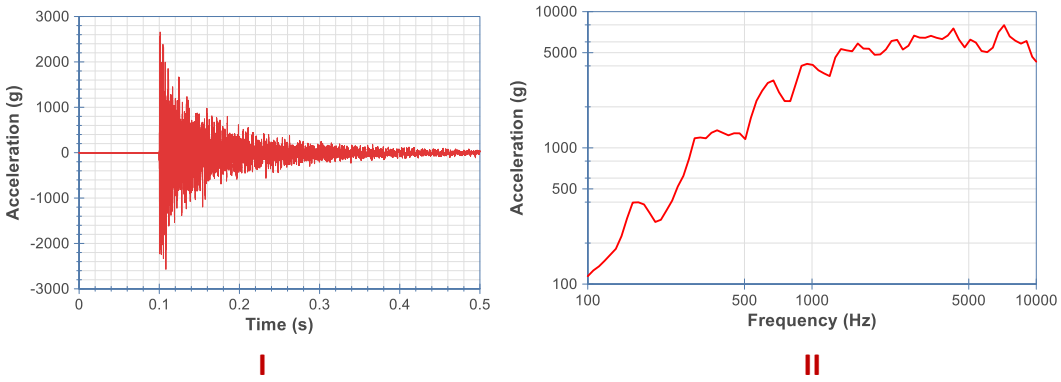


Figure 1.2. Sample pyroshock test data (I: Acceleration time history, II: Shock response spectrum)

The time-domain measurement of a shock signal is not beneficial directly for engineering purposes as it lacks information about the frequency contents of the shock. It cannot be used to compare the maximum response of the structure to which the shock is applied and similar shock pulses. Thus, the transformation to another form is then required. The Shock Response Spectrum (SRS) is useful for shock representation and comparison used by engineers, as shown in Figure 1.2. It shows the acceleration level corresponding to each frequency.

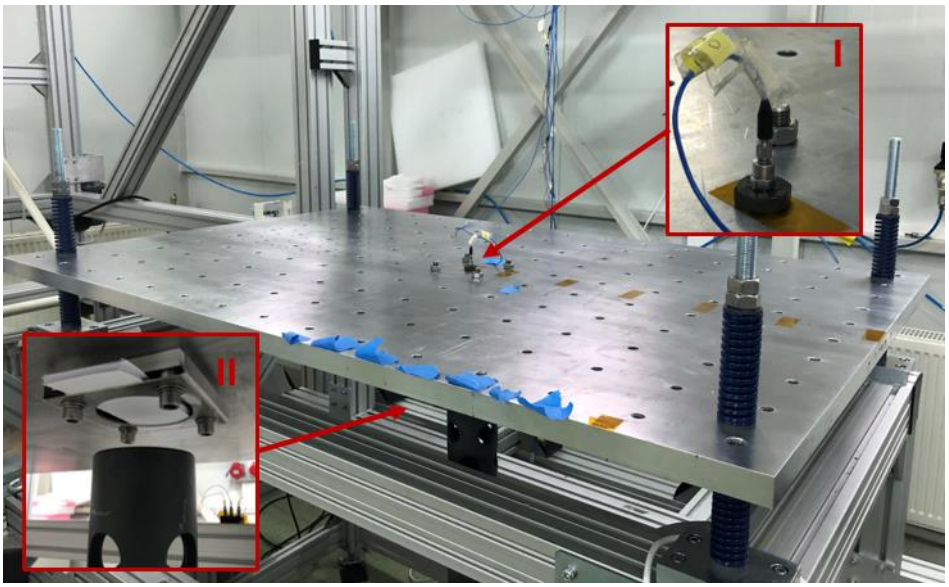


Figure 1.3. Mechanical impact pyroshock test system (I: Accelerometer, II: Impact plate with mechanical filter)

## 1.1 Motivation

The desired shock profile cannot be obtained easily in mechanical impact shock tests. It is necessary to adjust the profile with a dummy model before each test. The desired test profile should be within the tolerance range on the SRS. An example of a shock test specification is shown in Figure 1.4. Each parameter in the test configuration has an effect on the profile. The size, thickness, and boundary conditions of the resonant plate, hammer speed, hammer mass, impact plate and mechanical filter material are the most essential test system parameters. When a shock test is requested, the test operator has to predict appropriate parameters. At this stage, the operator must know the test system parameters' behavior and decide on the configuration. Alternatively, time-consuming tests should be done with the dummy trial and error method. However, this option takes a lot of time. It may even cause many parts to be procured unnecessarily since the appropriate configuration is unknown. For this reason, it is essential to know the effect of test parameters in advance. In this way, the test configuration can be decided quickly according to the need. Although some parameters have been studied by finite element analysis and test methods in the literature, some issues such as defining correct input parameters, including force profile, and investigating their effects on SRS profile have remained limited. Hence, research studies should be carried out to improve the shock test system parameters prediction with FEA and experiment.

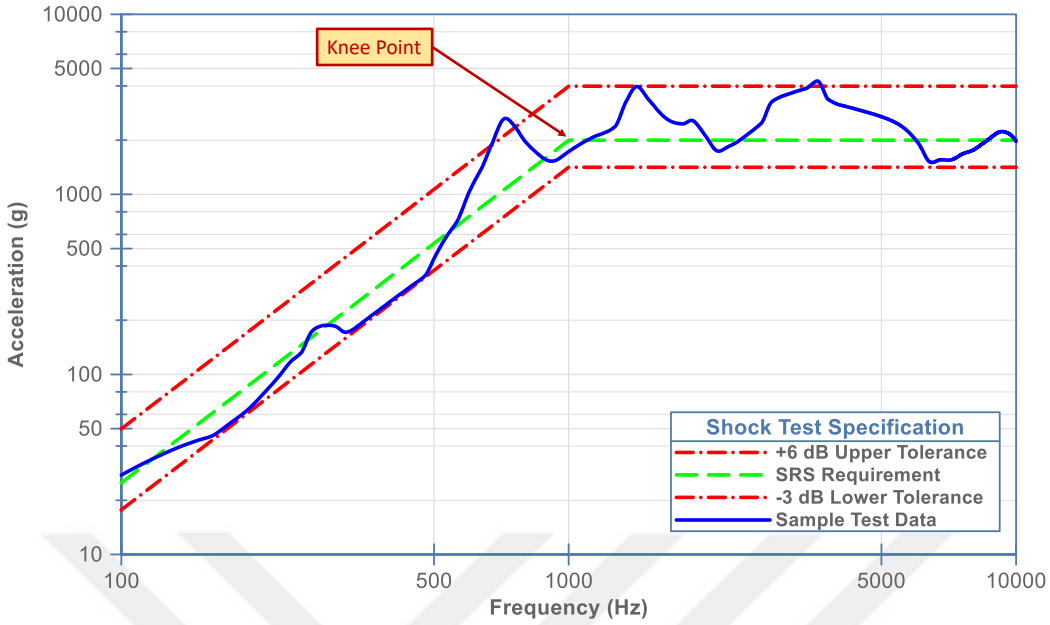


Figure 1.4. A shock test specification example

## 1.2 Literature Review

This section is divided into three parts. The first part describes studies about the design, development, and characterization of a pyroshock test system. There is valuable information about the influence of test parameters such as hammer mass, impact radius, and impact speed on SRS. The second part discusses the papers comparing FEA and experimental results. The third part explains the studies on spacecraft shock tests.

### 1.2.1 Pyroshock Test System Development and Characterization

Binder et al. [2] designed and constructed a pyroshock test simulator for Space Environments Lab at California Polytechnic State University. They performed preliminary research on past pyroshock testing systems. The systems are compared in terms of complexity, characterization and repeatability, attainable acceleration level, test area, and cost. Finally, they chose a suspended plate system with a

pendulum hammer impactor because of its simplicity, available test area, low cost, and demonstrated results. However, the target shock profile could not be achieved in the study. Not only the test system configuration but also there were problems with the data acquisition system. Improper acceleration-time data was shared in the result graphs.

Irvine [3] explained the shock response spectrum calculation. The author derived corresponding equations and developed a code that converts time data to SRS. Additionally, information about shock qualification methods is provided, and capabilities and limits of the shock tests are evaluated, which is performed with explosive, mechanical impact, and shaker. It was also stated that the equipment test levels were much higher than actually exposed at the spacecraft. Components are subjected to over-testing. The author also examined the acceleration and velocity-time responses as a result of half-sine input in the SDOF system.

Pyroshock test is commonly performed in three axes of a test item separately because it is not possible to reach the qualification level in three directions with a shock in one direction. However, depending on the modal characteristics of the test fixture, the test item may also be exposed to loads in cross directions apart from the test direction. Jacobson [4] investigated whether the equipment could be qualified in all three directions with a single axis test. The modal response of structures in the test configuration was studied by Lagrange Multiplier Frequency Based Substructuring Method. At the end of the study, an equal magnitude response is achieved at the in-axis and off-axis direction of the test fixture. This research can be expanded by studying the optimum rotation angle of the test items and impact properties such as location magnitude and direction.

Lee et al. [5] developed a point source shock device. In the pyroshock tests, three consecutive shots have to be applied in each axis. Generally, the previous application location cannot be exactly provided with a point source shock device, and differences may be observed between successive shot SRS results. Moreover, in this developed system, repeatability is directly related to the test system diaphragm deformation.

Similar results could be obtained if it explodes, in the same way, all the time. Besides, the diaphragm will be completely deformed after a certain number of tests, so it has to be renewed. The most significant advantage is that the device can be easily applied to every region of the resonant plate due to its small size. This saves time in the profile determination test.

Hwang et al. [6] designed a new point-source pyroshock simulator that uses disk spring as a resonator. Resonators were produced in various thicknesses to manipulate the shock profile's knee frequency by modifying the first natural frequency. A piston pump mechanism loaded by spring was designed and built. They stated that the repeatability was good in the tests. They can also adjust projectile speed, resonator thickness, cut-out numbers, and impact plate thickness to change the SRS profile. However, they reported that the thickness of the impact plate did not affect. To sum up, they asserted that this system could be used as a shock source in the satellite platform shock tests. The shock levels are pretty low in their results. It may be suitable for simulating low shock but could not be used to simulate the shock that occurs in most separation rings.

Bernaudin et al. [7] highlighted an essential point regarding the determination of equipment shock test levels. They stated that the determination of the level directly from spacecraft tests would not be correct. Actually, the levels should be obtained by combining more than one SRS. Test systems produce a specific SRS profile during the qualification process. Compared to spacecraft test data, proficiency is below or quite above what it should be. They emphasized that the duration and time and frequency data were different in the comparison between equipment qualification test and spacecraft shock measurement. Another calculation method is proposed instead of SRS.

Jonsson [8] built up a pendulum-type shock test facility, which is a metal-to-metal impact system. It was designed for qualifying equipment against shock in compliance with NASA, ECSS, and MIL standards. As it is known from other studies, each parameter of the test system has an effect on obtained SRS. In this

study, the author has characterized them clearly. Effect of impact speed, hammer mass, impact plate material, hammer material, foam type, the boundary condition was explained. Although extensive research has been carried out on pyroshock test systems, there are few studies exist that explain the system characteristics. Hence, it is a useful study for those who will work on this subject. However, additional studies are required on the resonant plate, mechanical filters, and impact plate materials in order to understand SRS behavior. Also, sufficient information about the finite element model has not been provided, such as time step, mesh size, and damping [8, Ch. 2.4].

Kiryenko and Piret [9] introduced a pendulum-type shock test bench in the ESTEC test center. The content in this paper is similar to that used by other researchers. The effect of the main parameters, such as drop height, hammer mass, hammer radius, impact plate characteristics, and position of the test specimen, have been observed.

Fillippi et al. [10] have introduced the Alcatel ETCA shock test facility. The resonant plate is vertically mounted to the structure in the facility, and it is excited by a detonating charge or a mechanical impact. In this article, most of the test parameters were specified without details. The determination of the impact point and the design of the test fixture were emphasized. They had a problem with in-plane tests because of the test fixture. Test fixture cross axis (Z-axis) vibration modes affected test items higher than in-plane fixture mode shapes. This indicates that the test fixture is not suitable. Attention should be paid to this issue during the fixture design phase.

Markl [11] has studied with the circular resonant plate in a suspended position. Parameters such as impact location and measurement location were investigated to meet the test item's required SRS level. Also, It is stated that the cross axes can be stimulated by changing the impact location and angle. Another finding of this study showed that mode shapes should be used when deciding the location of the impact. In summary, it is aimed to reach the desired SRS by changing the impact location and measurement point. However, in the study, the resonant plate was chosen as

circular rather than rectangular, unlike the conventional plates. The advantage or disadvantage of this difference should have been addressed.

### 1.2.2 Pyroshock Test System Analysis And Validation

In ECSS mechanical shock design and verification handbook, numerical analysis methods and procedures are comprehensively described [1, Ch. 9]. Strong and weak points of explicit and implicit methods are expressed, and an explicit approach is recommended for shock analysis since the shock event is highly dynamic and load duration is very short. It guides the reader step by step about modeling and contains important notifications related to meshing size, time step, different wave types, element type, damping. The information on FEA modeling is crucial in terms of getting correct answers at high frequencies.

Morais and Vasques [12] published a paper that starts with the understanding of the shock test specification, follows with the review of the state of the art of shock test methods, and ends with a sustained demonstration of the selected in-plane (IP) pendulum shock test configuration. They emphasized that understanding impact phenomena is essential for accurate shock environment design. They mentioned the repeatability of shock tests and stated the same pulse parameters would reproduce the same SRS. It has been stated that FE analysis performed in IP configuration was compatible with test results. Although there are many FE studies, information relating to the analysis parameters remains limited.

Siam [13] aimed to develop an effective and reliable shock analysis method using FEM for space equipment in his thesis. The strengths and weaknesses of various analysis methods were examined, and determined that the most effective way is modal transient response analysis. The FEA model is excited with complex acceleration - time data. A triangular resonant plate was used to compare the FEA results in the test infrastructure. The triangular plate is one of the unusual plate shapes. The author shared beneficial information about simulation techniques. One

of these is related to the definition of the damping coefficient. It has been stated that a low damping coefficient should be used in order to obtain accurate data at high frequencies in thin-walled structures.

Ruess et al. [14] investigated the root cause of optical equipment failure during shock tests. The equipment has a mirror that is glued to the flange. Its alignment was distorted during the test. Firstly, they correlated their FE model and compared loads with the test. Their numerical simulation approach is stated in the ECSS shock handbook [1, Ch. 18.2.4.5]. After the identification of the problem, they developed a recovery solution.

Jayaraman et al. [15] investigated the effect of mechanical shock load on the printed circuit board (PCB), which contains many sensitive components to shock. The shock level to these components can be predicted by finite element analysis, but it is known that there are often deviations from the actual levels. In their study, firstly, they subjected the finite element model of PCB to modal analysis and then response spectrum analysis. They compared their results with experimental ones. It has been observed that there is an acceptable difference in the results. They emphasized that more detailed modeling is needed, and material properties should be known more accurately to match the results better. They have made a meaningful study to examine how shock waves propagated in PCB type materials.

### 1.2.3 Spacecraft Shock Tests

Kitamura et al. [16] analyzed the shock response of satellite separation. Firstly, they created a FE model of the satellite body and verified their model with a satellite modal test. In the second step, they have performed a static analysis to compute forces exerted on the central cylinder from the clampband. Eventually, they made transient response analysis by using calculated forces as an input parameter and viewed acceleration time history at any location in the satellite body. They compared FE results with the clampband separation shock test data.

In ECSS mechanical shock design and verification handbook, system-level numerical simulation studies are described [8, Ch. 9.4]. In these studies, the shock source related to clampband separation, pyrotechnic bolts, other launcher induced shocks were described in detail. It was stated that the analysis results could not be verified very well with the test results at every location. Therefore, shock environment prediction should not be made only by simulation, but also other methods (extrapolation, test) should be evaluated. The range of validity of numerical simulation results is limited with low frequencies (< 2 kHz). Here, one of the reasons why test results could not be verified by analysis was the models having quite large and many interconnected structures.

## 1.3 Research Objectives

The synthesis of experimental study and numerical methods is needed for finding the correct parameters of the pyroshock test setup such that targeted SRS profile can be achieved in a time and cost-efficient manner. For this purpose, a reliable FEA model has to be established. Correct input force and boundary conditions have to be defined in addition to the other FE modeling parameter to get accurate analysis prediction. Then experimental tests should be performed in the same manner as in the analysis. In this way, the accuracy of the FEA model should be verified. With this thesis, the important pyroshock test system parameters will be identified, and the required test configurations will be quickly determined according to the required SRS profile. Also, a proven FEA model which can be utilized in space structure shock analysis will be developed.

## 1.4 Scope of the Research

In this thesis, an impact model will be created in order to observe the force profile formed during the impact at the first step. Here, the effects of parameters such as hammer speed and hammer mass on the force profile will be observed. These profiles

will be used as a concentrated transient load in the preliminary resonant plate FEA model. The effects of parameters on SRS will be started to be examined. Then, force measurement tests will be performed. These tests will result in the actual force profile generated during the impact. In addition, the effects of materials such as plexiglass, rubber, and Delrin, which are difficult to model, on force profiles will be measured. Obtained force profiles will be used in the FEM analysis of the resonant plate. The effects of important test parameters will also be measured by experimental setup, and these results will be compared with the results calculated from the analysis. A summary of the test parameters and their examination methods are presented in Table 1.1. In addition, analysis predictions and test measurements for the same configuration will be compared to see the reliability of the FEM model in understanding the effects of important test parameters on the SRS profile.

Table 1.1 Test system parameters and its investigation methods

| Test System Parameters | Investigation Methods | | |
|---|---|---|---|
| | Numerical (FEM) | Force Measurement Test | Pyroshock Test |
| Hammer speed | ✓ | ✓ | ✓ |
| Hammer mass | ✓ | ✓ | ✓ |
| Impact location | ✓ | N/A | ✓ |
| Measurement location | ✓ | N/A | ✓ |
| Resonant plate thickness | ✓ | N/A | ✗ |
| Resonant plate side length | ✓ | N/A | ✓ |
| Impact plate and mechanical filters material | ✓ | ✓ | ✓ |
| Resonant plate boundary condition: Clamped | ✓ | N/A | ✗ |
| Resonant plate boundary condition: Spring | ✓ | N/A | ✓ |
| Resonant plate boundary condition: Hanging | ✓ | N/A | ✓ |
| Hammer tip radius | ✗ | ✓ | ✗ |

## 1.5 Outline of the Thesis

There are six chapters in this study. In Chapter 1, a brief introduction to the subject of the thesis is firstly presented. Then motivation, literature review, research objectives, and scope of the research are addressed. This chapter concludes with the outline of the thesis.

In Chapter 2, shock response spectrum derivation and implementation are covered. Firstly, the shock spectrum calculation is explained. Afterwards, the standard for the calculation of SRS is introduced.

In Chapter 3, studies on finite element analysis are presented. This chapter first introduces dynamic analysis methods. The strengths and weaknesses of the different analysis methods are evaluated. Then, FEA modeling parameters are discussed. Mesh, element type, time step, damping modeling, boundary conditions, and load conditions are explained. This chapter concludes with the characterization of test system parameters. Here, all the parameter results obtained from the analysis model are included.

In Chapter 4, experimental studies are presented. This chapter starts by presenting force measurement tests. Then, pyroshock test results are stated. Following, the pyrovalf test result is given.

In Chapter 5, FEA outputs are compared with test results. The comparison results for plates with the two different dimensions are presented.

In Chapter 6, The conclusion of the study is included.

# CHAPTER 2

# NUMERICAL SIMULATION AND ANALYSIS APPROACH

Many analytical solutions to problems in the field of engineering have been developed. However, an analytical approach is not possible in the case of complex geometry and loading conditions. With the beginning of the computer age, the use of numerical methods has increased, and more complex problems can be calculated with a certain margin of error.

In engineering, time and space-dependent problems are commonly described with partial differential equations. FEM is a particular numerical method used to solve partial differential equations. This method divides the problem into smaller, simpler parts, which are called finite elements. Every element is connected by nodes to each other. Trial solutions could be presumed to obtain an approximate solution for each element. Additionally, the trial solution has to satisfy the boundary conditions of the problem.

The finite element analysis approach could be preferred to simulate the shock environment in a structure. The general FEM dynamic analysis procedure is valid in shock prediction, and a transient response analysis could be applied to get the response levels at desired locations.

## 2.1 Dynamic Analysis Methods

A wide range of stress analysis problems can be solved with FEM. The primary classification of these problems is a static or dynamic response; dynamic problems have significant inertia effects.

There are some methods in order to perform these dynamic analyses [17]. Modal methods are typically used for linear analyses. Since the system's global equations

of motion need to be integrated over time in direct integration, which makes direct integration approaches considerably more costly than modal methods.

### 2.1.1 Implicit and Explicit Dynamics

The dynamic direct-integration procedure provides a selection of implicit operators for the integration of motion equations, whereas explicit utilizes the central difference operator. In implicit dynamic analysis studies, the integration operator matrix must be reversed, and, at each time increment, the program has to solve a series of nonlinear equilibrium equations. In explicit dynamic analysis studies, displacements and other quantities are measured and defined at the beginning of any time increment. Accordingly, it is not appropriate to build and invert the global mass and stiffness matrices, meaning that each increment is reasonably and computationally inexpensive compared to the increments in an implicit integration scheme.

However, the time step in an explicit dynamic analysis is constrained since the operator of the central differential is only conditionally stable. In contrast, the implicit operator is unconditionally stable. Therefore, there is no restriction on the duration of the time increment.

The stability limit for the method of central difference (the highest time increment that can be taken without the method producing large, quickly increasing errors) is closely related to the duration required to wave cross the model's smallest element dimension. Hence, if the mesh contains small elements or if the material's wave velocity is too high, the time increment in an explicit dynamic analysis needs to be short.

In this thesis, ABAQUS / Explicit is used. Some of the advantages are as follows:

1. The cost of the analysis increases linearly with the size of the problem, while the cost of solving the implicit integration based nonlinear equations

increases more quickly with the size of the problem. Thus, for complex models, ABAQUS/Explicit is suitable.

2. To solve highly discontinuous short duration events, the explicit integration approach is more effective than the implicit integration process.
3. In ABAQUS/Explicit, problems concerning wave dispersion can be much more computationally effective than in ABAQUS/Standard.

### 2.1.2 Modal Superposition Procedures

Modal superposition procedures are a lower-cost method for carrying out linear or lightly nonlinear dynamic experiments. However, direct solution techniques are essential for nonlinear dynamic analyses.

ABAQUS involves a complete set of techniques for modal superposition [18]. One of the procedures is high performance linear dynamic software structure termed SIM. Its architecture provides more benefits in large-scale problems than the conventional method. This technique is very efficient, especially when the model size and the number of modes is large, and a small number of data output is required.

In the first step of modal superposition analysis, the natural frequencies of the problem must be identified using the eigenvalue analysis technique.

Available modal superposition procedures in ABAQUS are stated below:

- Mode-based steady-state harmonic response analysis can be performed to estimate a structure's linearized response to harmonic excitation.
- Mode-based transient response analysis offers a transient solution to linear problems using modal superposition.
- Response spectrum analysis is often utilized to estimate the upper limit of a structure's peak response to input load (for instance, earthquake data) in the frequency spectrum. This approach has a very low cost of computation and offers valuable information on the structure's spectral nature.

- In random response analysis, the response of a system to random excitation can be determined based on the natural frequencies of the system. Response load is represented in terms of a "Power Spectral Density" (PSD) function.

### 2.1.3 Transient Modal Dynamic Analysis

The transient modal dynamic analysis provides a structure response as a function of time according to the applied time-dependent load. Firstly, the modes of the structure are extracted by eigenvalue analysis. In the second step, the response of the structure to the applied loads is obtained by using these modal responses. In this study, the maximum frequency of interest is 10000 Hz, but modes up to 15000 Hz were extracted in each analysis. It is aimed to predict the contribution of high frequencies to low frequencies. 320 modes were extracted for 1000x1000x50 $mm^3$ resonant plate and 500 modes for 1500x1000x30 $mm^3$ resonant plate analysis.

### 2.1.4 Damping in Dynamic Analysis

Every system shows certain energy loss related to material nonlinearity, internal material friction, or external frictional activity (mostly joint). Structural products such as steel and alloys with high-strength aluminum have limited quantities of internal material damping, not enough to avoid strong amplification at or around resonant frequencies. Generally, it is difficult to determine the source of damping. Usually, they occur simultaneously from different sources. For instance, energy loss while hysteretic loading, viscoelastic material properties, and joint friction.

People who work in a particular device are aware of energy loss from experience. Several methods are available in ABAQUS to correctly determine damping that model energy loss in a dynamic environment.

In this study, modal damping is assigned as the source of damping. Modal damping can be implemented only to mode-based linear dynamic analysis, and for each mode

in the model, it can be described with damping ratio. Common values of the damping ratio vary from 1% to 10%. This procedure applies the damping directly to the modes of the structure. Modal damping is added diagonal elements of the modal system of equations.

## 2.2 Finite Element Modeling Parameters

This section discusses how FEA parameters affect the analysis results. The material is aluminum in all models, and its density is 2700 $kg/m^3$ , Young's modulus 68.9 GPa, Shear modulus 25 GPa, and Poisson's ratio 0.33 are defined. This section concludes with a description of the model used in all analyses.

### 2.2.1 Mesh

In dynamic analysis, the determination of mesh element size and type is one of the important stages. It should be determined according to the maximum frequency of interest in order to avoid errors. The smallest wavelength corresponding to the maximum frequency is considered. There are shear, flexural and traction-compression types of waves that propagate in a structure. In order to correctly simulate the propagation of these waves, at least eight elements per wavelength are recommended [1, Ch. 9.2.4.1]. The wavelength formulation is presented in Table 2.1 and calculations for this study are given in Table 2.2 and Table 2.3.

Table 2.1 Wavelength formulation of different wave types [1]

| Wave Type | Wavelength Formula |
|---|---|
| Traction-compression | $\lambda = \frac{\sqrt{E/\rho}}{f}$ |
| Shear | $\lambda = \frac{\sqrt{G/\rho}}{f}$ |
| Flexural | $\lambda = \left(\frac{2\pi}{f}\right)^{1/2}\left(\frac{D}{\mu}\right)^{1/4} = \left(\frac{2\pi}{f}\right)^{1/2}\left(\frac{Et^2}{12\rho}\right)^{1/4}$ |

Table 2.2 Wavelength calculation of traction-compression and shear waves for the aluminum resonant plate

| Wavelength Calculation of Traction-Compression and Shear Waves |
|---|
| $\lambda_{\substack{Traction \\ Compression}} = \frac{\sqrt{\frac{68.9 \cdot 10^9}{2700}}}{10000} = 0.505 \text{ m}$ |
| $\lambda_{Shear} = \frac{\sqrt{\frac{25 \cdot 10^9}{2700}}}{10000} = 0.304 \text{ m}$ |

Table 2.3 Wavelength calculation of flexural waves for 100, 50, 30, and 12 mm thick aluminum resonant plate

| Wavelength Calculation of Flexural Waves |
|---|
| $\lambda_{Flexural,100\ mm} = \left(\frac{2\pi}{10000}\right)^{1/2}\left(\frac{68.9\cdot 10^{9}\times 0.1^{2}}{12\times 2700}\right)^{1/4} = 0.303\ m$ |
| $\lambda_{Flexural,50\ mm} = \left(\frac{2\pi}{10000}\right)^{1/2}\left(\frac{68.9\cdot 10^{9}\times 0.05^{2}}{12\times 2700}\right)^{1/4} = 0.214\ m$ |
| $\lambda_{Flexural,30\ mm} = \left(\frac{2\pi}{10000}\right)^{1/2}\left(\frac{68.9\cdot 10^{9}\times 0.03^{2}}{12\times 2700}\right)^{1/4} = 0.166\ m$ |
| $\lambda_{Flexural,12\ mm} = \left(\frac{2\pi}{10000}\right)^{1/2}\left(\frac{68.9\cdot 10^{9}\times 0.03^{2}}{12\times 2700}\right)^{1/4} = 0.105\ m$ |

Flexural waves depend on the geometric properties of the structure besides the material properties. They are dispersive, which means wave propagation speed is dependent on frequency [19, Ch. 4.5]. According to Table 2.2 and Table 2.3, the flexural wave is the determining factor in the calculation of the element size compared to other waves.

In this study, more than eight elements per wavelength did not make significant improvements, and the calculation has been made by taking eight elements per wavelength, according to Table 2.4.

Table 2.4 Element size calculation for different thickness resonant plates

| Element Sizes |
|---|
| For 100 mm thickness plate $= \frac{0.303}{8} = 0.0379$ m $\cong 37.5\ mm$ |
| For 50 mm thickness plate $= \frac{0.214}{8} = 0.0268$ m $\cong 25\ mm$ |
| For 30 mm thickness plate $= \frac{0.166}{8} = 0.0208$ m $\cong 20\ mm$ |
| For 12 mm thickness plate $= \frac{0.105}{8} = 0.0131$ m $\cong 12.5\ mm$ |

In order to observe mesh dependency, various mesh structures have been created in different element sizes, types and their effects have been monitored. For instance, 25 mm standard and 5 - 25 mm bias mesh structures are shown in Figure 2.1. This work was done with a 1000x1000x50 $mm^3$ plate. The summary of these studies is presented in Table 2.5, and the result of modal response and resonant plate shock analysis shown in Figure 2.2, and Figure 2.3, respectively.

Table 2.5 Mesh dependency studies summary

| No | Type | Dimension (mm) | Number | Properties |
|---|---|---|---|---|
| 1 | S4R | 100 | 100 | Linear quadrilateral |
| 2 | S4R | 50 | 400 | Linear quadrilateral |
| 3 | S4R | 25 | 1600 | Linear quadrilateral |
| 4 | S4R | Bias 5 – 25 | 6400 | Linear quadrilateral |
| 5 | S4R | Bias 2.5 – 12.5 | 25600 | Linear quadrilateral |
| 6 | SC8R | 25 | 3200 | Linear hexahedral |

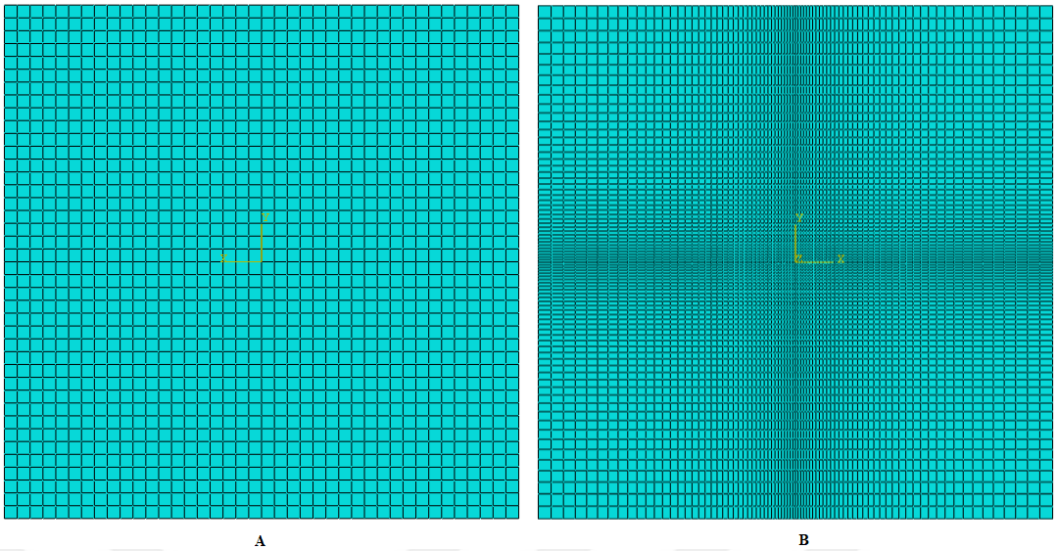


Figure 2.1. Mesh patterns: A (25) versus B (Bias 5-25)

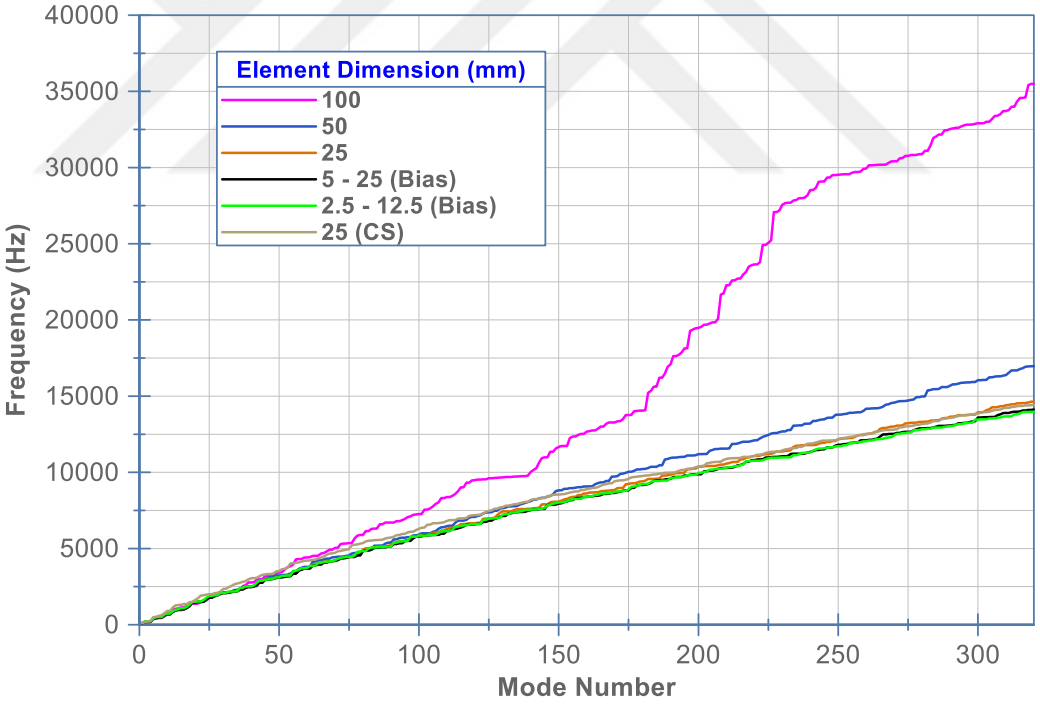


Figure 2.2. Frequency versus mode number for different element dimension

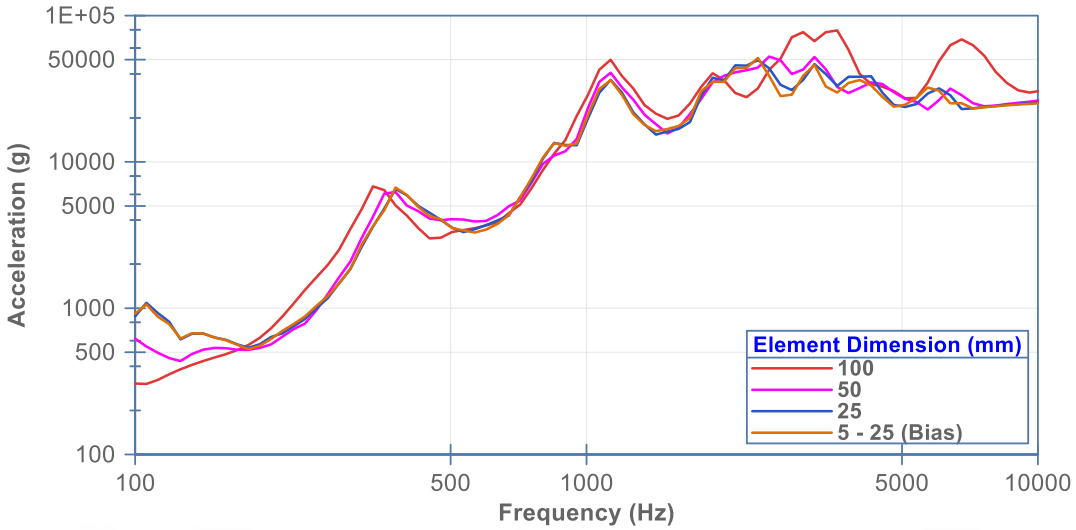


Figure 2.3. Frequency versus acceleration for different element dimension

### 2.2.2 Element Type

As the maximum frequency of interest increases, a particular emphasis should be placed on the selection of the element type. For example, solid elements can be used instead of shell elements, or integration points of shell elements can be increased.

Elements are characterized by family (continuum, shell, beam elements), degree of freedom, number of nodes (8 nodes linear element, 20 nodes quadratic element, 10 node tetrahedron element), formulation, and integration.

Shell elements are used if the thickness of the structure is considerably smaller than its length and width. In this study, conventional shell elements are used in which the thickness is defined on the reference surface.

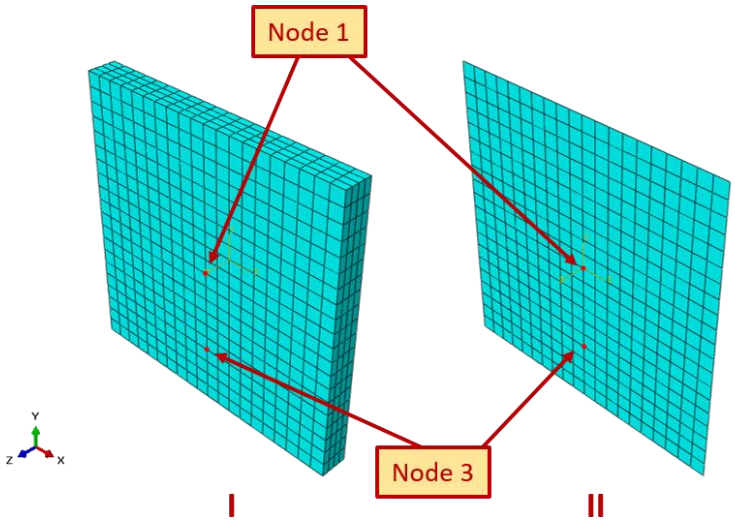


Figure 2.4. 300x300x30 mm model (I: Solid, II: Shell)

At the beginning of the study, the responses of solid and shell elements were examined in the simplified model, which is the size of a 300x300x30 $mm^3$ aluminum plate, shown in Figure 2.4. As a boundary condition, displacement in the Z-axis direction at the corner nodes is defined as zero. First of all, the natural frequencies of the structures have been extracted in the analysis. Then the responses of the structures to the transient load were compared using the modal superposition technique. Since the modal superposition technique is used, any difference in the models' natural frequencies affects the results. For this reason, the effect of element types and boundary conditions on natural frequency has been examined in detail. The obtained natural frequency values are given in Table 2.6.

Table 2.6 Comparison of modal responses of shell and solid model

| *Mode Number* | *Solid Model* | | *Shell Model* | |
|---|---|---|---|---|
| | *Eigenfrequencies (Hz)* | *Modal participation factor in the z-axis* | *Eigenfrequencies (Hz)* | *Modal participation factor in the z-axis* |
| 1 | 520 | 6.85E+00 | 537 | 6.86E+00 |
| 2 | 1075 | 2.66E-26 | 1114 | 2.31E-23 |
| 3 | 1075 | 6.79E-25 | 1114 | 2.37E-25 |
| 4 | 1493 | 4.10E-23 | 1526 | 2.41E-24 |
| 5 | 2499 | 3.46E-22 | 2612 | 2.99E-24 |
| 6 | 2992 | 2.47E-01 | 3095 | 2.43E-01 |
| 7 | 3475 | 2.65E-23 | 3585 | 1.15E-22 |
| 8 | 3475 | 2.81E-20 | 3585 | 1.06E-23 |
| 9 | 4791 | 8.95E-23 | 4891 | 3.80E-23 |
| 10 | 5223 | 1.14E-30 | 5403 | 1.92E-26 |
| 11 | 5223 | 8.37E-30 | 5403 | 2.11E-22 |
| 12 | 5718 | 1.12E-01 | 5961 | 1.15E-01 |
| 13 | 6451 | 1.52E-26 | 6454 | 3.29E-21 |
| 14 | 6920 | 6.63E-26 | 6931 | 1.96E-23 |
| 15 | 6920 | 6.91E-23 | 6931 | 2.01E-21 |
| 16 | 7276 | 8.54E-19 | 7302 | 9.54E-23 |
| 17 | 7297 | 2.97E-28 | 7598 | 9.58E-25 |
| 18 | 7466 | 9.69E-28 | 7658 | 3.29E-21 |
| 19 | 7466 | 1.48E-27 | 7658 | 1.30E-20 |
| 20 | 7856 | 8.55E-28 | 8006 | 1.10E-20 |

The SRS graphs obtained in node 1 and node 3 are shown in Figure 2.5 and Figure 2.6. Minimal differences were observed in the results. It is thought to be due to differences in natural frequency values.

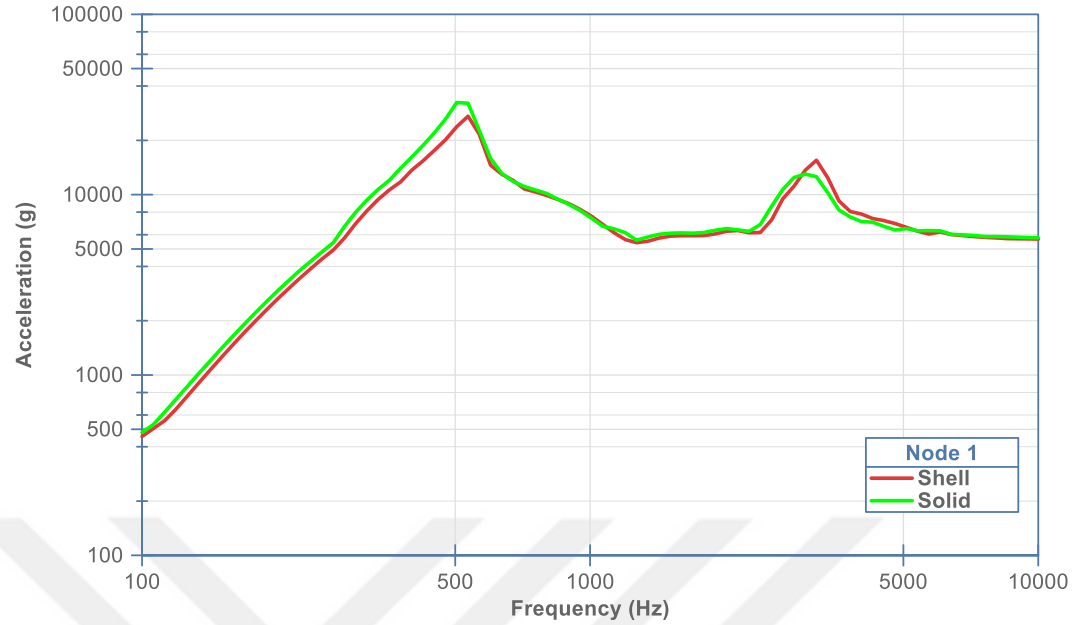


Figure 2.5. Comparison of shell and solid model SRS graphs at node 1

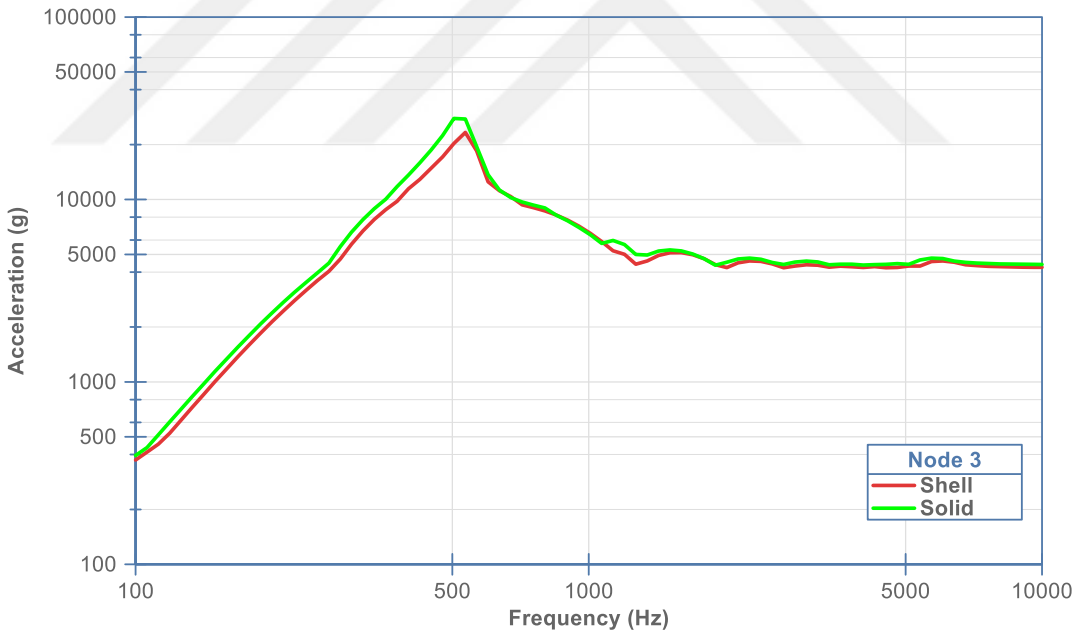


Figure 2.6. Comparison of shell and solid model SRS graphs at node 3

Another parameter in determining the element type is whether the element should be linear or quadratic. When the element is defined as quadratic in the shell model, the number of nodes increases from 4 to 8. This raises the computation time and memory

usage. However, in circular boundary conditions, quadratic elements represent better because linear elements cannot fully describe the circular boundaries [20]. The results obtained with quadratic and linear elements for the 1000x1000x50 $mm^3$ shell model are indicated in Figure 2.7.

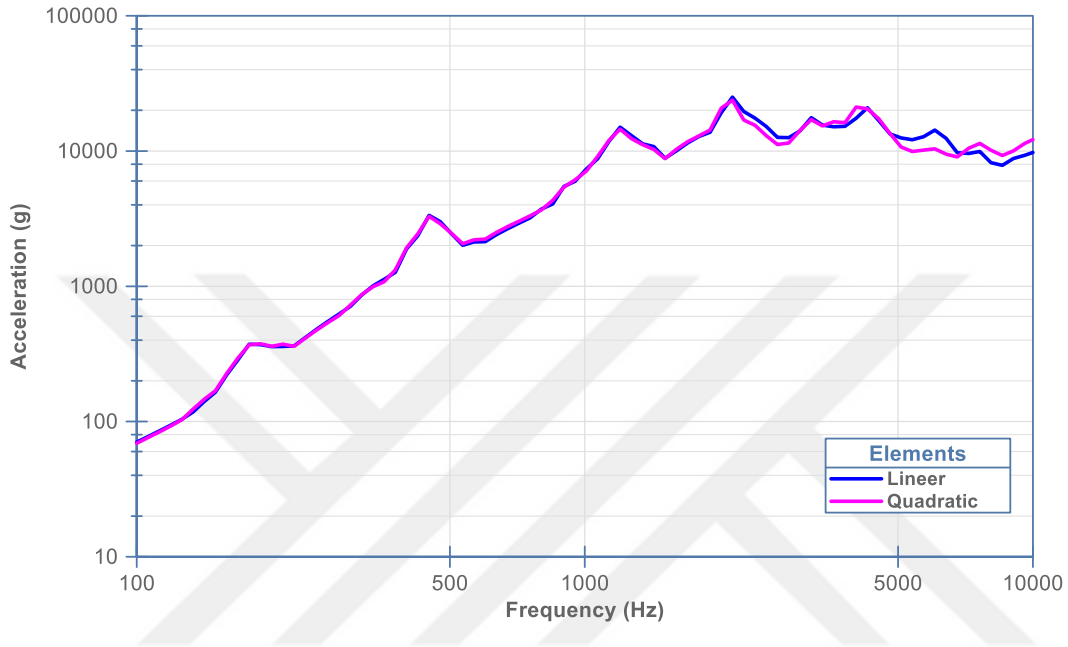


Figure 2.7. Comparison of linear and quadratic element SRS graphs at node 4

Reduced (lower order) integration feature is applied to many element types in ABAQUS. This feature relates to the formation of element stiffness. The mass matrix and the distributed loads are precisely integrated. Reduced integration simply provides more accurate results and notably decreases computation time. When this feature is applied with first-order (linear) elements, control of the hourglass is necessary.

In this study, conventional shell elements with 5 thickness integration points are implemented, using Simpson integration rules.

### 2.2.3 Time Step

The time step should be kept as small as possible in order to represent the shock wave in the structure correctly, but as it gets smaller, the computational cost increases. Therefore, it should be determined according to the maximum frequency of interest in simulation.

Time step ($\Delta t$) is dependent on the sampling rate of the shock input load. At least 5 times per cycle sampling rate is recommended in order to produce shock input load accurately.

The following formula is used initially to determine the time increment [1].

$$\Delta t \leq \frac{1}{20 \cdot f_{max}} \leq \frac{1}{20 \cdot 10000} \leq 5 \cdot 10^{-6} \text{ s} \tag{2-1}$$

In dynamic analysis, numerical consistency is maintained by checking Courant Condition [1, Ch. 9.2.4.2].

$$\text{Courant Condition} = \frac{c_F \cdot \Delta t_{max}}{\Delta x} \leq 1 \tag{2-2}$$

$$\text{Courant Condition} = \frac{3130\ x\ 5 \cdot 10^{-6}}{25 \cdot 10^{-3}} = 0.626 \leq 1 \tag{2-3}$$

This condition specifies that the distance traveled by the wave within the finite element model ($c \cdot \Delta t_{max}$) less than the mesh element length ($\Delta x$).

The following courant conditions were applied in the comparison analysis made in Chapter 5.

$$\text{Courant Condition for 1000x1000x50 mm}^3\text{ plate} = \frac{3130\ x\ 1.1 \cdot 10^{-6}}{25 \cdot 10^{-3}} = 0.138 \leq 1 \tag{2-4}$$

$$\text{Courant Condition for 1500x1000x30 mm}^3\text{ plate} = \frac{3130\ x\ 1.1 \cdot 10^{-6}}{20 \cdot 10^{-3}} = 0.172 \leq 1 \tag{2-5}$$

### 2.2.4 Damping Modeling

It is hard to quantify or estimate the effect of distinct damping sources in the structure, and therefore a certain error will often occur between test measurements and simulation performance. However, by comparing the analysis results with the test results, the damping coefficients in each mode can be adjusted; thus, the error rate could be reduced. In the analysis, the damping ratio is defined to 320 modes of 1000x1000x50 $mm^3$ plate and 500 modes of 1500x1000x30 $mm^3$ plate.

The optimal damping ratio distribution obtained for the case where the impact occurs from the middle of the 1000x1000x50 $mm^3$ plate and 1500x1000x30 $mm^3$ plate is shown in Figure 2.8 and Figure 2.9, respectively.

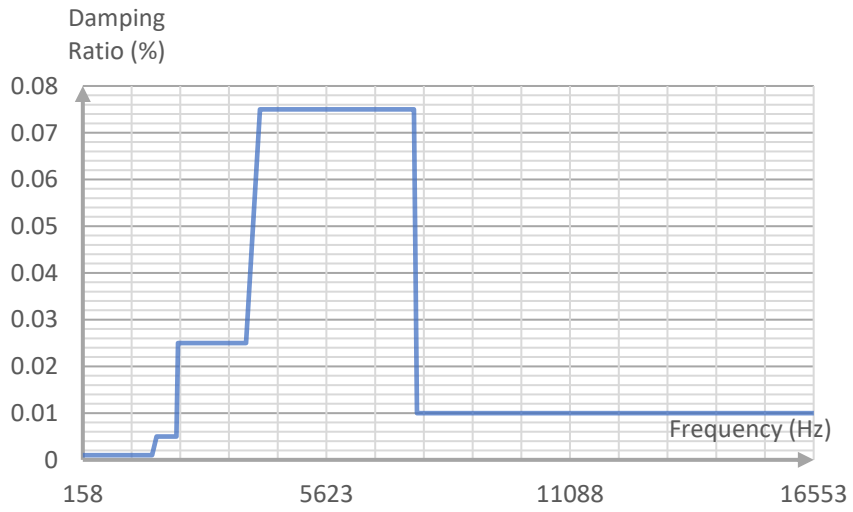


Figure 2.8. Damping ratio distribution of 1000x1000x50 $mm^3$ plate

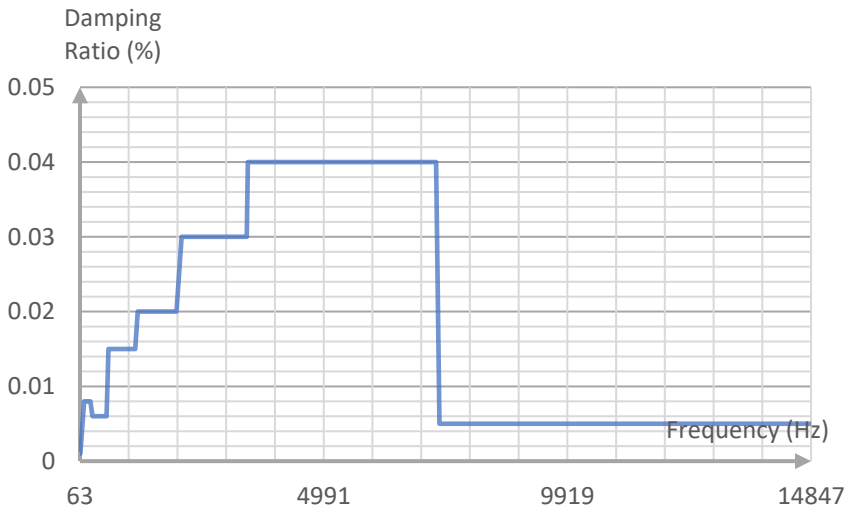


Figure 2.9. Damping ratio distribution of 1500x1000x30 $mm^3$ plate

The distributions can be examined in three different frequency regions. At the starting frequencies, the level is gradually increasing, high at the middle frequencies and low at the high frequencies. The analysis results obtained with the estimated damping ratios were compared with the test measurements in Chapter 5. The damping ratio values were modified until an acceptable match between the experimental SRS and numerically estimated SRS is obtained. An overall good match was observed in the results.

In literature, it is stated that the damping value should be decreased when dealing with thinner material [13]. This information has also been confirmed in our study. The 50 mm thick plate damping values in Figure 2.8 are approximately twice of the 30 mm thick plate in Figure 2.9.

### 2.2.5 Boundary Conditions

Resonant plate boundary conditions have a direct effect on the results. Physically, tests can be performed under free (hung by a string), spring, and sponge boundary conditions, as shown in Figure 2.10.

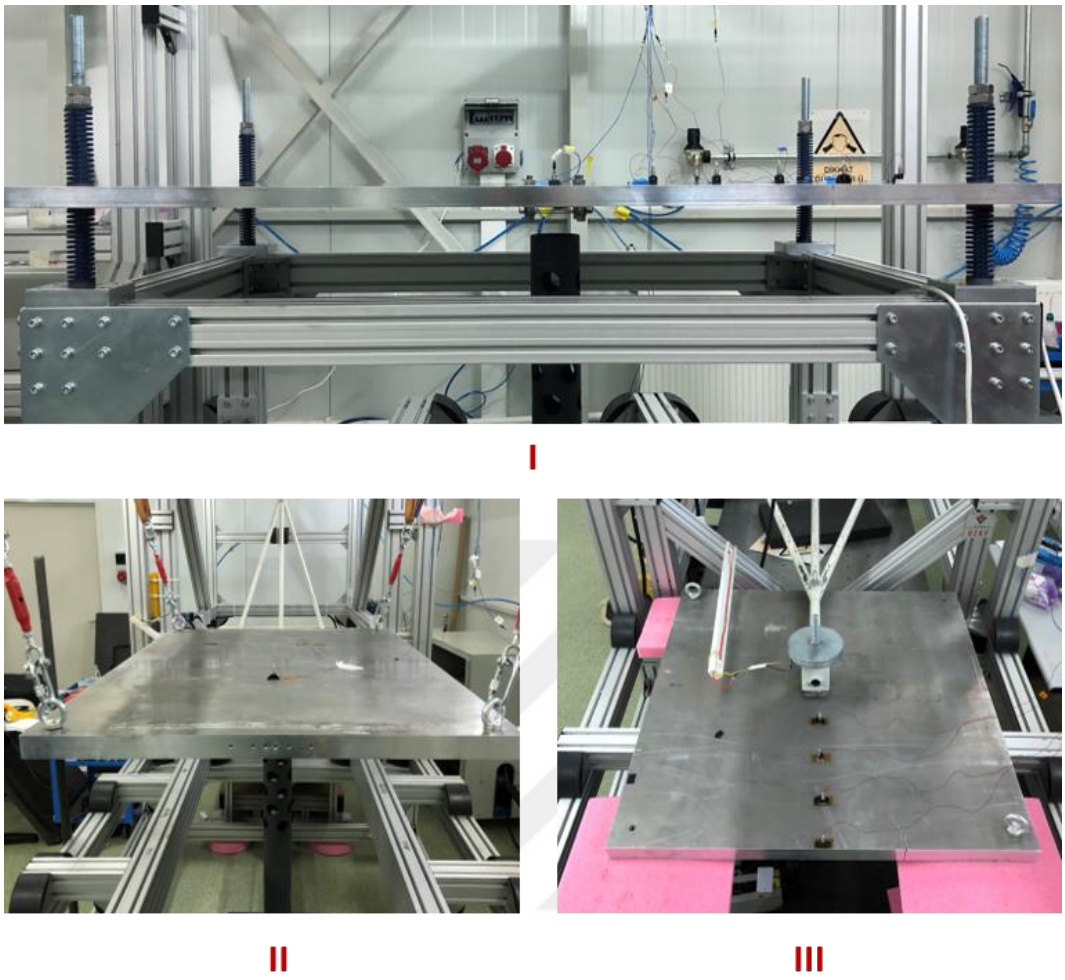


Figure 2.10. Resonant plate boundary conditions in the test facility (I: Spring, II: Free, III: Sponge)

In order to observe the effect of boundary conditions on the SRS profile, free, fixed, and springs are modeled on a 1000x1000x50 $mm^3$ plate. Springs are classified according to their degree of stiffness. Light (k:35 kN/m), medium (k:70 kN/m), and heavy (k:140 kN/m) load springs are used in the industry. In Figure 2.11, the FEA analysis model with spring boundary conditions is presented.

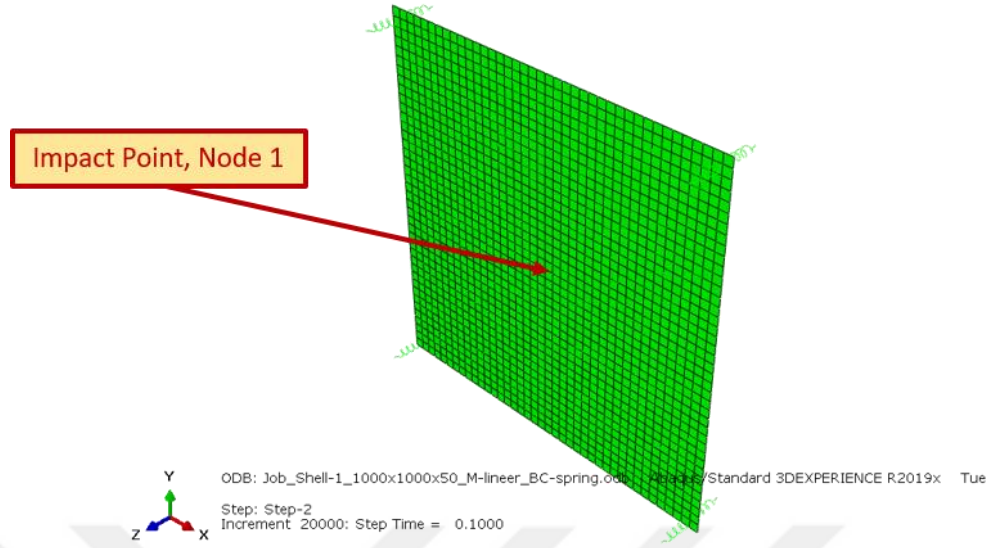


Figure 2.11. 1000x1000x50 $mm^3$ plate modeled with springs from four corners

Results can be seen from Figure 2.12 and Figure 2.13; no remarkable difference is observed between springs and free state. Similar results were obtained in the test facility in subsequent trials.

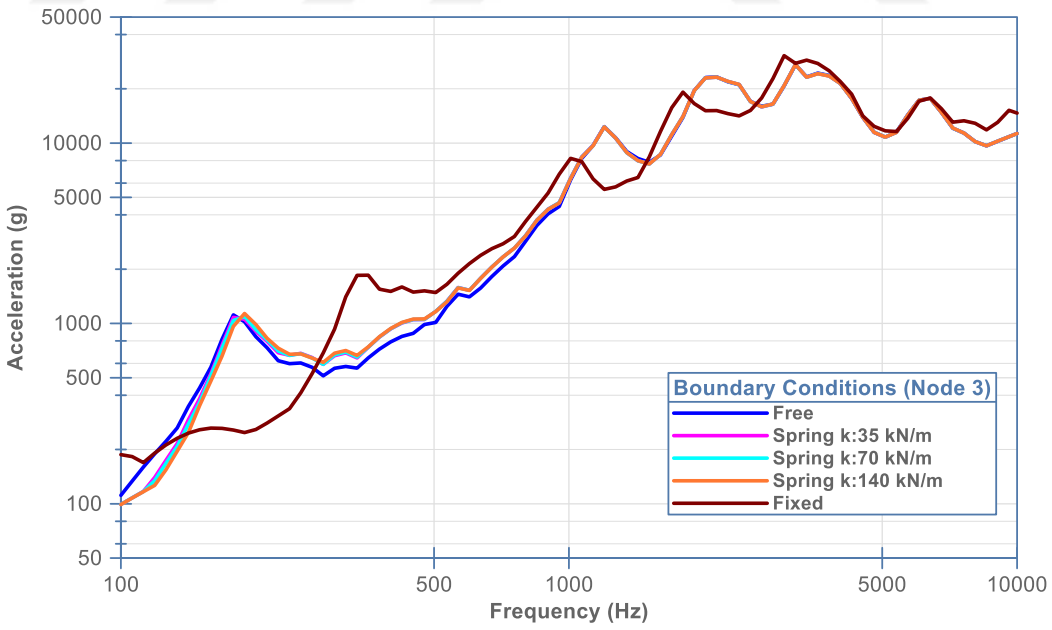


Figure 2.12. The effect of boundary conditions on the SRS graph, Node 3

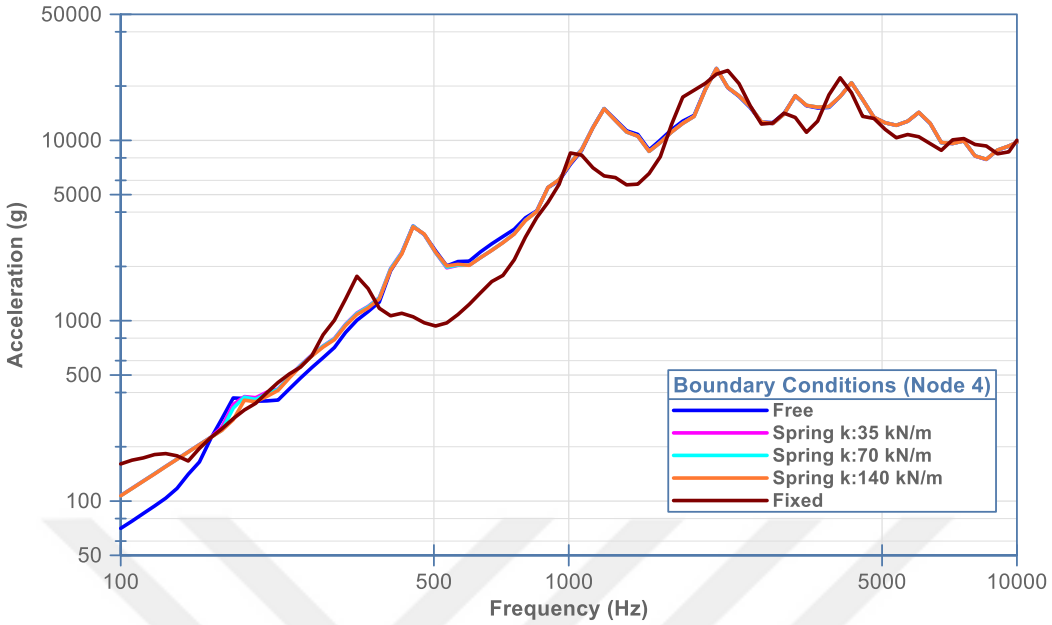


Figure 2.13. The effect of boundary conditions on the SRS graph, Node 4

### 2.2.6 Load

A high-magnitude of force is instantly generated by the impact of the hammer on a resonant plate. Many sources in the literature have stated that the resulting force is in the form of a half-sine as shown in Figure 2.14, and shape of the force profile directly affects the SRS profile [12], [1], [21]. At the beginning of this work, impact analyses are performed to observe how the hammer's speed and mass have an effect, the details of which are given in Chapter 3.2. Besides, the force measurement tests described in Chapter 4.1 were carried out to understand the validity of the half-sine approximation better. In these tests, the effect of the material of the mechanical filter could also be observed. As a result of these studies, FEM input forces were determined.

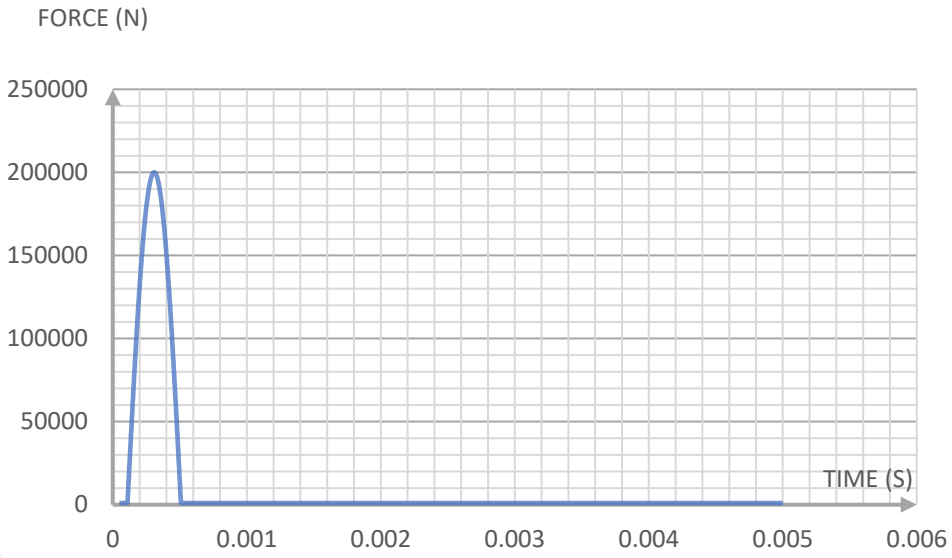


Figure 2.14. Sample half-sine pulse, duration: 400 μs

### 2.2.7 The Parameters Used in Finite Element Analysis

The used model consists of S4R shell elements. The element size varies according to the thickness of the plate to capture flexural waves up to 10000 Hz. Element sizes used on each plate are indicated in Table 2.4. Reduced integration feature is also used. As a time increment, 5 μs is applied and the analysis duration is 0.1 s. Free boundary conditions are preferred to make the model similar to the configuration in the test facility. These FEA parameters were used to examine the behavior of the test system parameters. For the 1000x1000x50 $mm^3$ plate, the FEA model is shown in Figure 2.15.

In the analysis in Chapter 5, where direct comparisons of the FEA model and the test configuration were made, the time step is taken 1.1 μs, and the analysis period is 0.11 s. In the natural frequency identification step, modes up to 15000 Hz were requested, which equivalent to one and a half times the frequency of the maximum SRS requirement frequency.

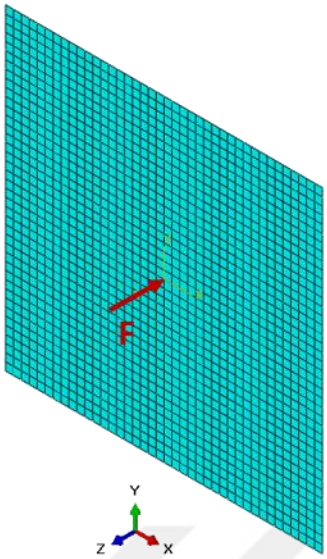


Figure 2.15. 1000x1000x50 $mm^3$ plate model with a concentrated force point

## 2.3 Post-Processing of Shock Time Data

The time-dependent trace of the shock is obtained from the FEM analysis output or test system accelerometer. The time history data is needed to be transformed into a different form to evaluate shock severity in each frequency. This transformation process is referred to as the data reduction method. The commonly used method is a reduction to the response domain, which is named Shock Response Spectrum (SRS) [22].

In shock response spectrum calculation, transient input time history data is applied as a base excitation to a series of single degree of freedom (SDOF) mass damper spring oscillators. The provided acceleration input is applied to the base of all oscillators and the maximum responses of each oscillator for own natural frequency compose the spectrum. In Figure 2.16, each single degree of freedom system has a unique set of distinguishing parameters; mass, $m$, damping constant, $c$, and constant of spring, $k$.

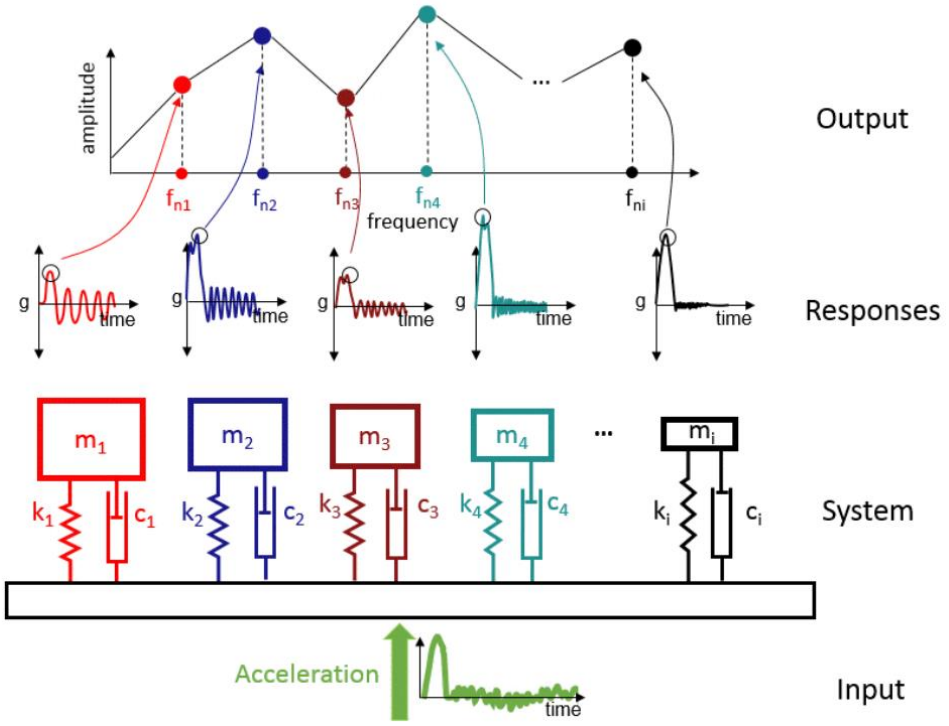


Figure 2.16. A shock response spectrum indicates the peak movement of a series of SDOF systems to a transient event [23]

SRS plots are displayed on a log-log scale and any set of random natural frequencies can be used to calculate the shock response spectrum. Typically, a proportional bandwidth such as $1/12$ octave is used. It means that each consecutive natural frequency is $2^{1/12}$ times the preceding frequency. In this study, National Instruments' LabVIEW platform is used to calculate SRS in the frequency range of 100 - 10,000 Hz. In this range, 81 SDOF systems are defined ($f_1$: 100, $f_2$: 105.95, $f_3$: 112.25, $f_4$: 118.92 ····· $f_{81}$: 10159.37).

SRS calculations are performed with a quality factor $Q = 10$ and the corresponding damping ratio of $\zeta = 5\%$ as specified in ISO 18431 [24].

Moreover, SRS calculation can be made by taking the time data's positive and negative direction or the absolute maximum. In this work, the absolute maximum value of the acceleration response, which is commonly used, is chosen.

In Figure 2.17, there are sinusoidal acceleration signals at 800 Hz, and corresponding SRS of them are plotted. There is varying amplification factor in the SRS graph with respect to signal form and number of periods at 800 Hz.

- Blue colored; is undamped signal.
- Green colored; damping ratio is %2.
- Red colored; damping ratio is %5.
- Turquoise colored; damping ratio is %10.

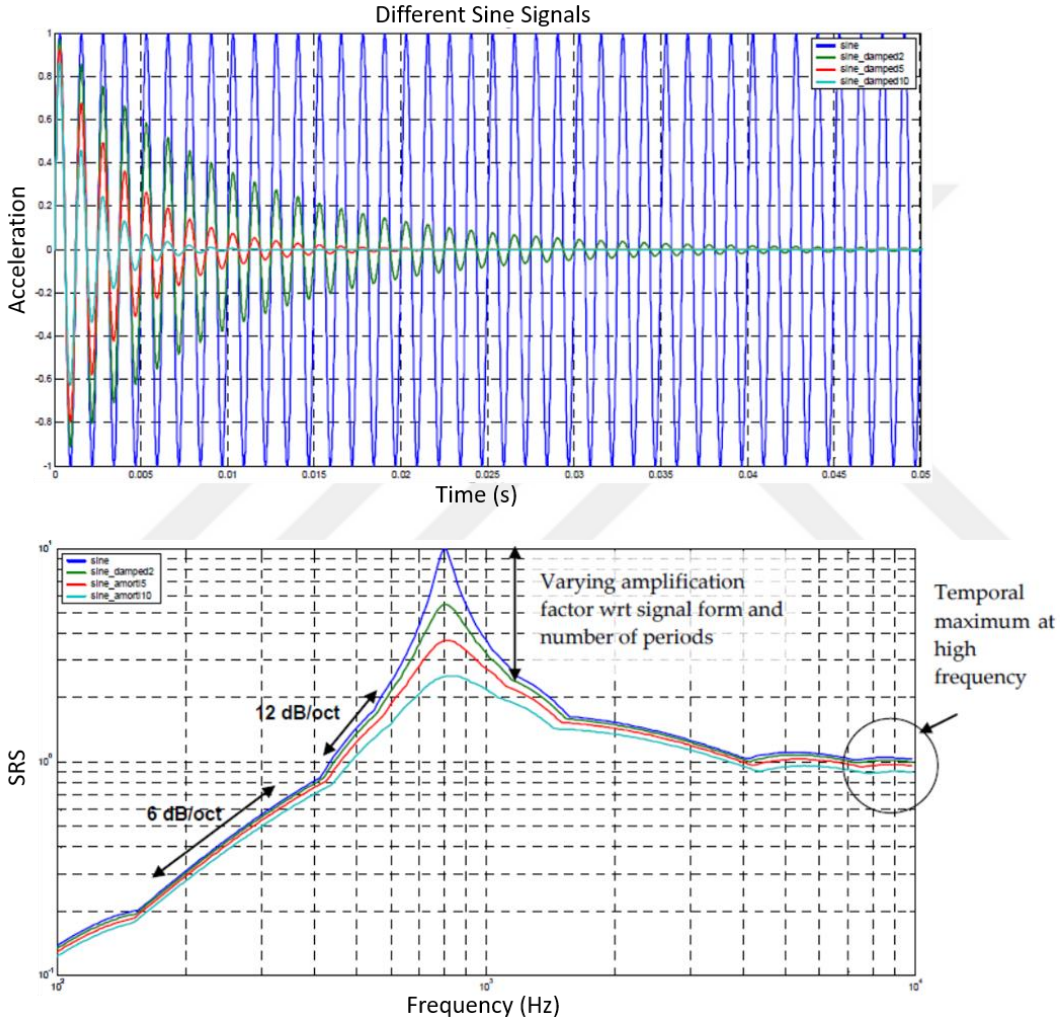


Figure 2.17. SRS plots of sine signals with different damping ratios [1]

A signal's amplification factor depends on the signal form, as seen in Figure 2.18. When the Q factor is considered to be 10 in the SRS calculation, the amplification factor usually varies between 1 and 6 times. If there is a perfect sine signal with a

sufficient number of periods, the corresponding value reaches up to 10. A shock spectrum response ($Q = 10$) based on a shock signal has an amplitude around 3 to 4 times of the time history peak due to the signal's transient (non-harmonic) nature [1].

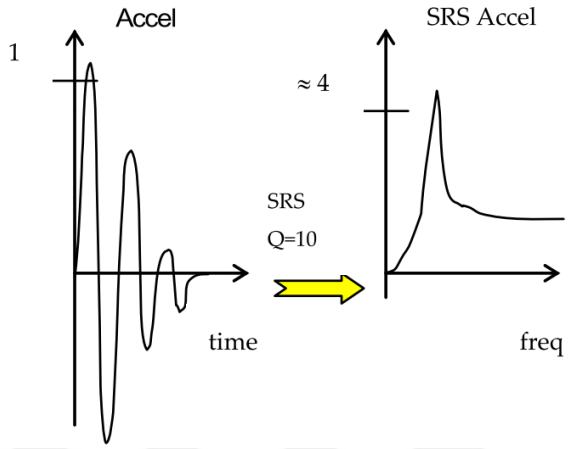


Figure 2.18. The relation between SRS peak amplitude and transient shock signal peak amplitude [1]

# CHAPTER 3

# INVESTIGATING THE EFFECT OF THE PYROSHOCK TEST PARAMETERS WITH FINITE ELEMENT ANALYSES

The parameters of a pyroshock test system are investigated in this chapter with the finite element modeling approach specified in Section 2.2.7.

Test system parameters are adjusted to obtain the appropriate SRS profile in the test infrastructure. Some of these parameters are not effective, and some are highly effective in obtaining the desired shock profile. Effective parameters are listed in Table 3.1. Since it would be difficult and costly to demonstrate the effect of each parameter in the experimental setup, some effects were observed using the appropriate FEA program. (ABAQUS) There are two different size of resonant plates in the test infrastructure. These are stated in Table 3.2.

Table 3.1 Test system parameters examined by finite element analysis

| Parameters | |
|---|---|
| Plate Thickness | Hammer Speed |
| Hammer Mass | Impact and Measurement Location |

Table 3.2 Resonant plate dimensions in the test facility

| No | Plate Dimension (mm) |
|---|---|
| 1 | 1000 x 1000 x 50 |
| 2 | 1500 x 1000 x 30 |

The experimental and analysis model of the first plate is shown in Figure 3.1 and Figure 3.2, also the second plate is shown in Figure 3.3 and Figure 3.4. The primary measurement points are presented. The distance between nodes is 125 mm on the first plate and 120 mm on the second plate. In this study, when defining location points in other chapters, Figure 3.2 and Figure 3.4 are taken as reference.

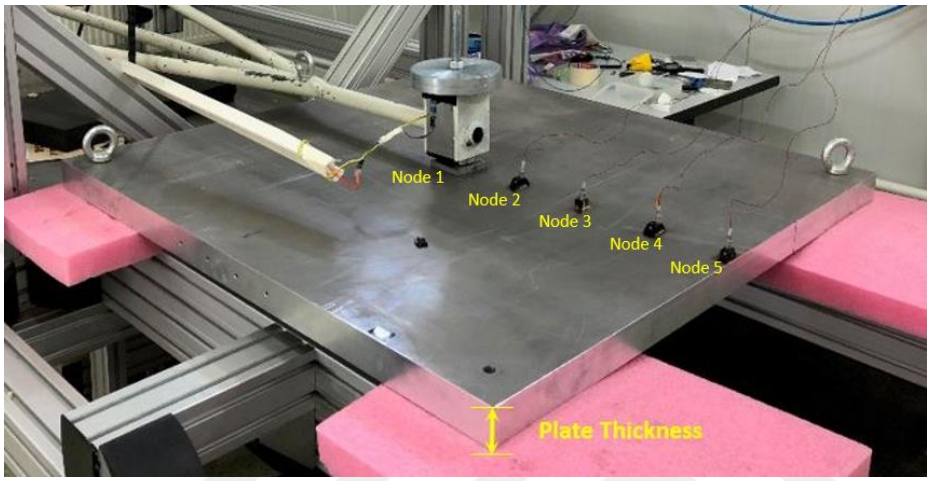


Figure 3.1. 1000x1000x50 $mm^3$ resonant plate pendulum-type test system configuration

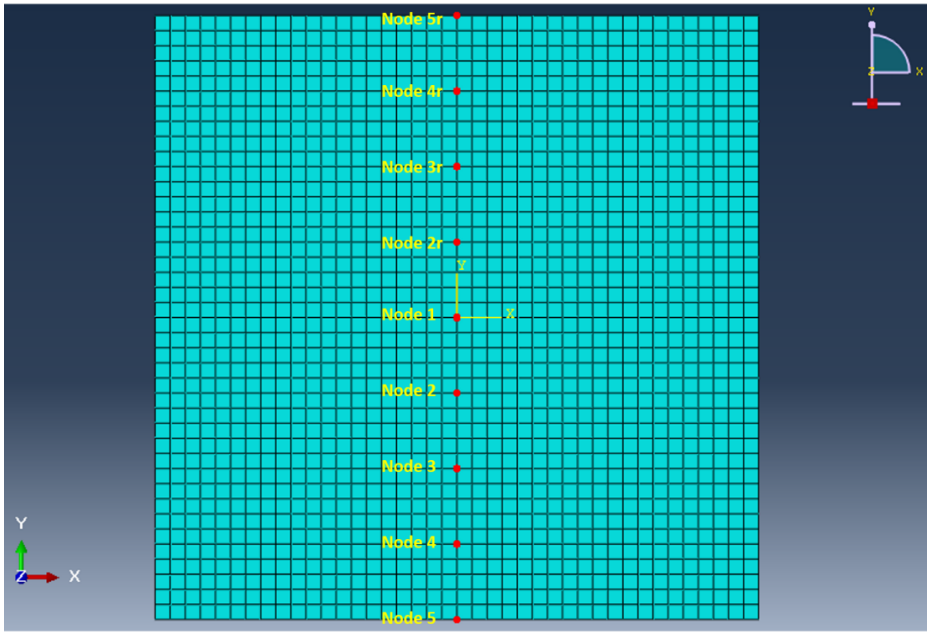


Figure 3.2. 1000x1000x50 $mm^3$ plate analysis model measurement points

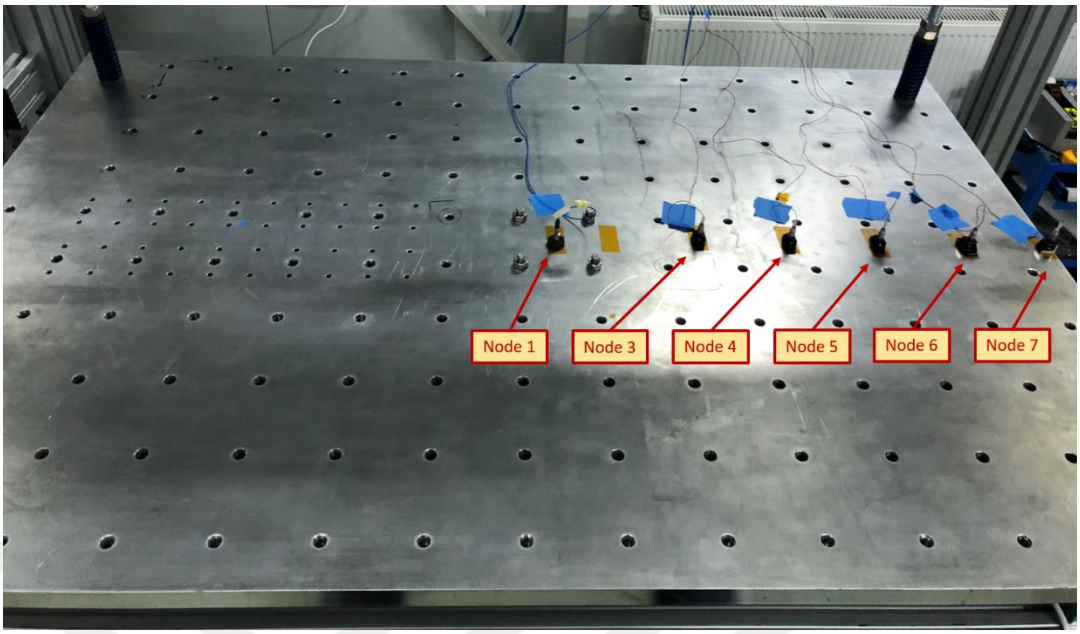


Figure 3.3. 1500x1000x30 $mm^3$ resonant plate pneumatic test system configuration (side view)

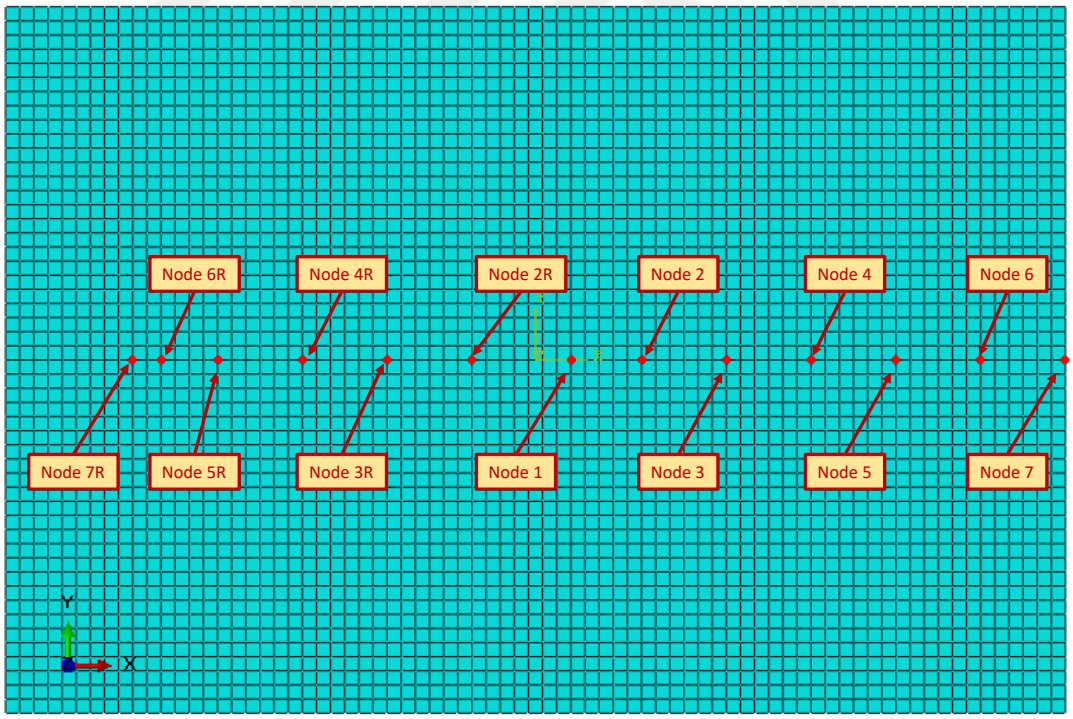


Figure 3.4. 1500x1000x30 $mm^3$ plate analysis model measurement points

## 3.1 Hammer (Projectile) Speed

The most important parameter influencing the SRS profile of the shock test is impact speed. Firstly, the impact model was created to observe the contact force, shown in Figure 3.5. By increasing impact speed, the amplitude of the half-sine rises which is generated during impact, as seen in Figure 3.6.

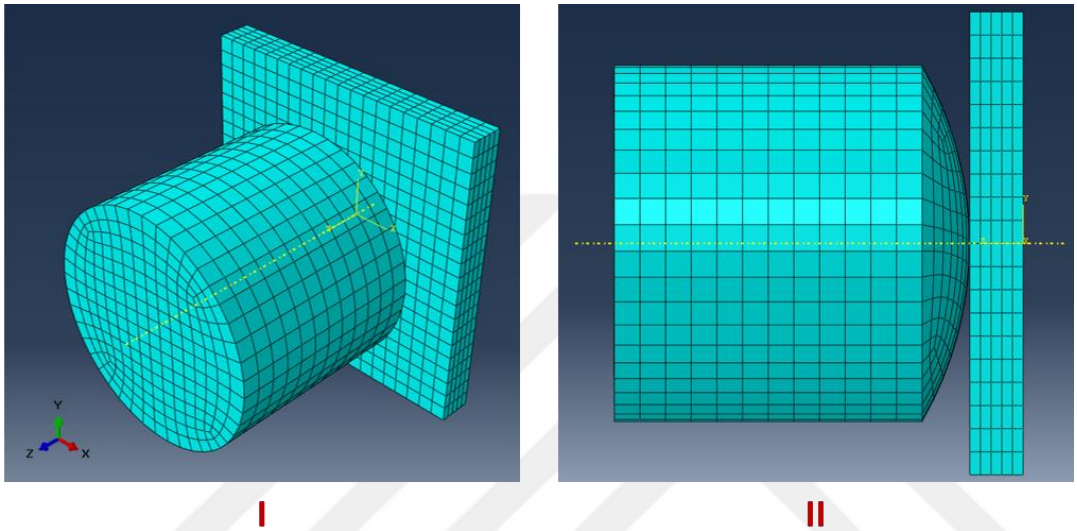


Figure 3.5. FEA impact model of hammer and plate (I: Isometric view, II: Side view)

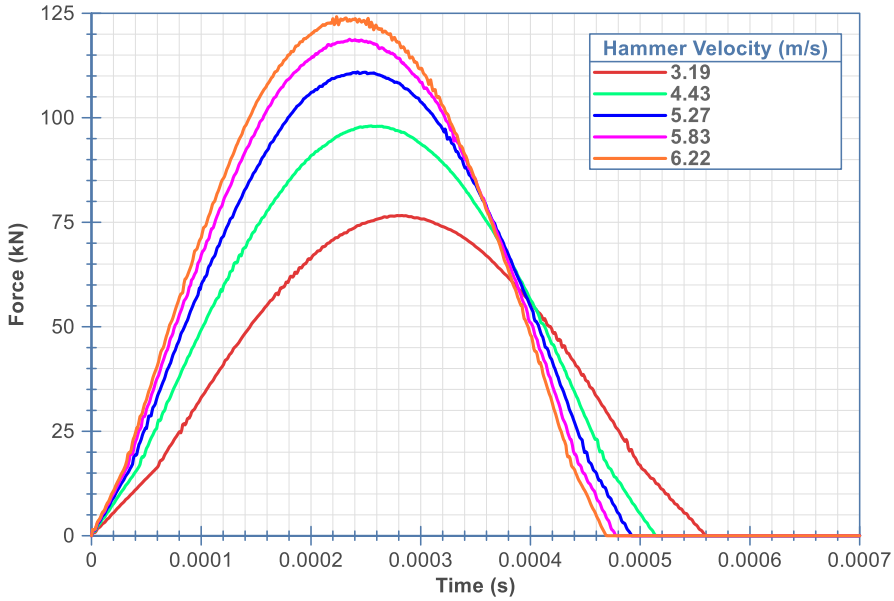


Figure 3.6. FEA result of contact force graph with different velocities

In Figure 3.7, two half-sine waves are generated with different amplitudes, and they are separately applied as a concentrated force from node 1 location of the resonant plate. Then, the entire profile shifts up to a certain extent without changing the shape of the SRS. The results are indicated in Figure 3.8 and Figure 3.9. Straight lines appearing in figures are estimated shock profiles of each SRS data. Detailed information about its calculation is described in Section 4.2.1.3.

In a pneumatic shock test system, impact speed is controlled by the pressure of the air tank. Besides, in the pendulum type shock test system, it is controlled by the angle of the pendulum.

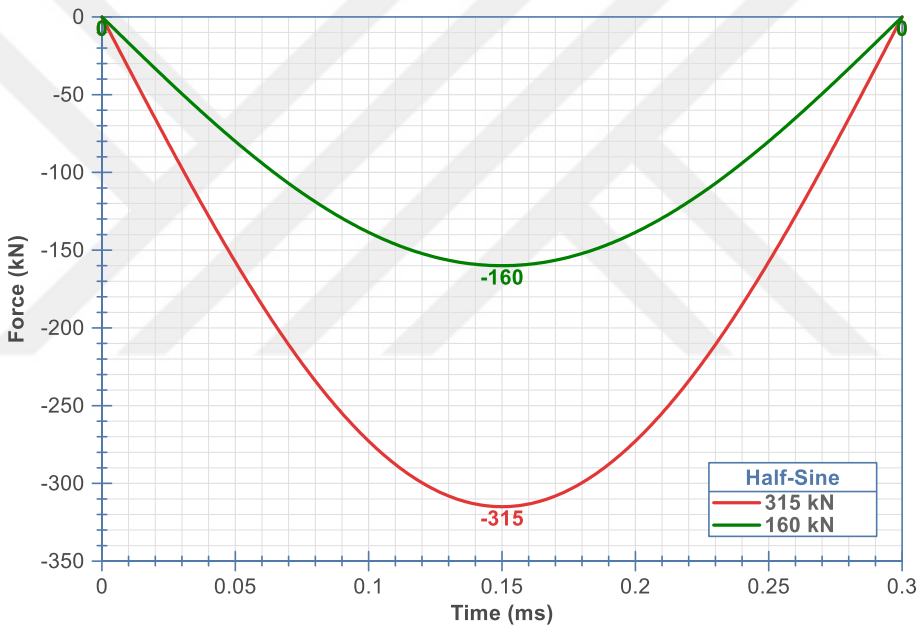


Figure 3.7. Input half-sine, 160kN & 315kN in 300 µs

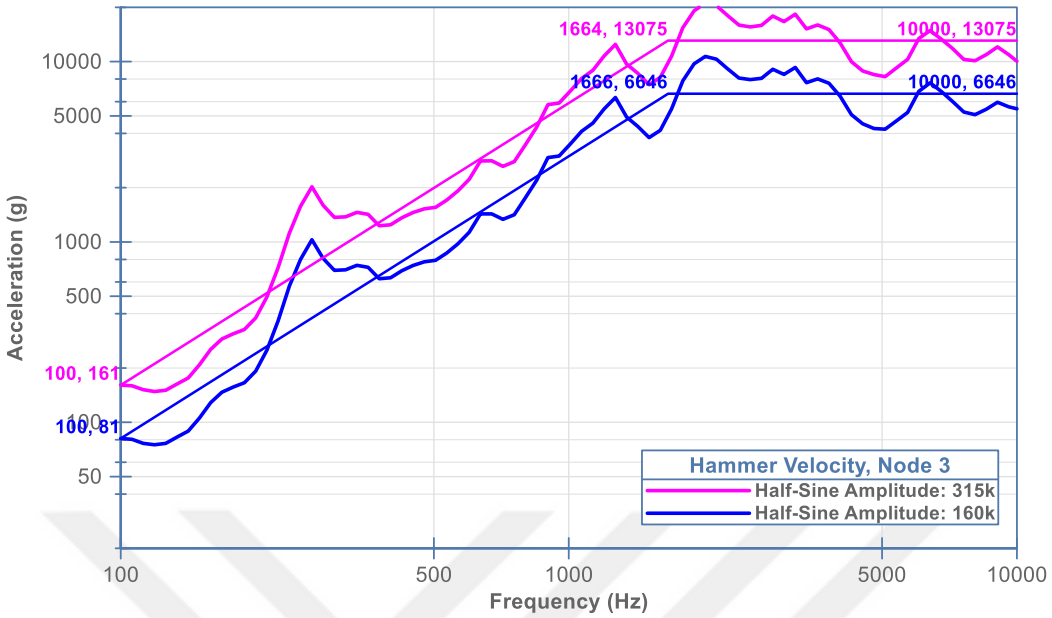


Figure 3.8. FEA results of impact speed using 1500x1000x30 $mm^3$ plate at node 3

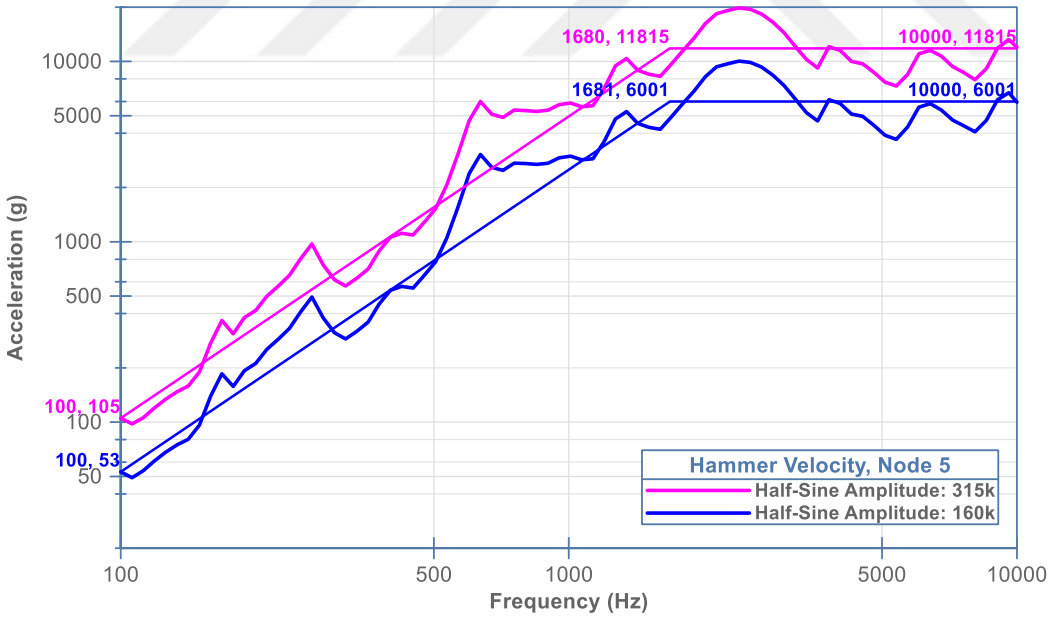


Figure 3.9. FEA results of impact speed using 1500x1000x30 $mm^3$ plate at node 5

## 3.2 Hammer Mass

Hammer mass has an effect on the half-sine. With heavier hammer mass, amplitude, and duration of half-sine increase. Impact analysis were made to see the effect, and results are given in Figure 3.10. This change in half-sine can be interpreted as an increase in low frequencies and a decrease in high frequencies in SRS. In other words, hammer mass has a booster effect on low frequencies under knee frequency. This is shown in Figure 3.11, where the mass effect is simulated by creating a sample two pulse. A half-sine pulse of 315 kN amplitude and 300 ms duration was compared with a 360 kN amplitude and 300 ms duration pulse.

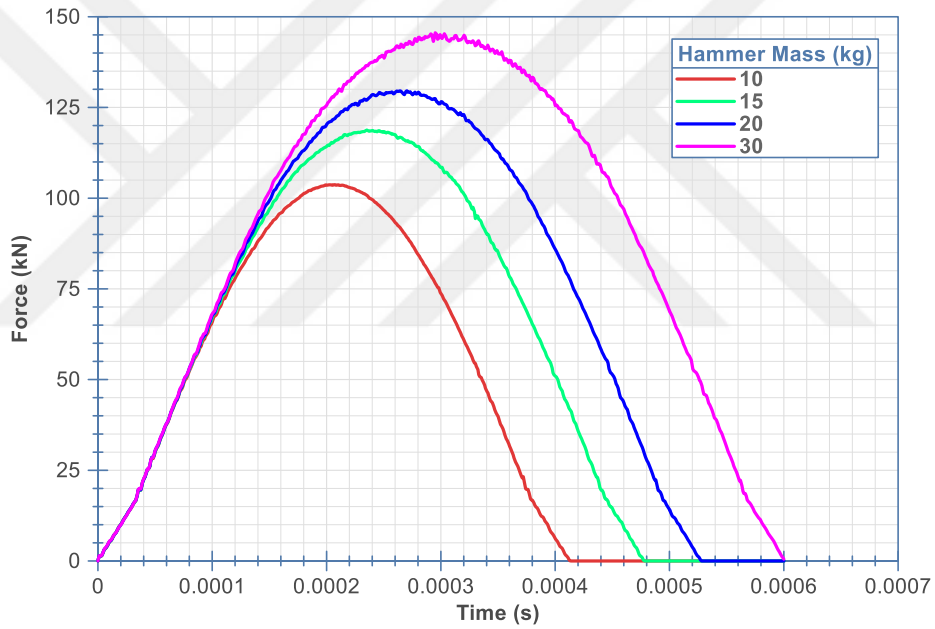


Figure 3.10. FEA result of contact force graph with different hammer mass

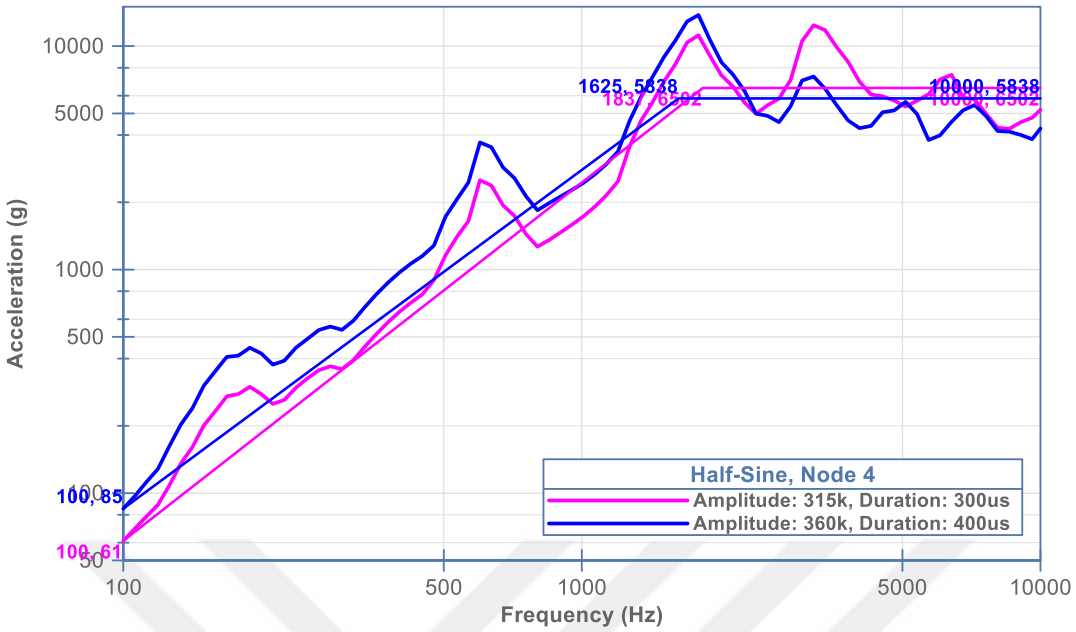


Figure 3.11. FEA results of hammer mass using 1000x1000x50 $mm^3$ plate at node 4

## 3.3 Plate Thickness

The thickness of the resonant plate significantly affects the shock test profile. Resonant plates can be used in various thicknesses. Models of different thicknesses are created, and the results are compared.

In the size of 1000x1000 mm plate, this effect is shown in Figure 3.12. The data obtained at all points of this plate are stated in Table 3.3. One of the notable point about this figure is that a dominant mode appeared at 315 Hz in the 100 mm thick plate. This is undesirable in tests because if the equipment is placed in that area, it will be subjected to a severe load at 315 Hz. Secondly, 30 mm plate is unfavorable in this position since the acceleration level is high in the initial frequency.

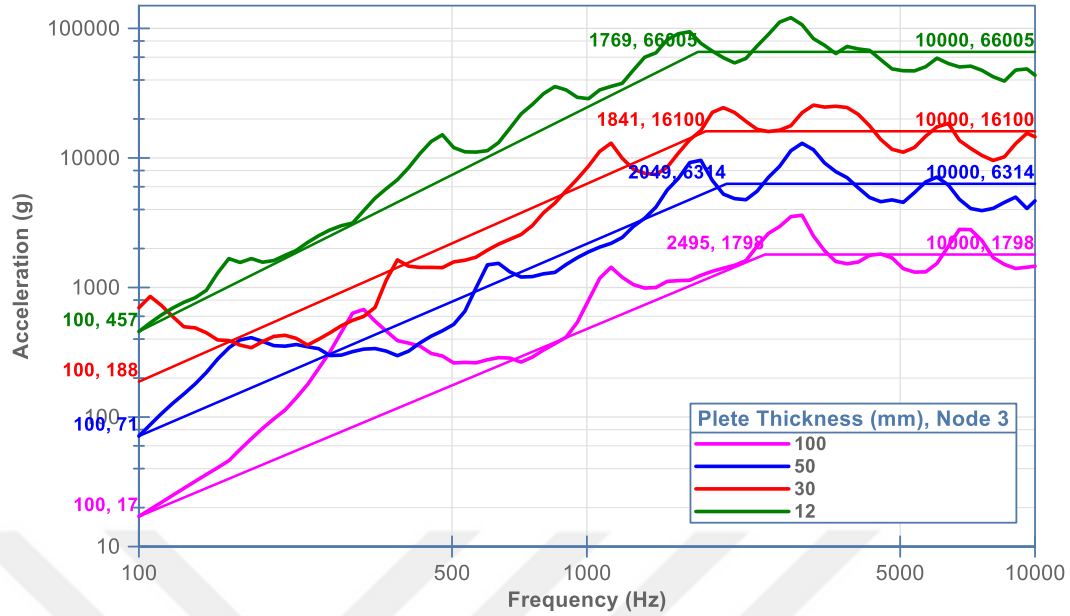


Figure 3.12. FEA results of plate thickness using a 1000x1000 mm$^2$ plate at node 3

Plate thickness effect in the 1500x1000 mm plate size is indicated in Figure 3.13, in the size of the 2000x1000 mm plate shown in Figure 3.14. Acceleration values increase in all frequencies, and peaks occur at some frequencies according to the structure's modal response.

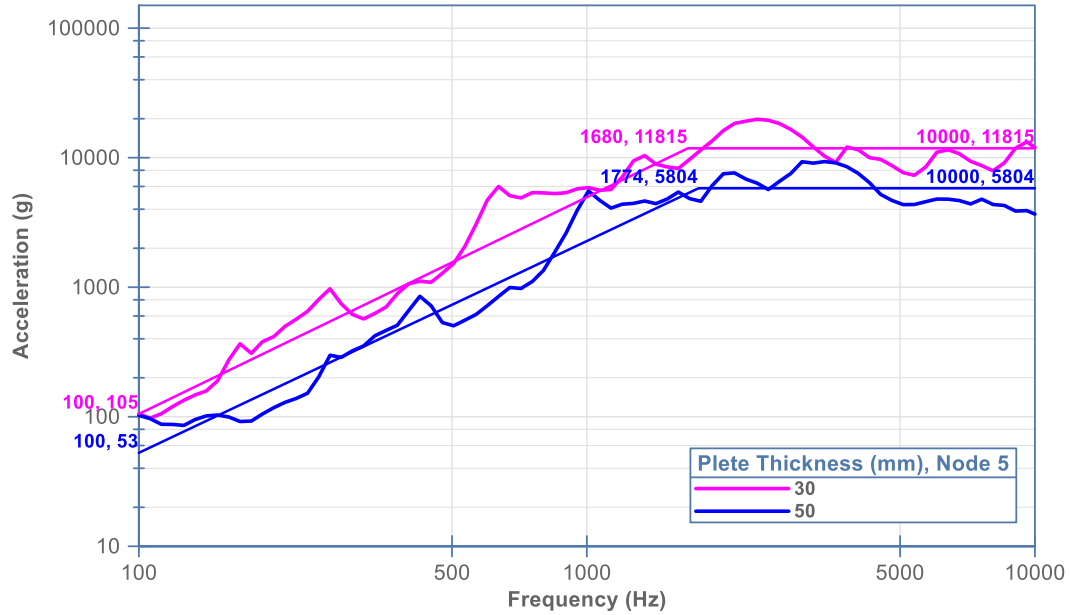


Figure 3.13. FEA results of plate thickness using a 1500x1000 mm$^2$ plate at node 5

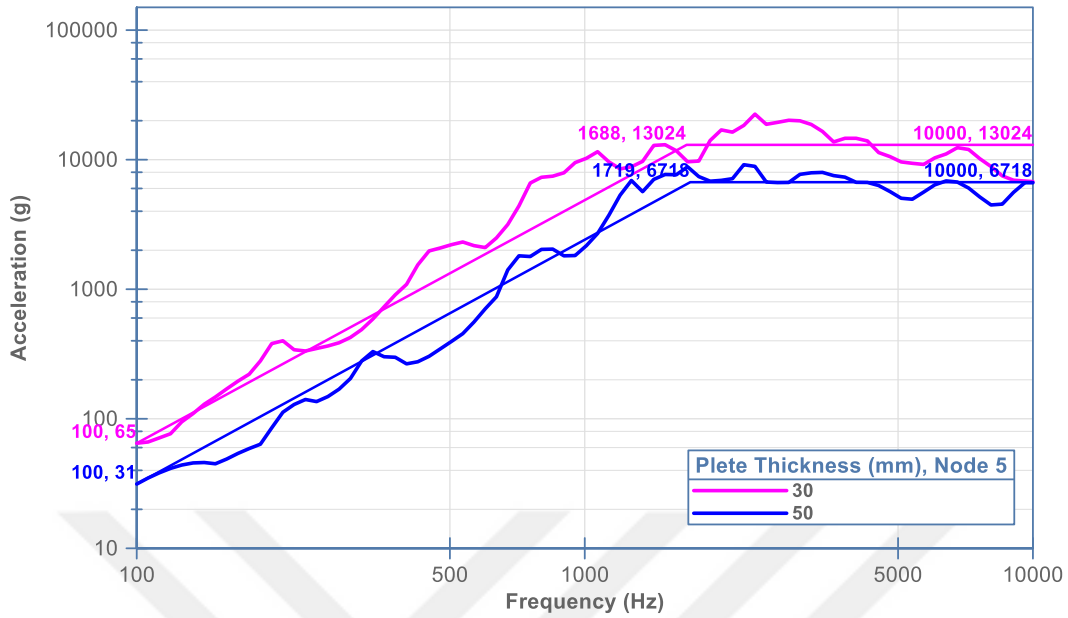


Figure 3.14. FEA results of plate thickness using a 2000x1000 $mm^2$ plate at node 5

Consequently, an appropriate plate thickness has to be determined according to the desired shock range of interest. As the thickness gets thinner, it increases the intensity of the shock and also generally shifts the knee point to the left. Another result in this parameter is that if the test system's speed is limited and aims to achieve high acceleration values, the targeted levels can be reached without changing the impact system by using thin plates.

Table 3.3 FEA results of plate thickness in 1000x1000 $mm^2$ plate

| 1000x1000 Plate Thickness | | | | |
|---|---|---|---|---|
| Measurement Point | Plate Thickness (mm) | Initial Acceleration At 100 Hz (g) | Knee Frequency (Hz) | Knee Acceleration (g) |
| Node 1 (Mid-Point) | 12 | 863 | 1889 | 148503 |
| | 30 | 295 | 1766 | 30406 |
| | 50 | 117 | 1799 | 15265 |
| | 100 | 26 | 2843 | 4792 |
| Node 2 | 12 | 612 | 1931 | 60431 |
| | 30 | 220 | 1779 | 13231 |
| | 50 | 98 | 1478 | 6882 |
| | 100 | 23 | 2220 | 2653 |
| Node 3 | 12 | 457 | 1769 | 66005 |
| | 30 | 188 | 1841 | 16100 |
| | 50 | 71 | 2049 | 6314 |
| | 100 | 17 | 2495 | 1798 |
| Node 4 | 12 | 794 | 1889 | 46965 |
| | 30 | 172 | 1486 | 12877 |
| | 50 | 65 | 1803 | 7036 |
| | 100 | 14 | 2386 | 1973 |
| Node 5 (Edge-Point) | 12 | 1407 | 1732 | 126607 |
| | 30 | 222 | 1895 | 27095 |
| | 50 | 74 | 1863 | 13045 |
| | 100 | 18 | 1595 | 3255 |

## 3.4 Impact and Measurement Location

The tuning point of the resonant plate affects how much individual modes are amplified or weakened. The test item can be located at any place according to the desired SRS profile on the resonant plate except for the impact point [1, Ch. 13.3.4.1.1, a].

The figures below show the measurement results at the various impact location. Modes of the resonant plate are amplified or weakened by changing the impact point.

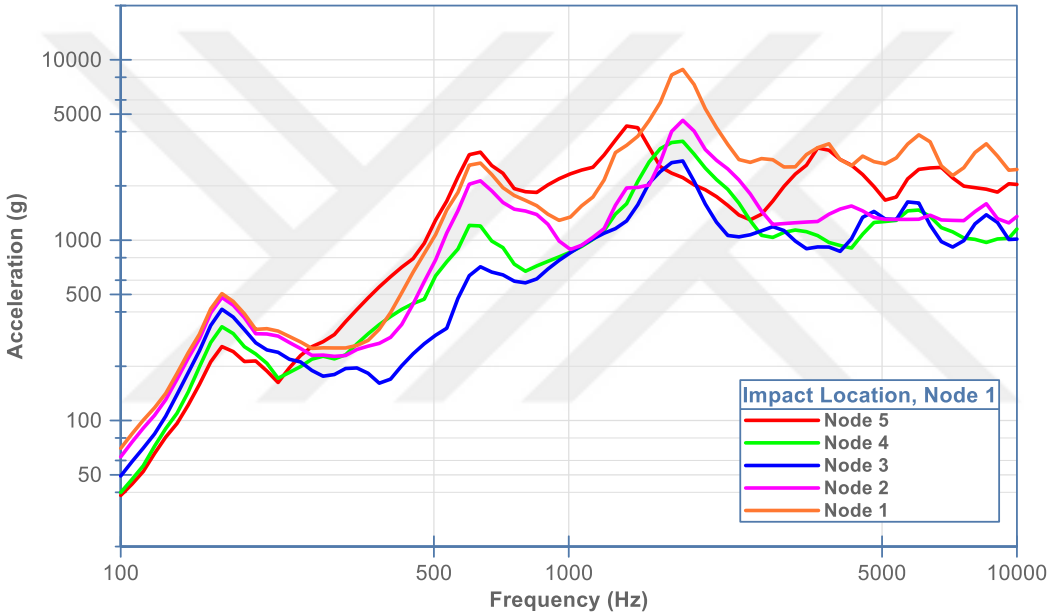


Figure 3.15. FEA result of impact location using 1000x1000x50 $mm^3$ plate at node 1

In Figure 3.15, the impact was carried out from Node 1, and measurements were taken from five points. In the first mode at 168 Hz, the amplitude decreases from 506 g to 257 g as the measurement point moves away from the impact location. In the second mode at 635 Hz, the amplitude varies from 712 g to 3016 g. The amplitude is the lowest value in the Node 3 zone, while the highest value in the Node 5 zone. The edge effect appears at Node 5 since it is on the edge of the plate. In the third mode at 1800 Hz, the amplitude varies from 2752 g to 8855 g. Points closer to the

impact location appear to be more affected in this mode. The knee points of these data determined by the Estimated Knee Point (EKP) approach are shown in Figure 3.16. The EKP approach is described in section 4.2.1.3.

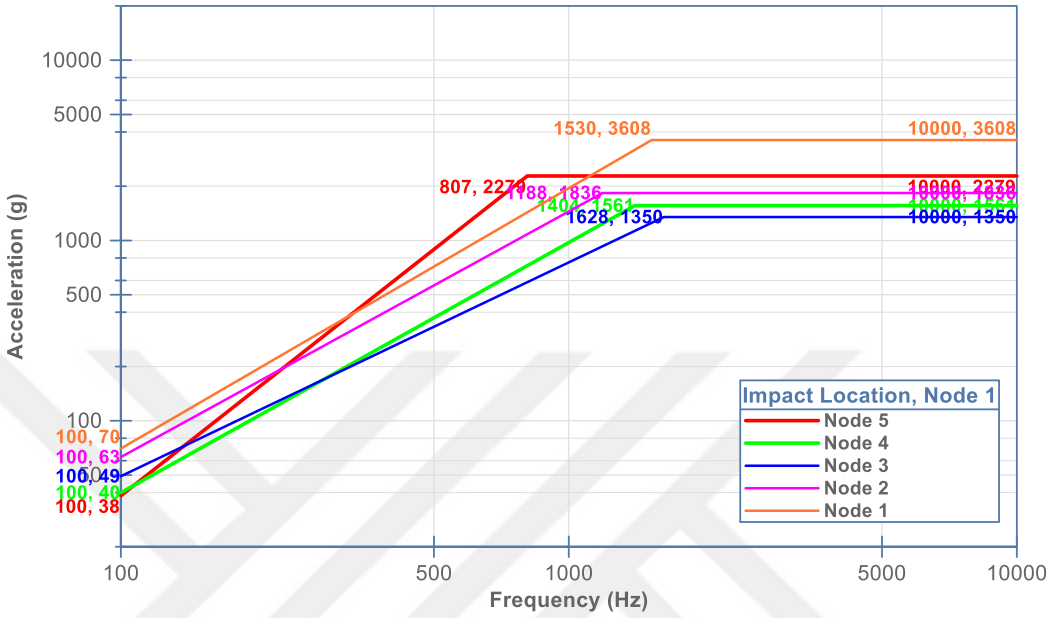


Figure 3.16. FEA result with EKP representation of impact location using 1000x1000x50 $mm^3$ plate at node 1

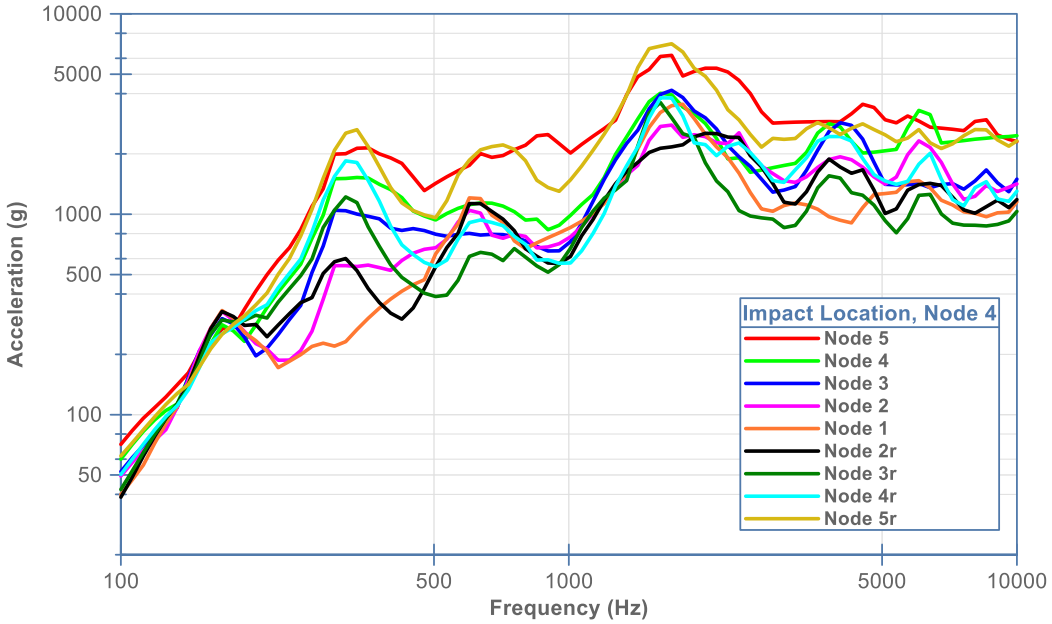


Figure 3.17. FEA result of impact location using 1000x1000x50 $mm^3$ plate at node 4

The impact was carried out from Node 4 in Figure 3.17, and measurements were taken from nine points. In the first mode at 168 Hz, there was no significant amplification. In the second mode at 318 Hz, the amplitude is the lower value in the middle of the plate, while the highest value in the edge of the plate. The edge effect appears at Node 5 and Node 5r. In the third mode at 600 Hz, there is amplification only in the middle zone. In the fourth mode at 1600 Hz, there is amplification in all of the locations, but edge nodes are noticeably high.

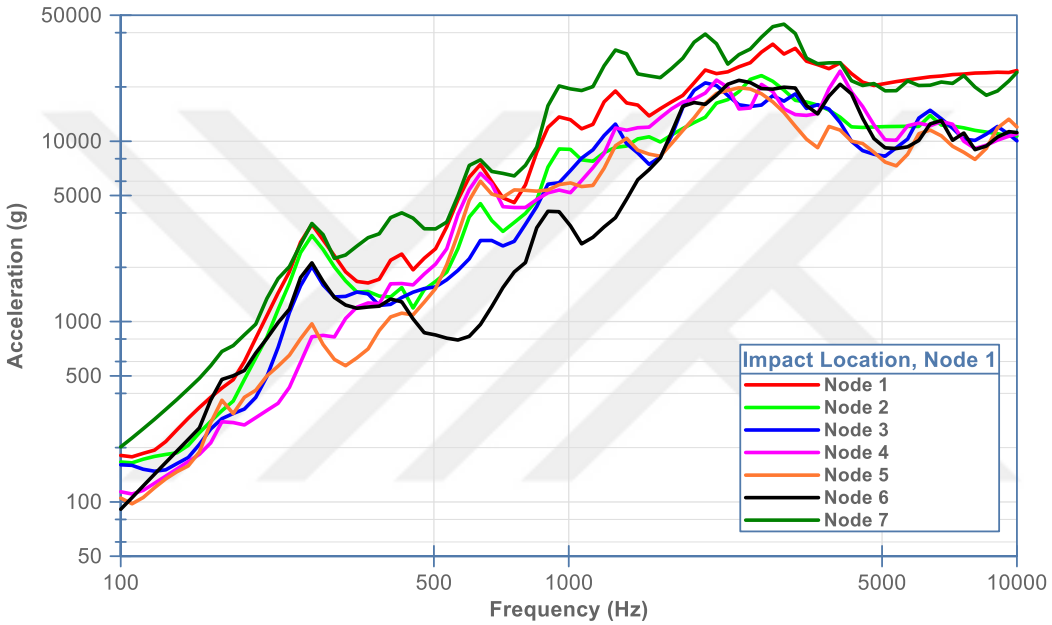


Figure 3.18. FEA result of impact location using 1500x1000x30 $mm^3$ plate at node 1

The impact was carried out from Node 1 in Figure 3.18, and measurements were taken from seven points. First mode of the plate (267 Hz) is not severely amplified at Node 4 and Node 5 locations. There is only slightly amplification in the second mode (635 Hz). This region provides suitable conditions for testing.

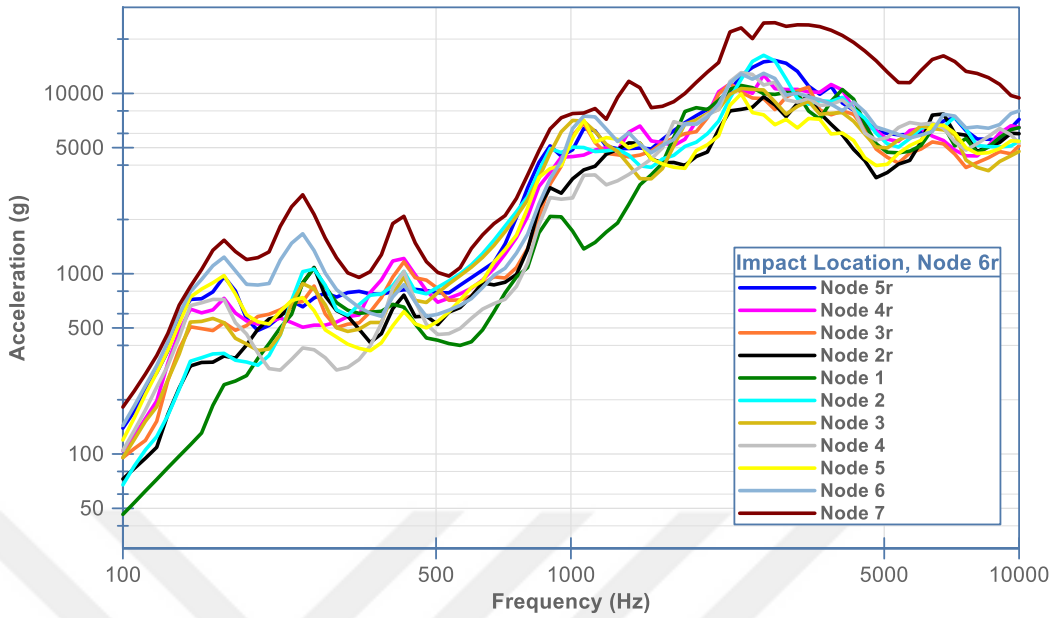


Figure 3.19. FEA result of impact location using 1500x1000x30 $mm^3$ plate at node 6R

The impact was carried out from Node 6r in Figure 3.19, and measurements were taken from eleven points. There is high amplification at low frequencies except for the middle region. The test equipment should be placed in the middle of the plate in this configuration.

# CHAPTER 4

# EXPERIMENTAL STUDIES

This chapter first investigates forces that occur at the time of the impact. For this purpose, a force measurement test setup was established, and various impact scenarios were discussed. Then, pyroshock tests by mechanical impact method were examined, performed in various configurations in the pendulum type and pneumatic type system. In these tests, the effects of different parameters on SRS are investigated experimentally. Finally, with the pyrotechnic shock test, the shock levels emitted by a source were monitored.

## 4.1 Force Measurement Tests

High levels of force are generated during the impact of the hammer in the form of half-sine, as shown in Figure 4.1. Since the collision takes place in a very short duration, the momentum of the object turns into a high force. The difference in momentum (or impulse $J$) between periods $t_1$ and $t_2$ is that the net force encountered by a particle varies as a function of time, $F(t)$.

$$\Delta p = J = \int_{t_1}^{t_2} F(t)dt \tag{4-1}$$

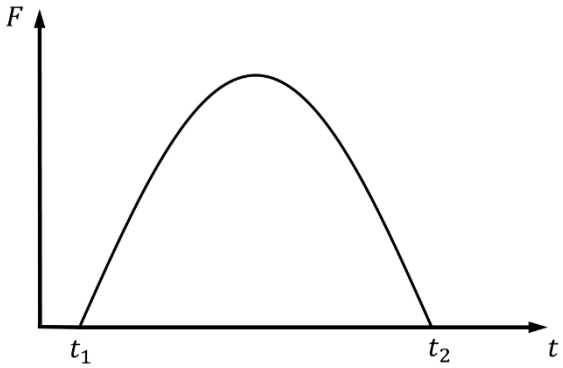


Figure 4.1. Sample half-sine force plot

This force is reflected as an input to the FEA model. In the preliminary studies of the research, information about the force started with the data from FEA impact model and the literature. Afterward, precise force measurements were made using the piezoelectric type force sensor to verify the FEA model with test configuration.

### 4.1.1 Hardware and Setup

The hardware used in the tests is listed in Table 4.1, and the test configuration is shown in Figure 4.2. A force sensor is used for measuring dynamic and quasistatic compressive forces. It can measure up to a force magnitude of 300 kN. It is sensitive to transient loads since this transducer is a piezoelectric type sensor. Straingage based force sensors are widely available but are not suitable for transient pulse measurements because their time constants are not short enough to catch the 20 ms pulse. Data were collected at a sampling rate of 900kHz during the tests.

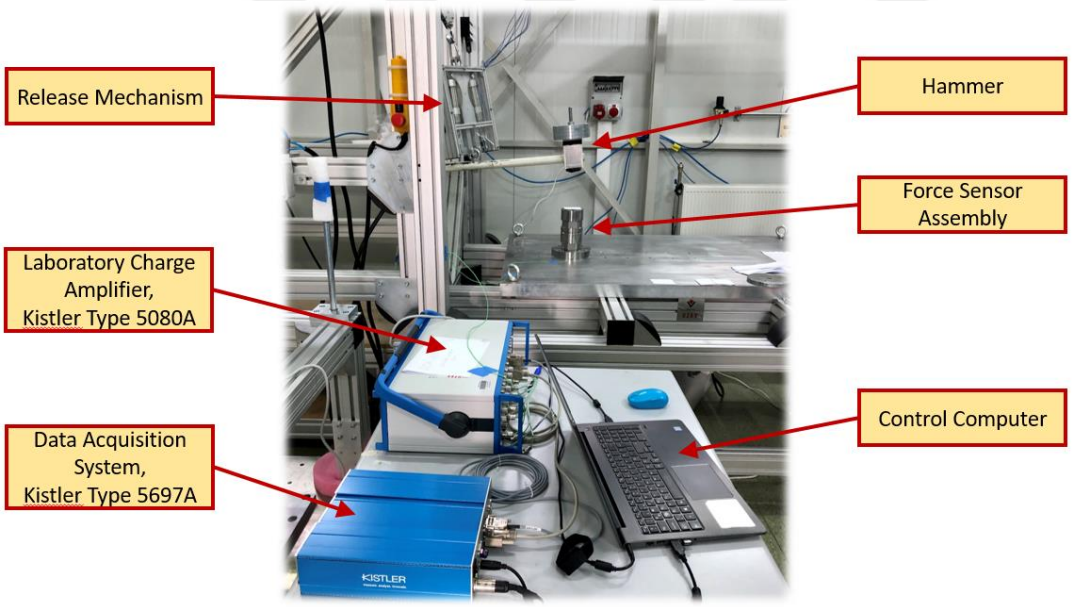


Figure 4.2. Force measurement test setup

Table 4.1 Force measurement equipment list, brand, model and sensitivities

| Equipment | *Brand* | *Model* | *Sensitivity* |
|---|---|---|---|
| Force Sensor | Kistler | 9383A | -1.966 pC/N |
| Charge Amplifier | Kistler | 5080A | - |
| Data Acquisition System | Kistler | 5697A | - |

The green-colored mechanical adapters shown in Figure 4.3 were produced and mounted on the test setup for the assembly of the force sensor. The stationary position of the hammer and force sensor is shown in Figure 4.4.

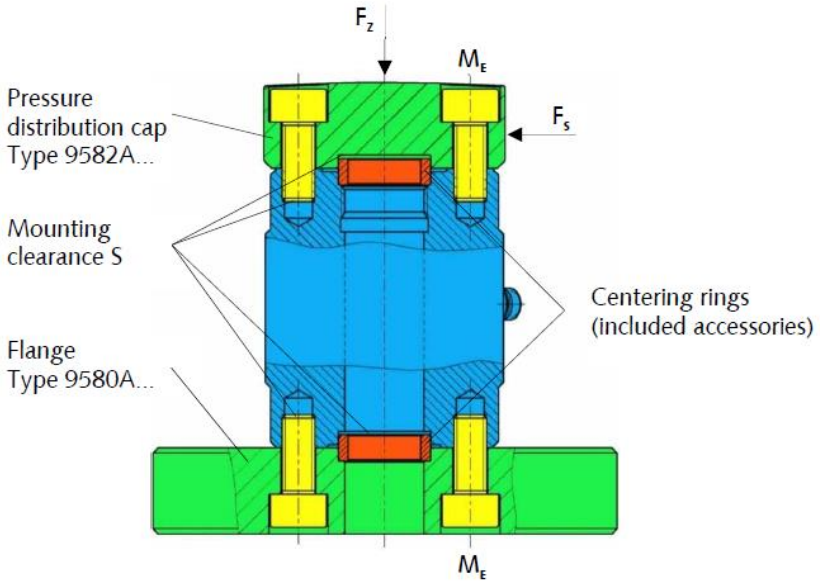


Figure 4.3. Force sensor assembly [25]

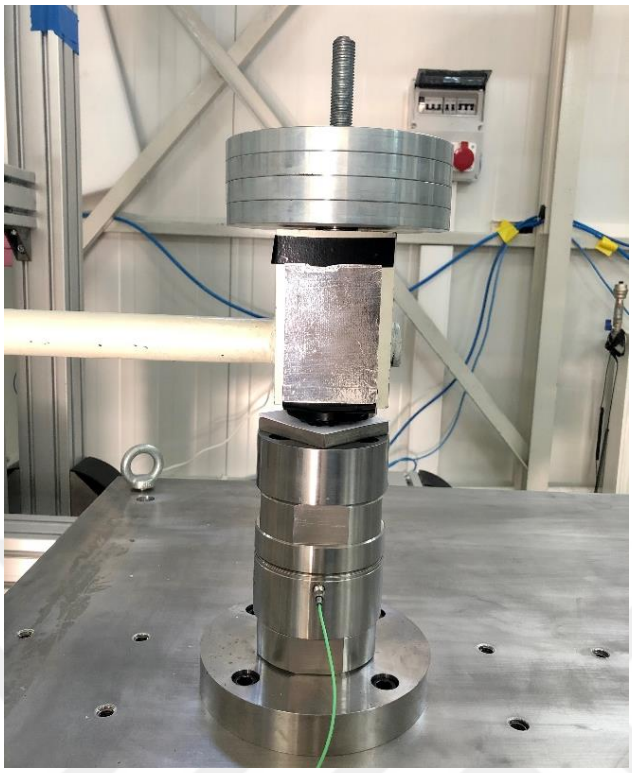

Figure 4.4. 19.30 kg hammer in a stationary position at the top of the force sensor

### 4.1.2 Measurement Parameters

#### 4.1.2.1 Hammer Speed

The force-time graph obtained by increasing the hammer height from 5 degrees to 10 degrees is shown in Figure 4.5. At the moment of impact, 5 degrees corresponds to a speed of 1.735 m/s, while 10 degrees corresponds to a speed of 2.45 m/s. A similar result was obtained as a result of the FEM analysis in Figure 3.6.

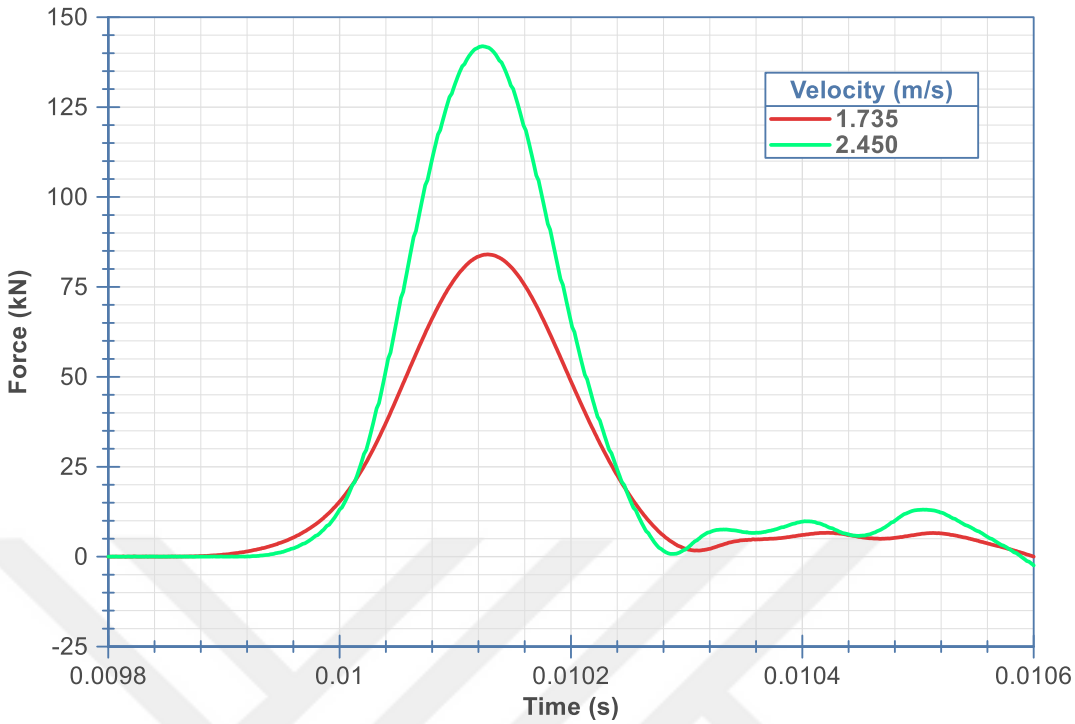


Figure 4.5. FMT result of impact speed

#### 4.1.2.2 Hammer Mass

Hammer configurations of different masses are shown in Figure 4.6, and the results of the mass increase are given in Figure 4.7. The amplitude appears to remain at a similar level, but the duration of the pulse extends. When we compare with the FEA results in Figure 3.10, it is seen that close results are obtained. However, test results show that the level decreased slightly and rose again. It is thought that there is an inertia effect due to the design of the hammer. If there were a one-piece spherical hammer design, a more half-sine-like shape would be obtained.

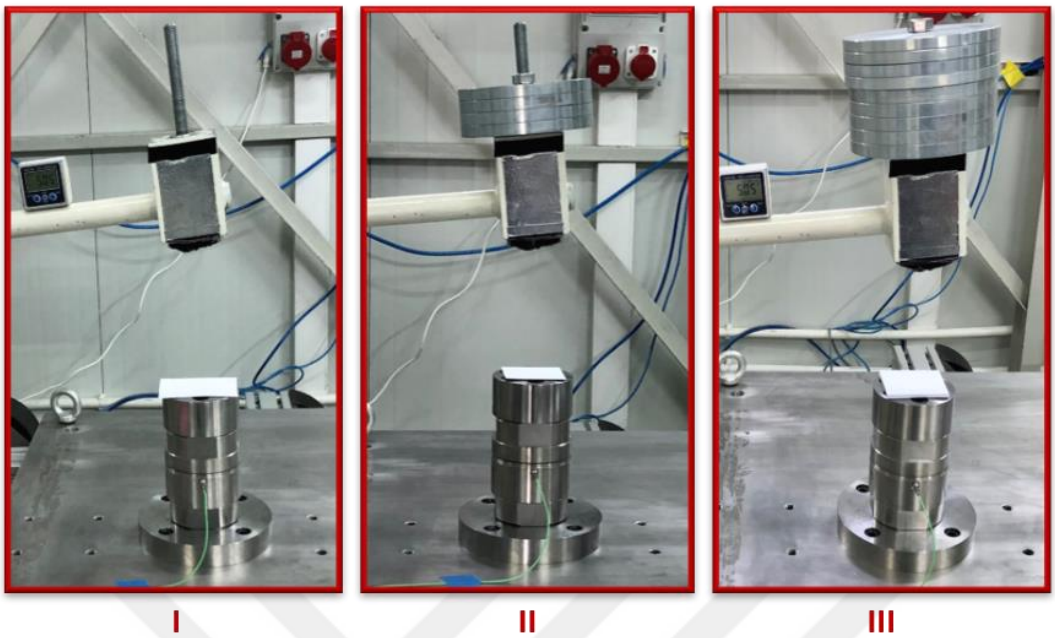


Figure 4.6. Hammer with three different mass (I: 10.8 kg, II: 19.3 kg, III: 29.4 kg)

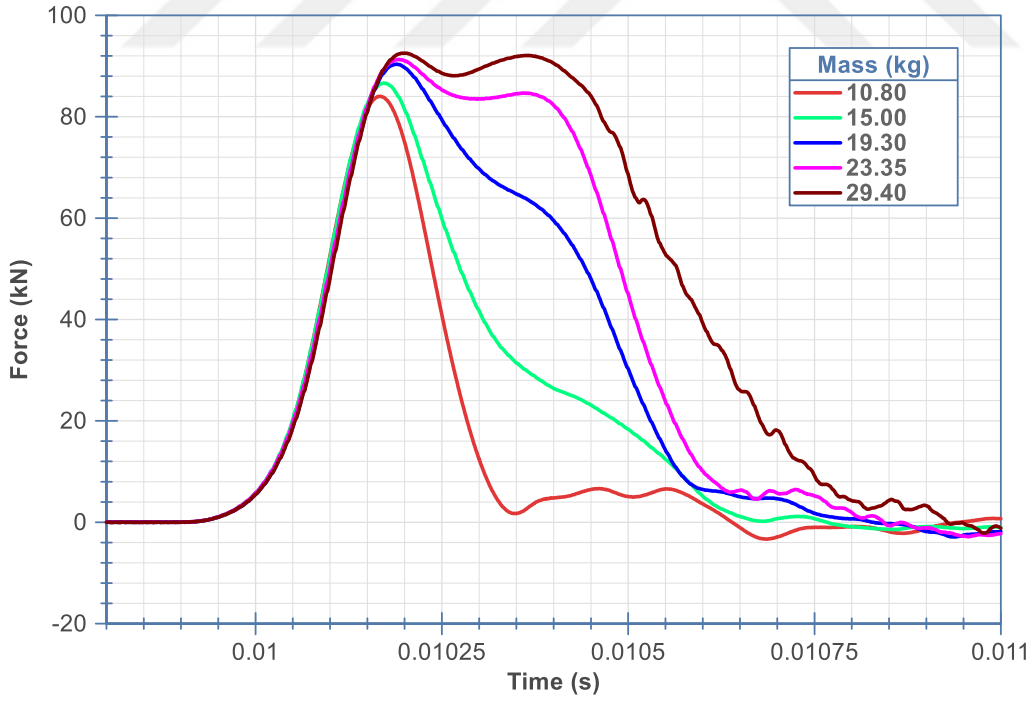


Figure 4.7. FMT result of hammer mass

Figure 4.8 shows the 15 kg hammer's half-sine profiles at the same speed in both analysis and test configurations. The analysis estimate appears to be significantly different from the test measurement. As a result of applying these force profiles to the resonant plate on the FEA model, SRS graphics in Figure 4.9 were obtained.

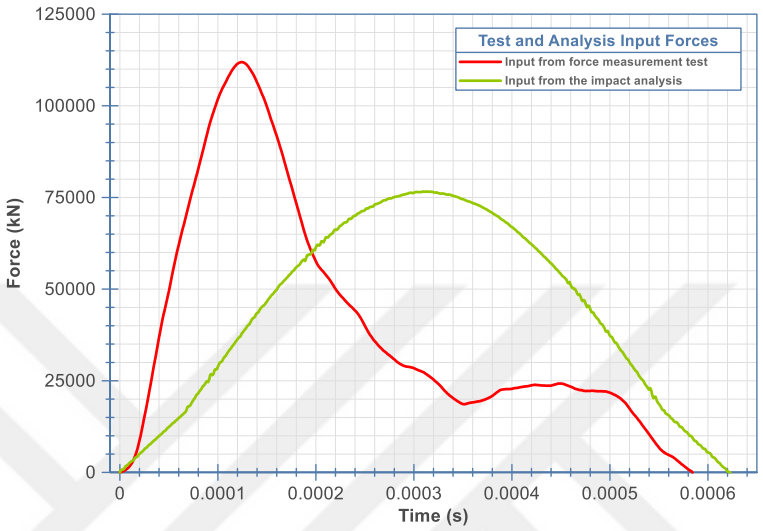


Figure 4.8. 15 kg hammer test and analysis impact force profiles

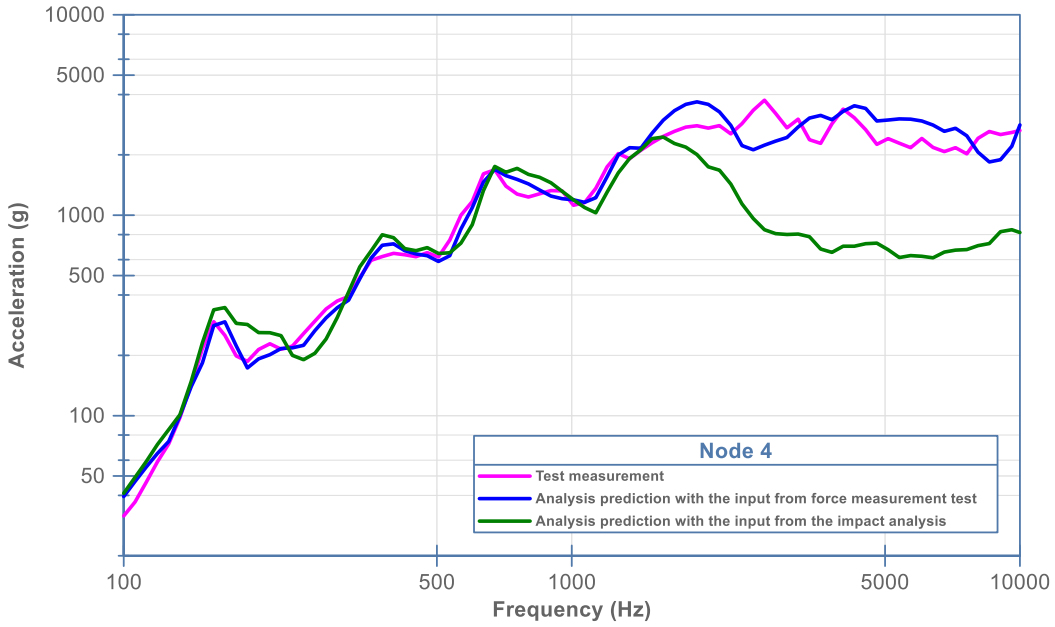


Figure 4.9. SRS plots obtained with test and analysis impact force profiles of 15 kg hammer.

The use of force profile obtained from the impact analysis in Figure 4.8 remains significantly low after 1700 Hz. The direct application of the half-sine profile obtained from the F.M.T. to the resonant plate shock analysis provided accurate results in the entire spectrum. Consequently, the actual half-sine profiles obtained from the force measurement test have great importance in getting accurate results in the analyzes performed in this study.

#### 4.1.2.3 Impact Plate and Mechanical Filter Material

As it is known, the material of the impact surface directly affects the pulse profile. Various impact plates and mechanical filters have been tested for this purpose. Sheet paper produced the most consistent and repeatable results among them.

The effect of placing a certain number of papers is shown in Figure 4.10. The force distribution at the moment of impact can be precisely controlled. The desired pulse profile can easily be adjusted.

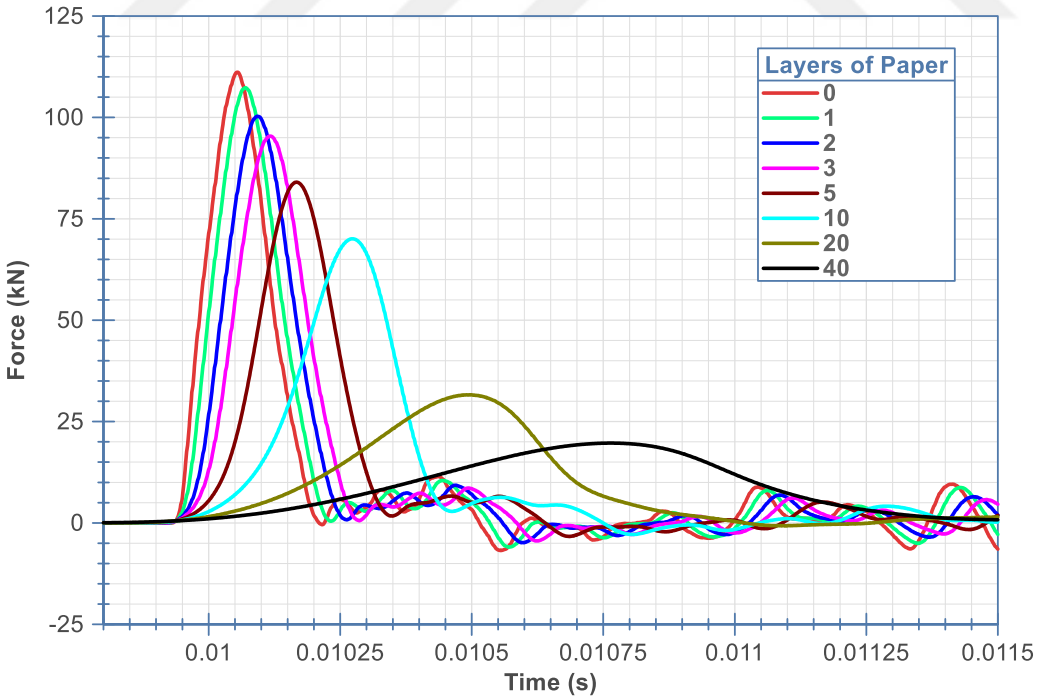


Figure 4.10. FMT result of sheet paper layers as a mechanical filter

Various impact plate materials have been tested, shown in Figure 4.11. The results are shown in Figure 4.12.

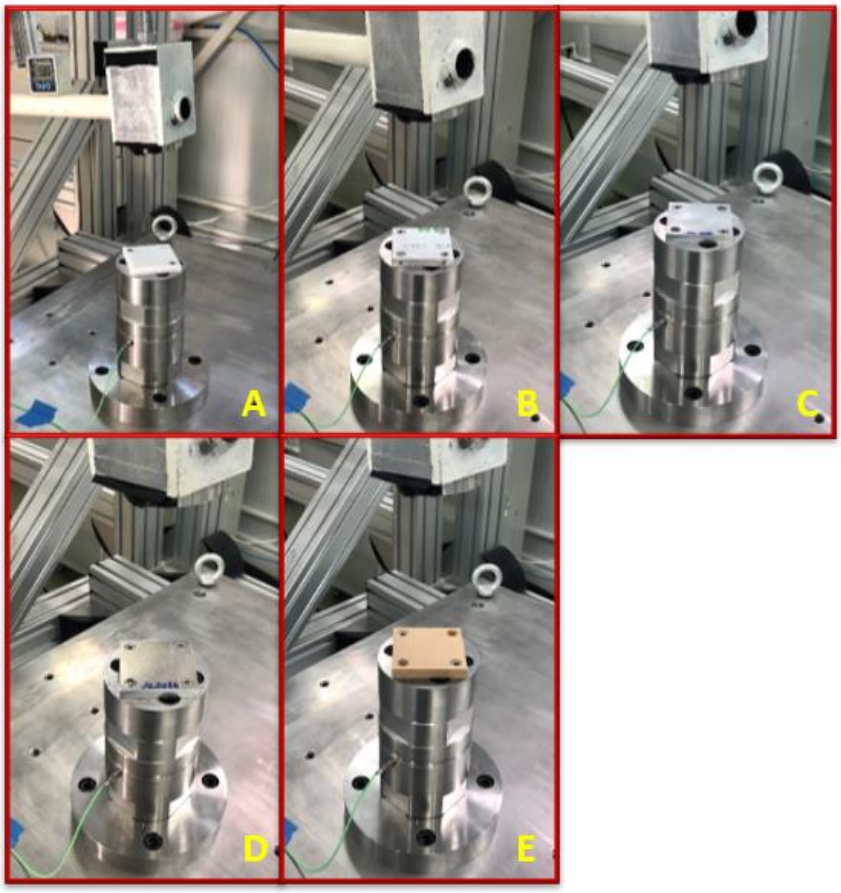


Figure 4.11. Various impact plate materials: A) White Delrin, B) Plexiglass, C) Aluminum 6061, D) Aluminum 2024, E) Hardboard

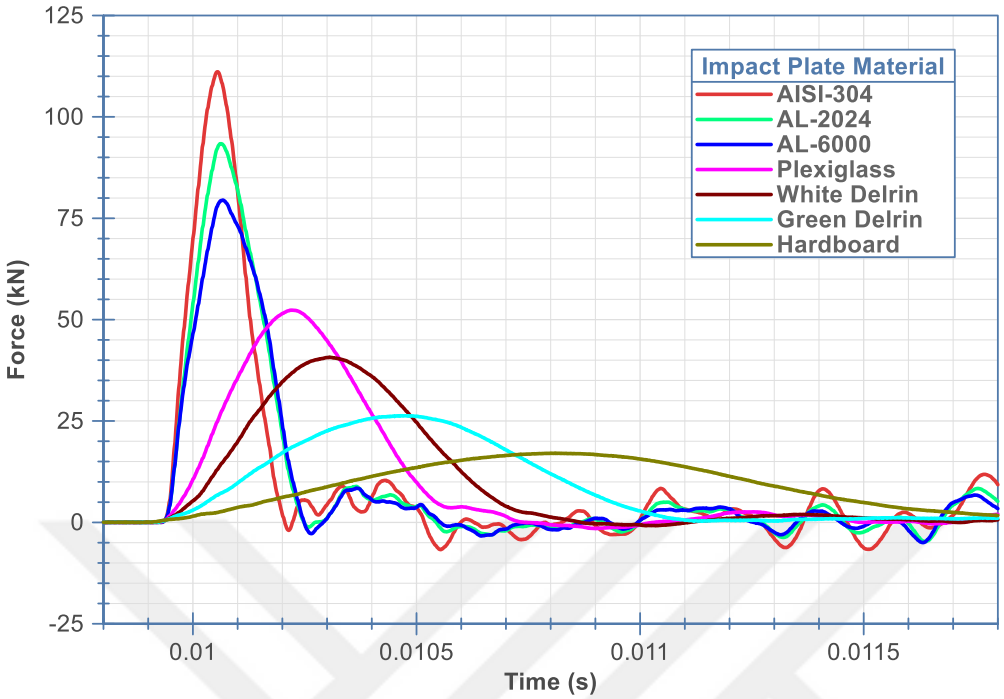


Figure 4.12. FMT result of mechanical filter, which is placed between hammer and impact plate

The impact plate hardens after the first test. We can observe this effect on the aluminum material in Figure 4.13. The force transmission increases significantly in successive tests. This result shows that the impact plate cannot produce the same effect in successive tests without changing it. A new plate is needed for each test in order to see the same effect on the results. The use of large amounts of plates is costly and also time-consuming to assemble in every test. It is more advantageous to use a paper type mechanical filter on a steel impact plate. In addition, mechanical filters must be replaced with a new one at every test. It can be easily changed in each test; also, it is cost-effective and easy to supply.

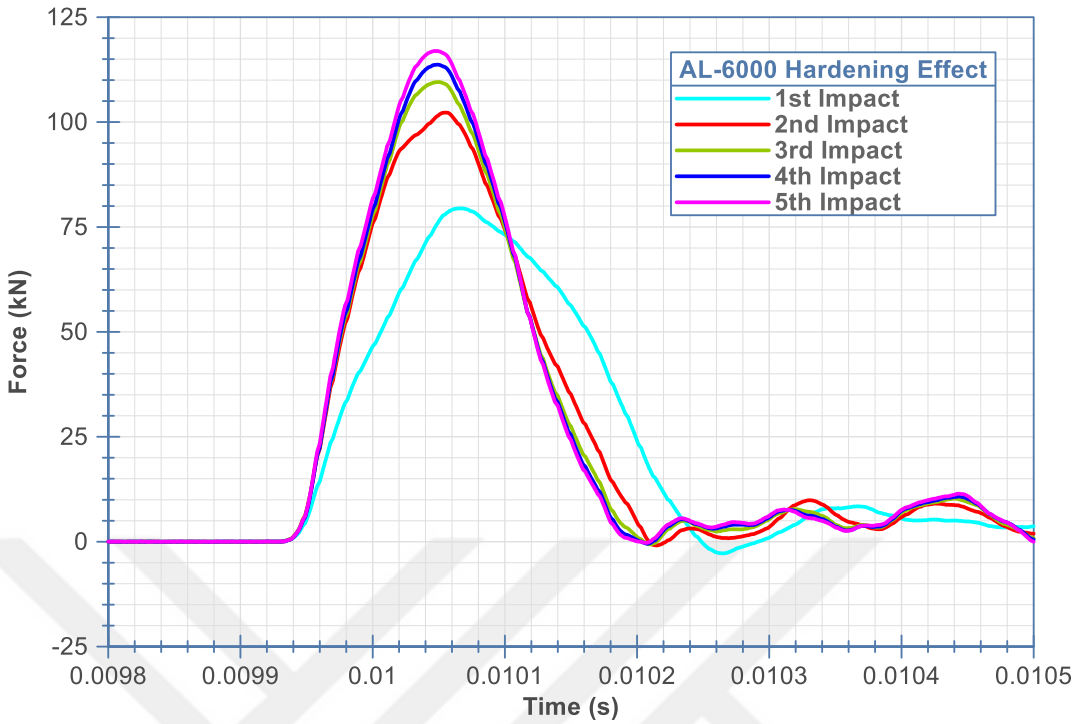


Figure 4.13. FMT result of aluminum 6061 material hardening effect in successive impacts

#### 4.1.2.4 Hammer Tip Radius

Force measurement tests were carried out with four different hammer tips in Figure 4.14 in order to investigate the effect of hammer tip radius on impact force profile. Some studies report that the hammer tip radius affects the high-frequency region of the SRS profile [8], [26]. However, it was observed that the radius of 80, 50, 40, and 35 mm did not affect the force half-sine, according to the results obtained in Figure 4.15. It is also seen that there are minimal differences between the results since the hammer angle could not be adjusted precisely.

Consequently, the hammers tested with different tip radius do not change the impact contact surface. It is understood that the radius values should be much smaller to be effective.

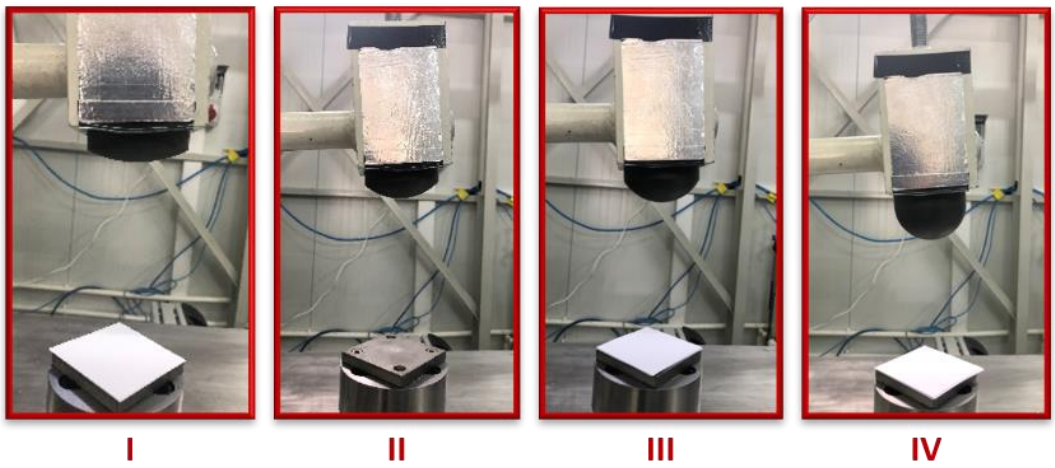


Figure 4.14. Hammer tip with four different radius (I: 80 mm, II: 50 mm, III: 40 mm, IV: 35 mm)

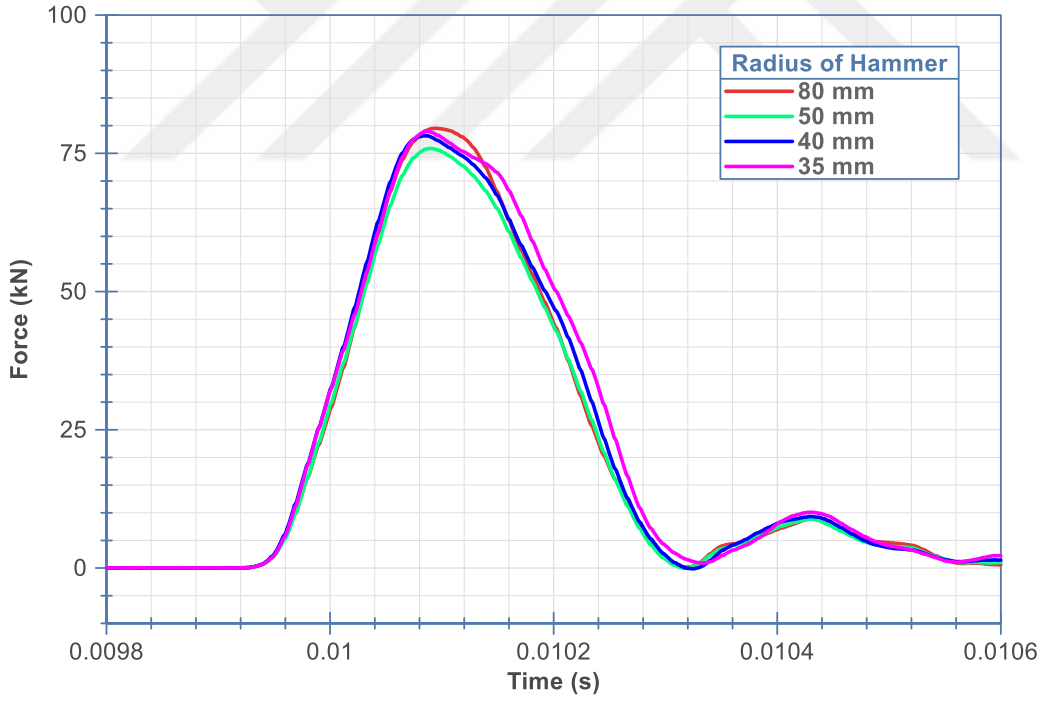


Figure 4.15. FMT result of hammer tip radius

## 4.2 Pyroshock Tests

### 4.2.1 Hardware and Setup

This section provides information about the hardware and software used in the pyroshock tests.

#### 4.2.1.1 Impact Method

The common pyroshock excitation methods are explosives and mechanical impact. Explosive methods are used when acceleration levels of 6000 g and above are needed. Mechanical impact methods can be categorized as pneumatic gun, pendulum hammer, drop towers, Hopkinson / Kolsky bars. In the test facility, there are pendulum and pneumatic type systems. The features of these systems are defined in Section 4.2.1.1.1 and 0, respectively.

##### 4.2.1.1.1 Impact by Pendulum Type Hammer

Shock tests in the infrastructure started with the pendulum type system shown in Figure 4.16. In this system, impact occurs simply using the gravity effect. The pendulum has a length of two meters. The effect of many parameters has been studied in this system. One of the system's advantages is that parameters can be manipulated more easily compared to the pneumatic system. In addition, it has a low operational cost. However, this system's main disadvantage is that a speed above 6 m/s cannot be obtained. Also, it is not possible to impact every point of the resonant plate.

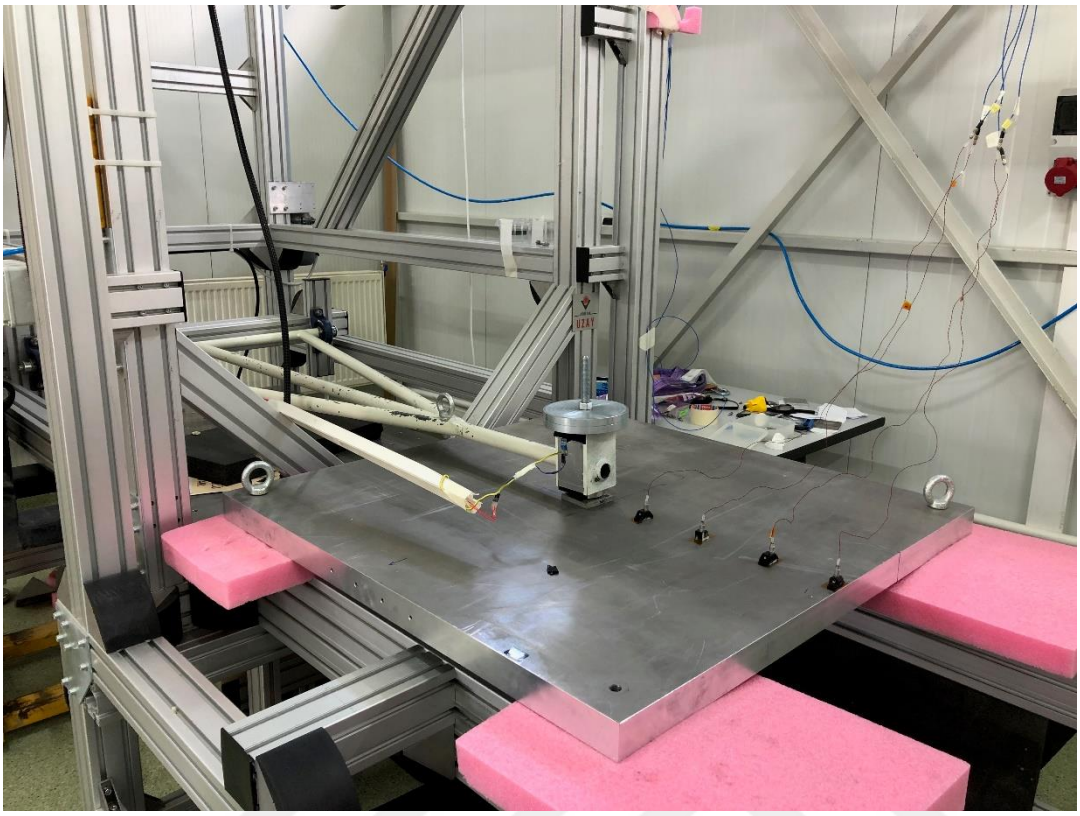

Figure 4.16. Pendulum type pyroshock test system

In the pendulum system, the speed can already be calculated theoretically, given in Table 4.2. However, there was a need for a speed measurement system. The aim is to verify the speed measurement setup in the pendulum system and prepare for reliable speed measurements in the pneumatic system. Speed measurement configuration is shown in Figure 4.17.

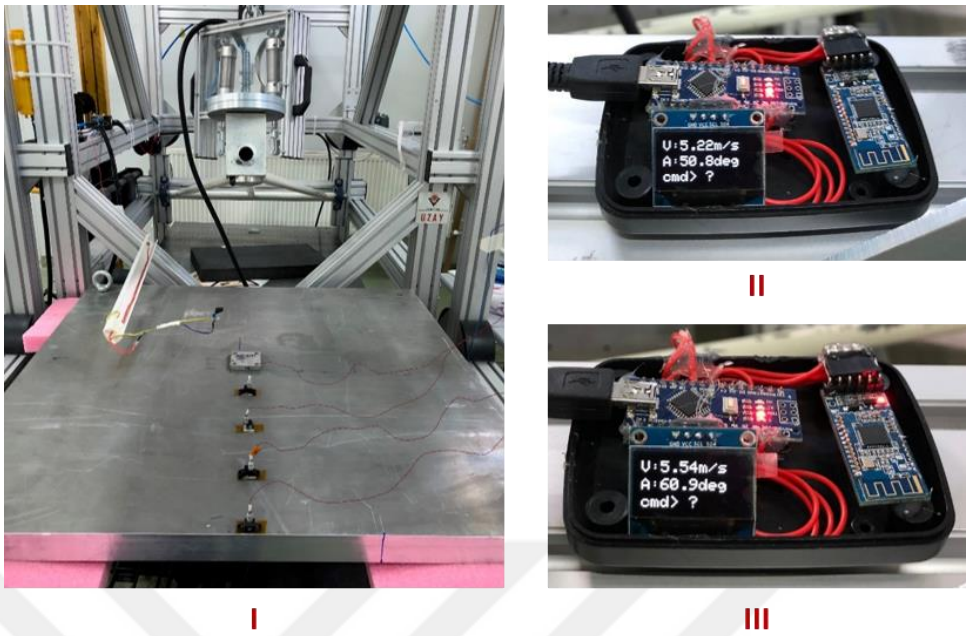


Figure 4.17. I: Hammer speed measurement configuration, II: Speed at 50.8°, III: Speed at 60.9°

Table 4.2 The theoretical speed values at various pendulum angles

| Angle | Speed |
|---|---|
| 5° | 1.74 m/s |
| 10° | 2.34 m/s |
| 20° | 3.44 m/s |
| 30° | 4.16 m/s |
| 45° | 4.94 m/s |
| 60° | 5.47 m/s |
| 75° | 5.77 m/s |
| 85° | 5.86 m/s |

#### 4.2.1.1.2 Impact by Pneumatic Gun

The hammer in the barrel reaches the desired kinetic energy with compressed air in the pneumatic system. The compressed air valve can be opened for a certain period of time (50 – 300 ms). It has been observed that more than one impact occurs when it is opened for longer periods. This means that the device under test is exposed to multiple shocks, and it is undesirable. The pneumatic test system is shown in Figure 4.18 and Figure 4.19, and the firing system units are illustrated in Figure 4.20.

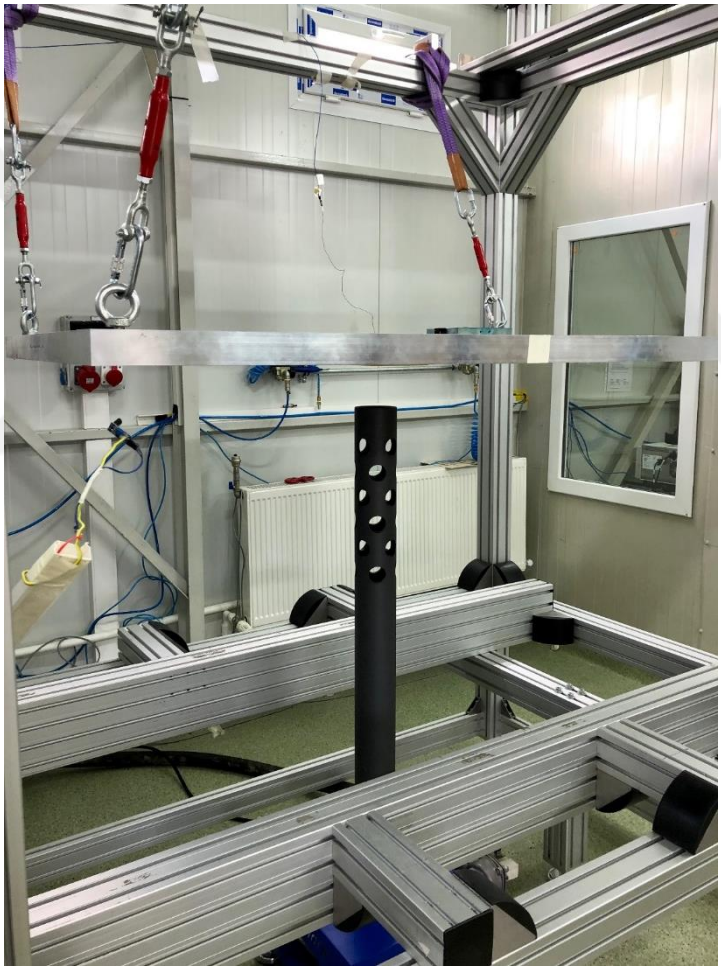

Figure 4.18. Pneumatic type pyroshock test system in a string hanging configuration

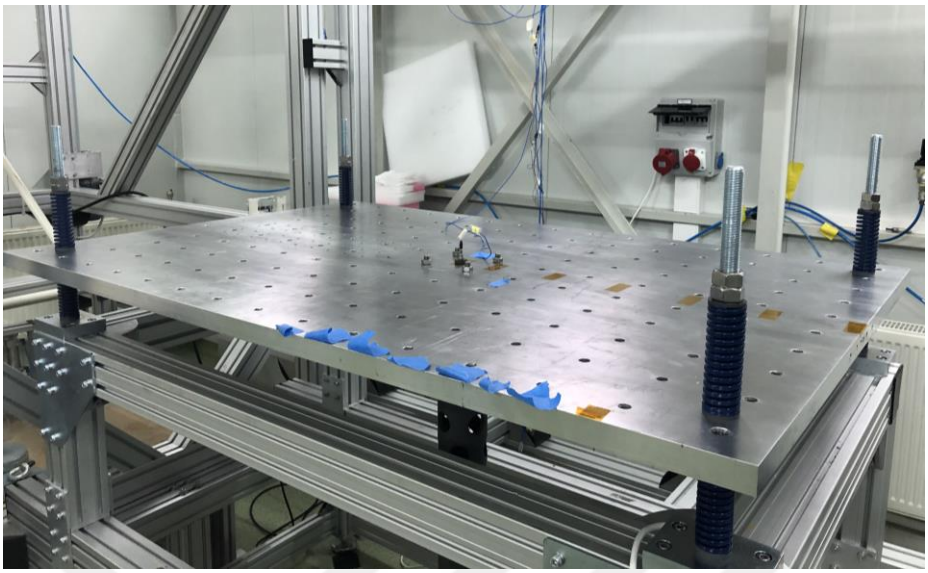

Figure 4.19. Pneumatic type pyroshock test system in a spring fixed configuration

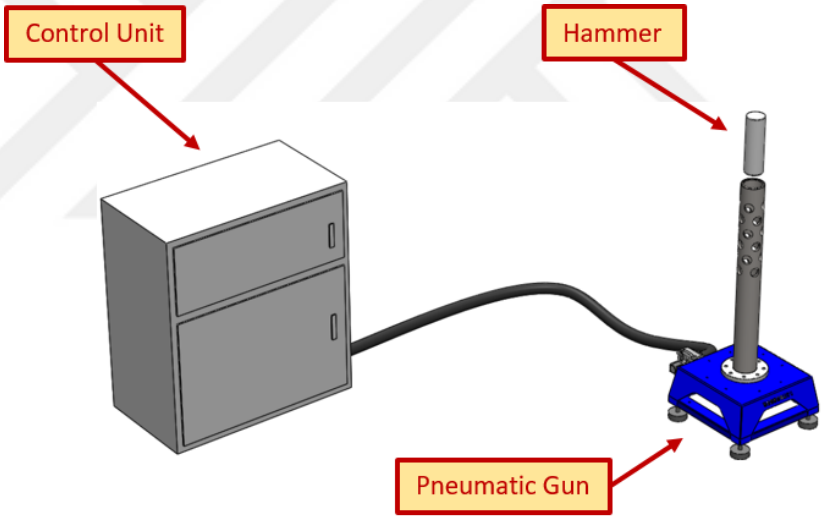


Figure 4.20. Pneumatic type pyroshock test system components

The main advantage of this system is that the impact speed can be easily controlled by pressure. The gun can be easily positioned according to the desired impact point. However, the system's complexity is a disadvantage in terms of the life of its components and the possibility of failure. The system also has to be fed with compressed air continuously. The speed values obtained from the system are summarized in Table 4.3. It can be achieved up to 15 $m/s$.

Table 4.3 The measured speed values in the pneumatic system

| Hammer Mass (kg) | Pressure (bar) | Valve Release Duration (ms) | Hammer Speed (m/s) |
|---|---|---|---|
| 7 | 0.46 | 300 | 3.1 |
| 7 | 0.88 | 300 | 5.8 |
| 7 | 1.6 | 150 | 8.8 |
| 7 | 2.8 | 50 | 12 |
| 7 | 4.3 | 100 | 15 |
| 15 | 0.7 | 300 | 3 |
| 15 | 1.7 | 300 | 6.2 |
| 15 | 3 | 300 | 8.8 |
| 15 | 4.5 | 100 | 10.9 |
| 15 | 4.5 | 150 | 10.6 |
| 15 | 4.5 | 50 | 10 |

#### 4.2.1.2 Data Acquisition and Measurement Approach

It is necessary to collect data at a high sampling rate in pyrotechnic measurements since the shock pulse is damped in about 20 ms. For this type of measurement, requirements related to data acquisition and instrumentation are defined in various standards. In this study, the measurement approach suggested by ECSS was followed [1, Ch. 13.4].

The data were collected by using NI PXIe-1073 chassis with NI PXIe-4480 module [27], [28]. With this system shown in Figure 4.21, data can be collected from a maximum of 6 accelerometers at the same time. Measurements were carried out in half-second periods with a sampling rate of 200k.

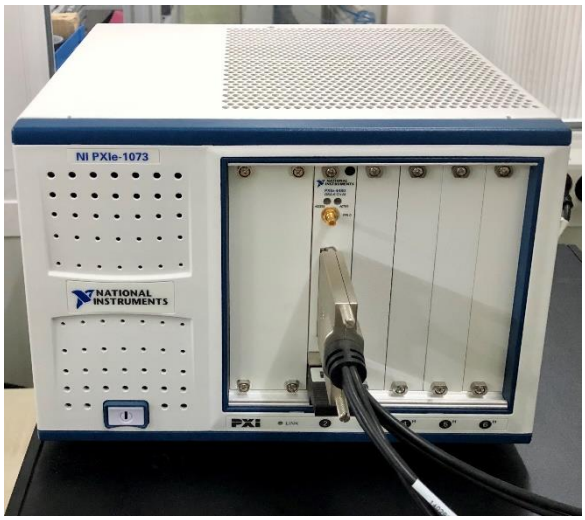


Figure 4.21. Data acquisition system

Kistler 8743A10 model shock accelerometers were used which is shown in Figure 4.22 [29]. Its measurement range is ±10000 g.

Figure 4.22. Kistler 8743A10 model shock accelerometer

Labview SRS program was utilized to control the data acquisition system [30]. Here, the SRS calculating function is given in Figure 4.23, and the inputs and outputs are specified.

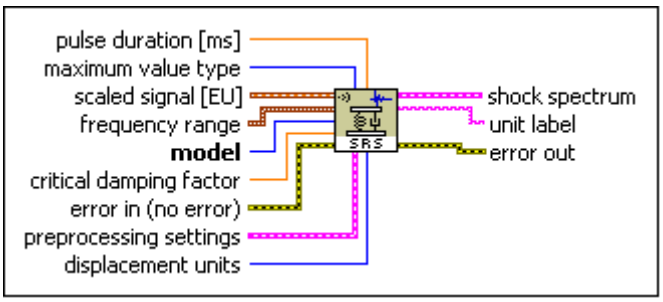


Figure 4.23. Labview shock response spectrum calculator

#### 4.2.1.3 Knee point identification method for comparing SRS profiles

When defining the SRS profile, the starting point, knee point, and endpoint are commonly defined. These three points are expressed when specifying the shock test level. Therefore, they are generally followed while observing parameter changes. A method was developed to characterize the SRS profiles while the studies were conducted. The graphical user interface of the program prepared for this thesis study is shown in Figure 4.24. The blue-colored shock profile is given as an input to the program, and the green-colored profile is taken as the output of the program. In addition, the estimated profile information is also specified.

The low-frequency linear region and the high-frequency flat region were examined separately, and the intersection point of these two regions was determined as the knee point. It is the intersection of the red line and the white line in Figure 4.25.

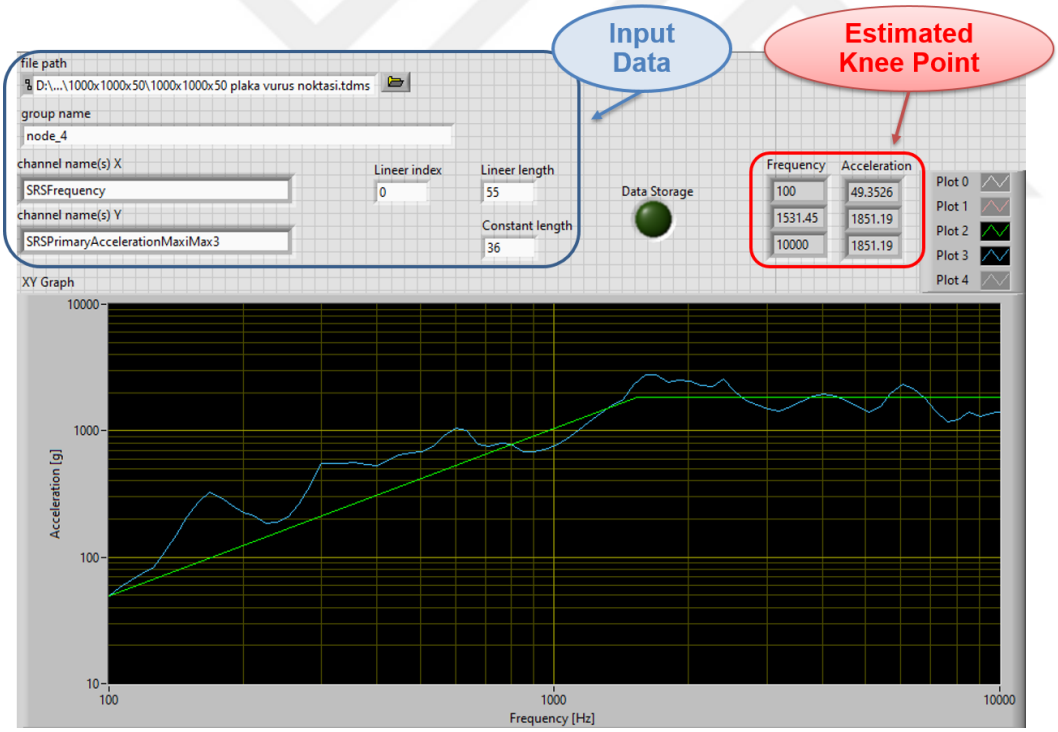


Figure 4.24. Knee point identification program graphical user interface

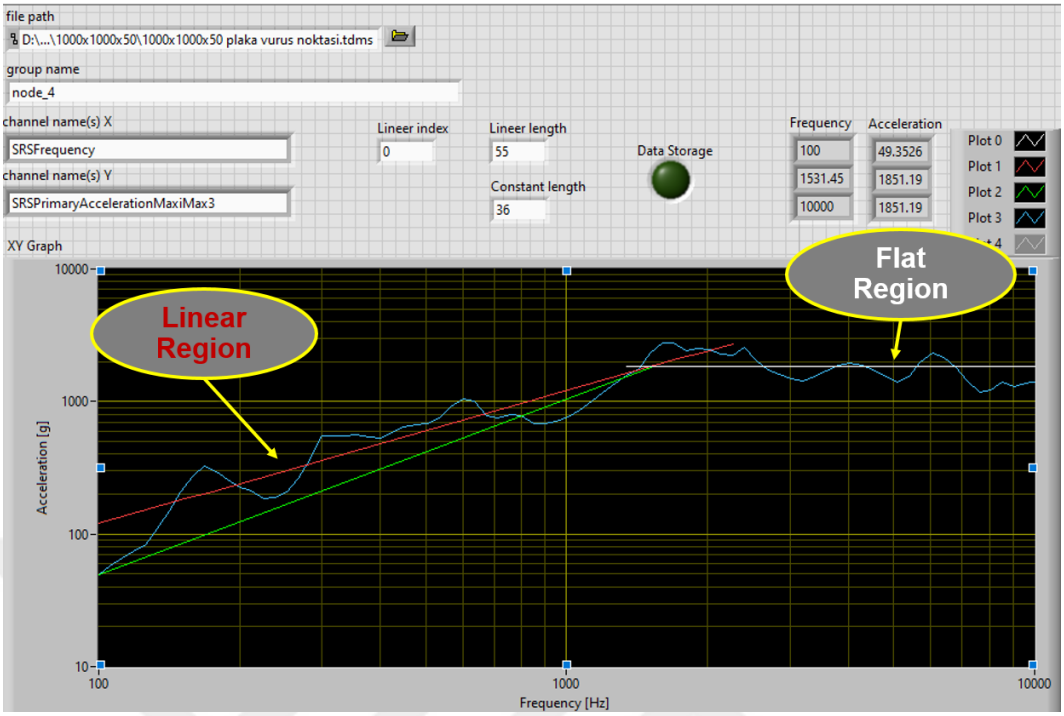


Figure 4.25. Knee point identification with the linear and flat region

### 4.2.2 Test System Parameters

The effect of parameters is examined in Chapter 3 by finite element analysis. However, the effect of the parameters was also observed in the test system in order to verify the analysis model and the obtained results. A limited study has been done here because there are no plates of all sizes or hammers in every mass in the facility, or the speed provided by the test system cannot exceed a certain limit. The parameters tested here are given in Table 4.4.

Table 4.4 Test system parameters examined in pyroshock test facility

| Parameters | |
|---|---|
| Plate Thickness | Hammer Speed |
| Hammer Mass | Impact Location |
| Measurement Location | Mechanical Filter |

#### 4.2.2.1 Hammer Speed

We have learned that the amplitude of the half-sine increases with increasing the hammer speed. In a pneumatic system, impact speed can be adjusted by changing the pressure. The effect of pressure change on the shock profile is shown in Figure 4.26, Figure 4.27, and Figure 4.28.

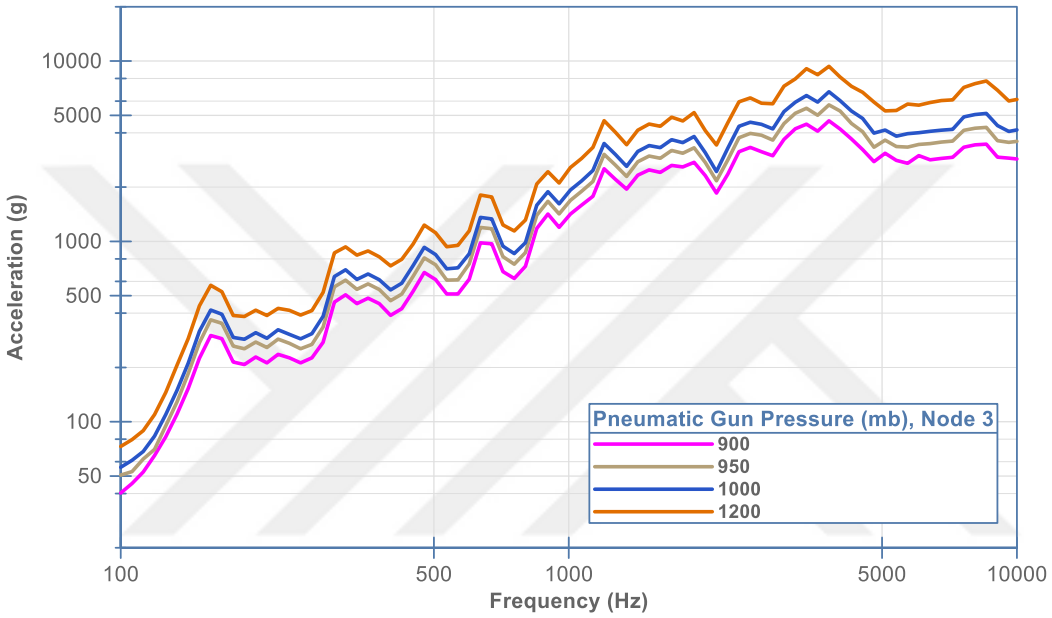


Figure 4.26. Pyroshock test results of impact speed using 1500x1000x30 $mm^3$ plate at node 3

The hammer speed is the most important parameter that increases the intensity of the shock at all frequencies. The change of this effect was observed similarly in the analysis results in Section 3.3.1. Additionally, speed effect studies on the SRS profile were presented by Jonsson and Morais et al. [8], [12]. They also achieved similar results.

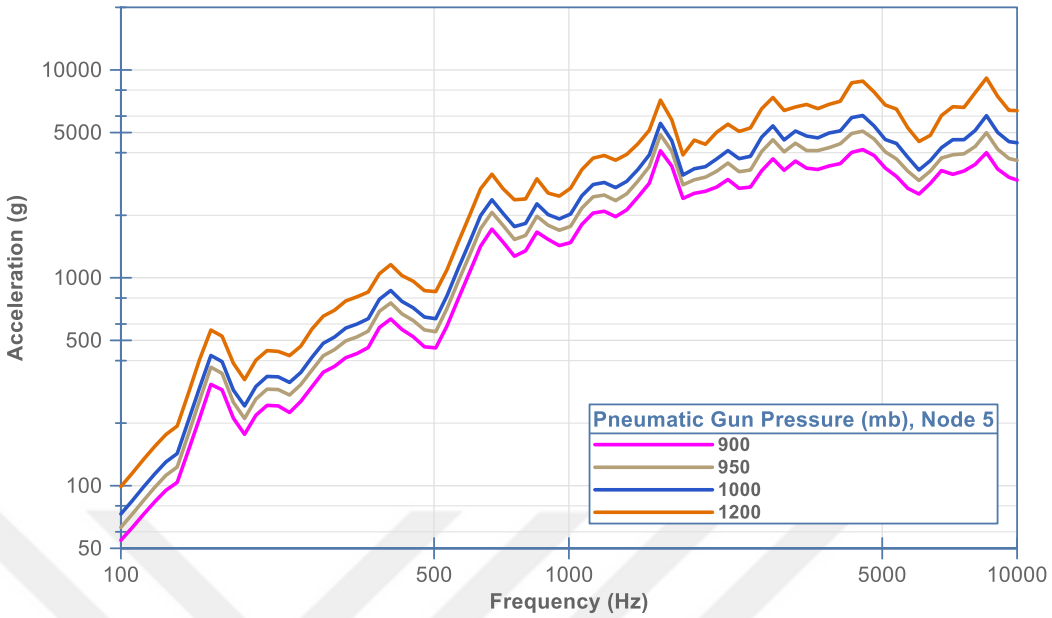


Figure 4.27. Pyroshock test results of impact speed using 1500x1000x30 $mm^3$ plate at node 5

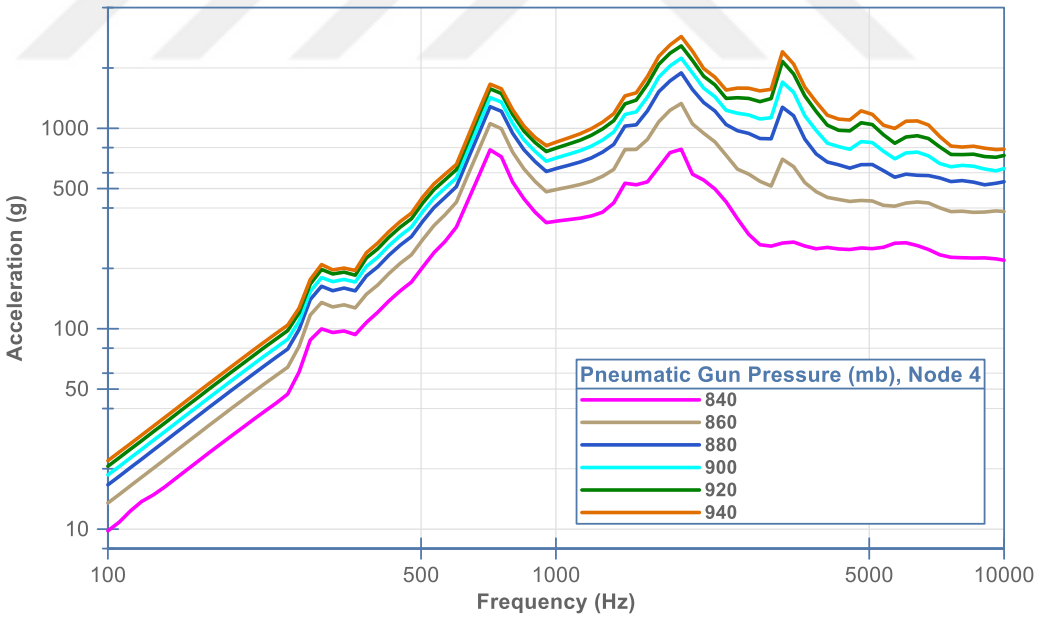


Figure 4.28. Pyroshock test results of impact speed using 1000x1000x50 $mm^3$ plate at node 4

#### 4.2.2.2 Hammer Mass

It has been experienced from both FEA and force sensor tests that hammer mass affects the duration of half a sine. In the pendulum system, the hammer's empty mass is 11 kg, and disks of 2 kg weights can be added to this mass. In this way, a maximum mass of 27 kg can be reached. The results obtained in this system are shown in Figure 4.29.

The hammer mass change effect was observed similarly in the analysis results in Section 3.2. With the applied analysis modeling approach, the impact of hammer masses that are not in the infrastructure but needed can be predicted.

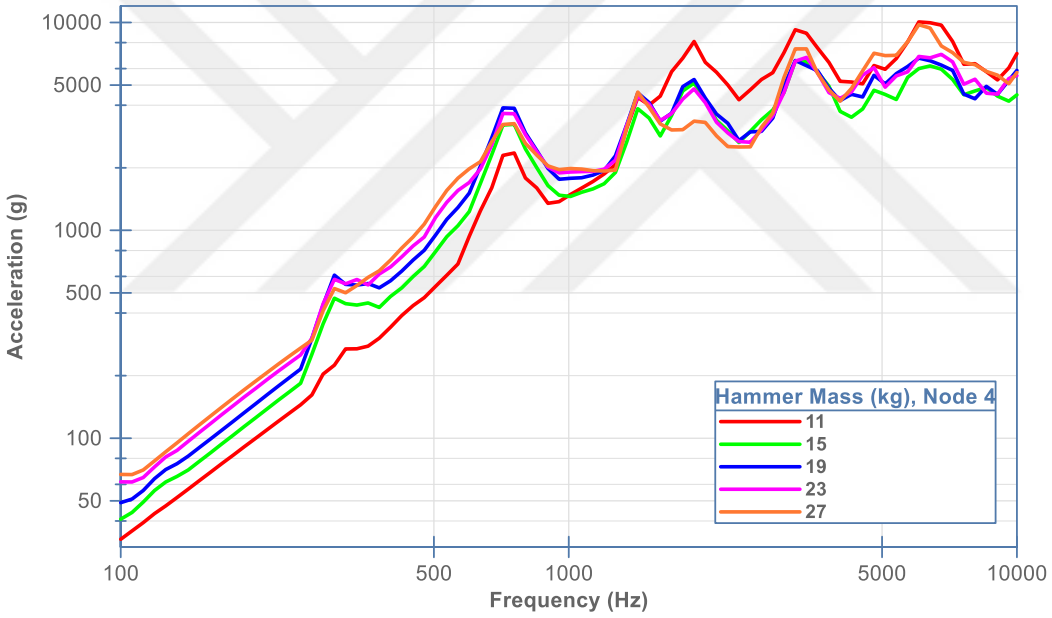


Figure 4.29. Pyroshock test results of hammer mass using 1000x1000x50 $mm^3$ plate at node 4

There are 7 kg and 15 kg hammers in a pneumatic system, and the effect of the mass change on the shock profile is shown in Figure 4.30 and Figure 4.31.

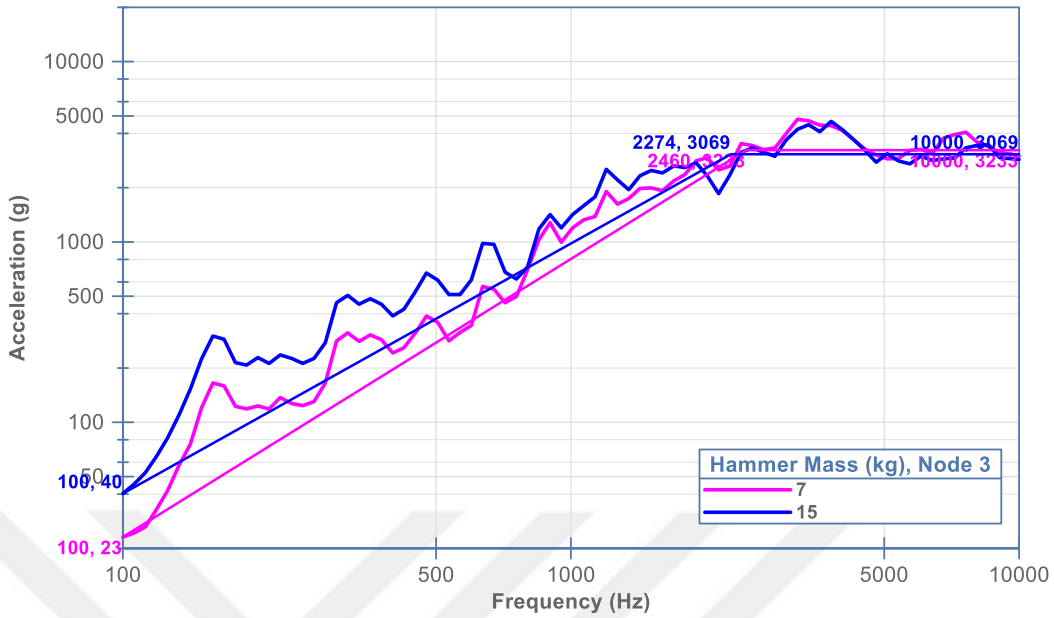


Figure 4.30. Pyroshock test results of hammer mass using 1500x1000x30 $mm^3$ plate at node 3

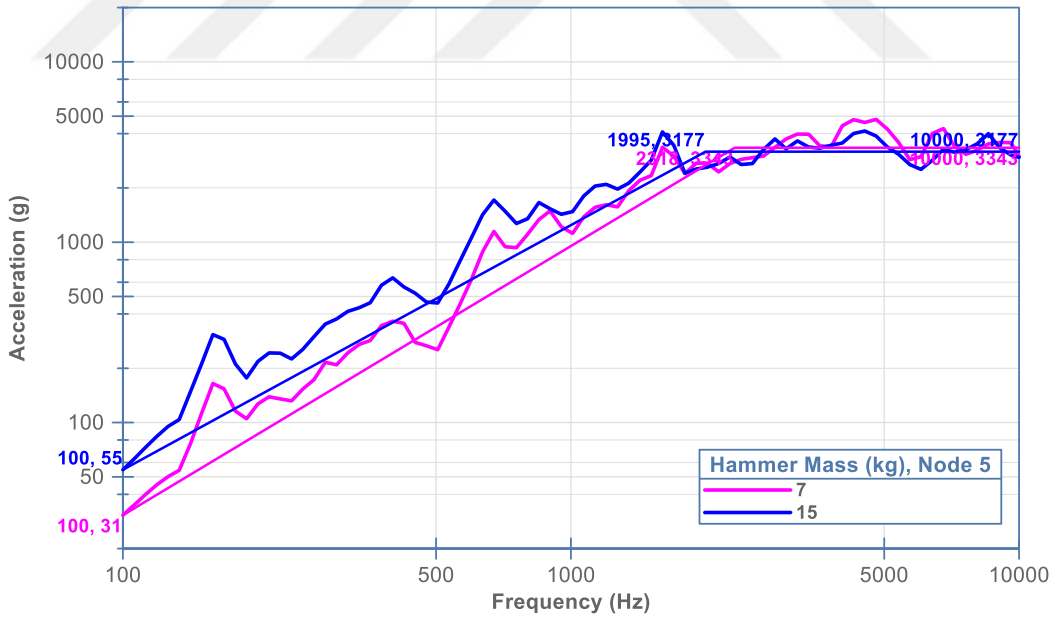


Figure 4.31. Pyroshock test results of hammer mass using 1500x1000x30 $mm^3$ plate at node 5

#### 4.2.2.3 Mechanical Filter

The mechanical filter between the impact plate and the hammer directly affects the half-sine. This is observed in force measurement tests in Figure 4.10 and Figure 4.12. The effect of mechanical filter on SRS profiles was also observed in tests. However, in the test facility, the sheet of paper is used as a mechanical filter in order to change the half-sine more precisely. Slight changes could be made to the SRS profile by changing the number of papers. The usage of the sheet paper simplifies the process of test profile adjustment. A4 size 80 $g/m^2$ typical office papers were used in the studies. The results are presented in Figure 4.32, Figure 4.33, and Figure 4.34. Pyroshock test results of mechanical filter of impact using 1000x1000x50 $mm^3$ plate with 15 kg hammer at node 4.

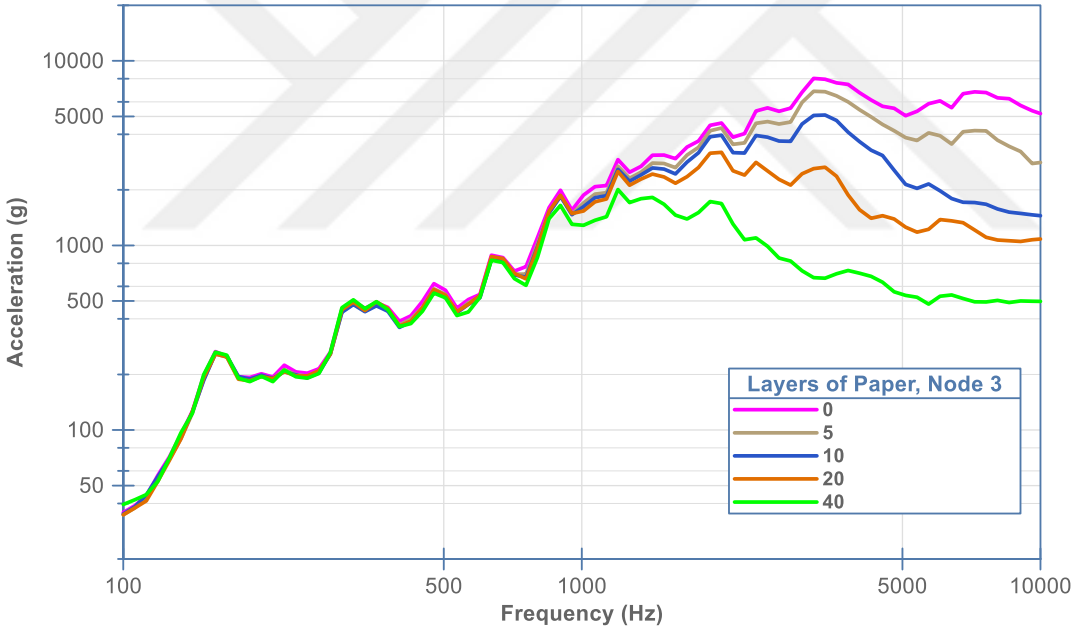


Figure 4.32. Pyroshock test results of mechanical filter of impact using 1500x1000x30 $mm^3$ plate with 7 kg hammer at node 3

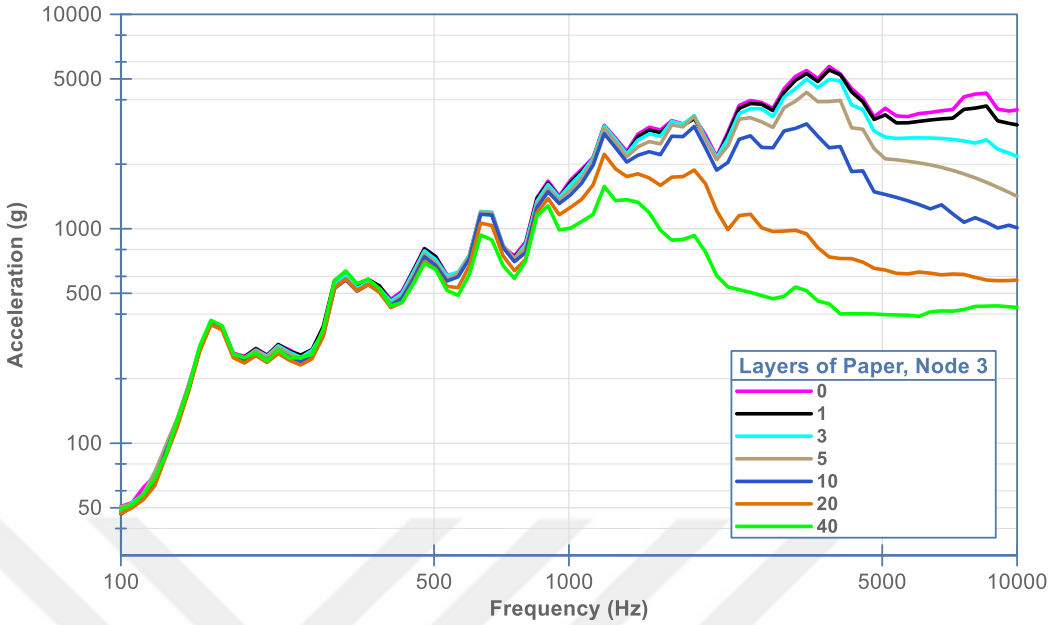


Figure 4.33. Pyroshock test results of mechanical filter of impact using 1500x1000x30 $mm^3$ plate with 15 kg hammer at node 3

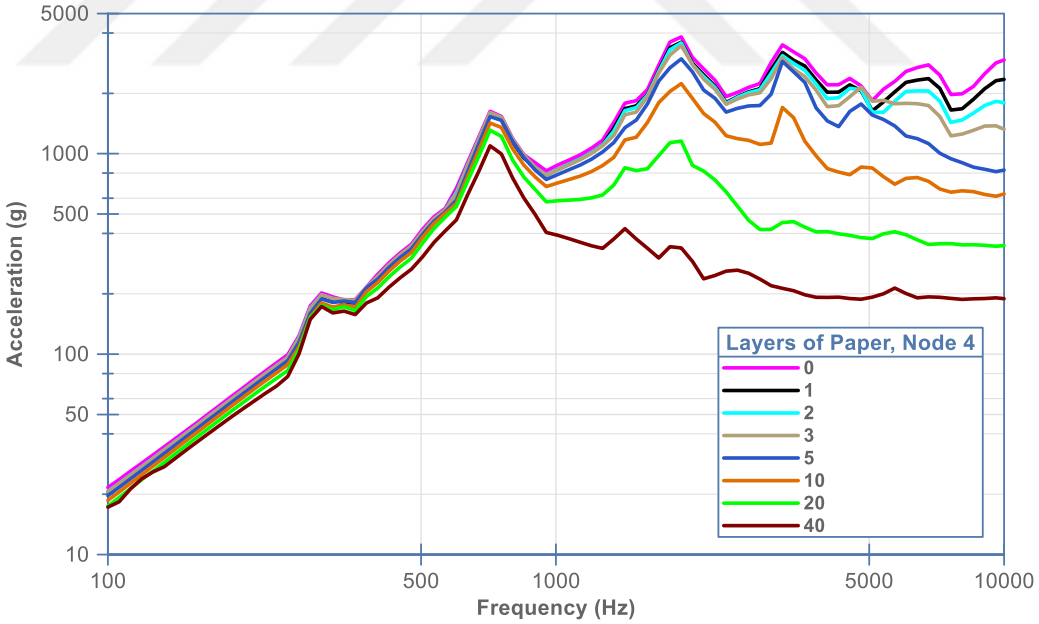


Figure 4.34. Pyroshock test results of mechanical filter of impact using 1000x1000x50 $mm^3$ plate with 15 kg hammer at node 4

#### 4.2.2.4 Impact and Measurement Location

The resonant plate is commonly excited at two points in the test infrastructure. These points are the Node 6R and Node 1 location. The results when testing at these locations are shown in Figure 4.35, Figure 4.36, and Figure 4.37.

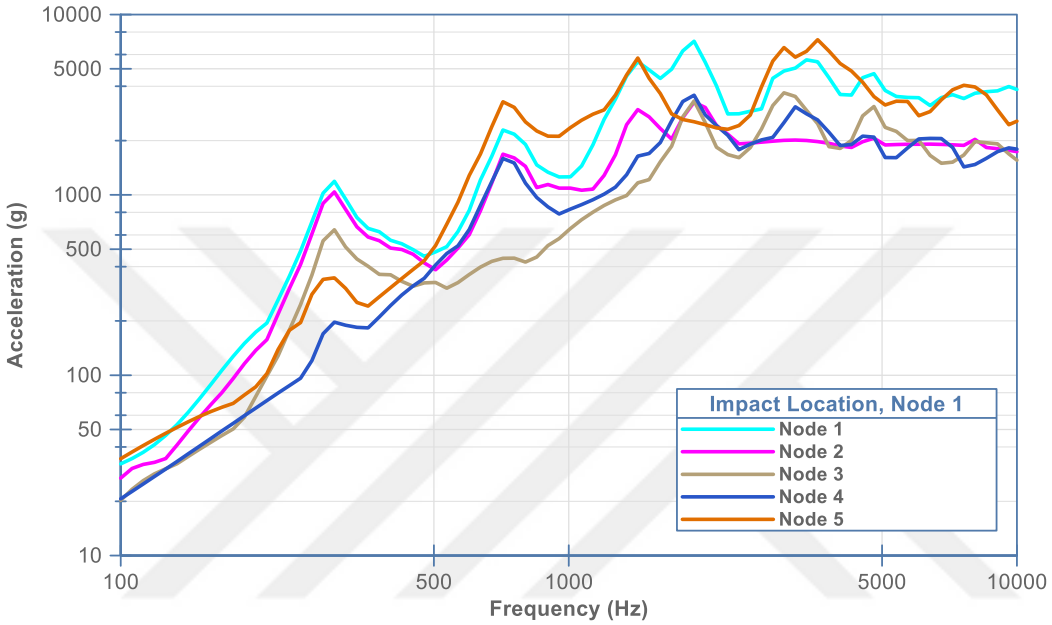


Figure 4.35. Pyroshock test result of impact location using 1000x1000x50 $mm^3$ plate at node 1

The impact was carried out from the Node 1 location in Figure 4.35, and measurements were taken from five points. In the first mode at 300 Hz, the amplitude decreases from 1190 g to 197 g as the measurement point moves away from the impact location. In the second mode at 712 Hz, the amplitude varies from 445 g to 3287 g. The amplitude is the lowest value in the Node 3 zone, while the highest value in the Node 5 zone. The edge effect appears at Node 5 since it is on the edge of the plate. In the third mode at 1902 Hz, the amplitude varies from 2546 g to 7110 g. Points closer to the impact location appear to be more affected in this mode. In summary, the FE result indicated in Figure 3.15 in the same configuration was also observed in the test results.

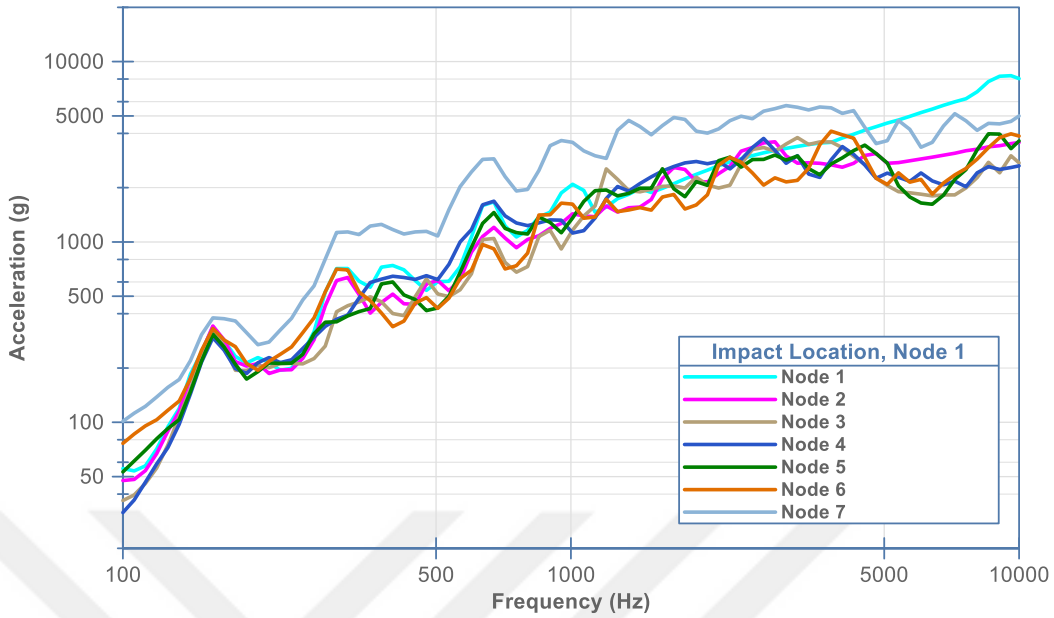


Figure 4.36. Pyroshock test result of impact location using 1500x1000x30 $mm^3$ plate at node 1

The impact was carried out from Node 1, and measurements were taken from seven points in Figure 4.36. In the first mode at 159 Hz, the amplitude is the same in all locations. In the second mode at 300 Hz, there is amplification in the middle and edge zone of the plate, but there is no amplification in Node 3, Node 4, and Node 5 locations, which is also suitable for testing. Additionally, the Node 7 location's acceleration levels are higher than other points since it is located on edge. It shows that testing should not be done at the edge point. Because there is a huge difference between it and its neighbor point Node 6. Since the test item interface can not be too small, a certain part of it is exposed to an over-level test. A similar result is also observed in FE analysis in Figure 3.18.

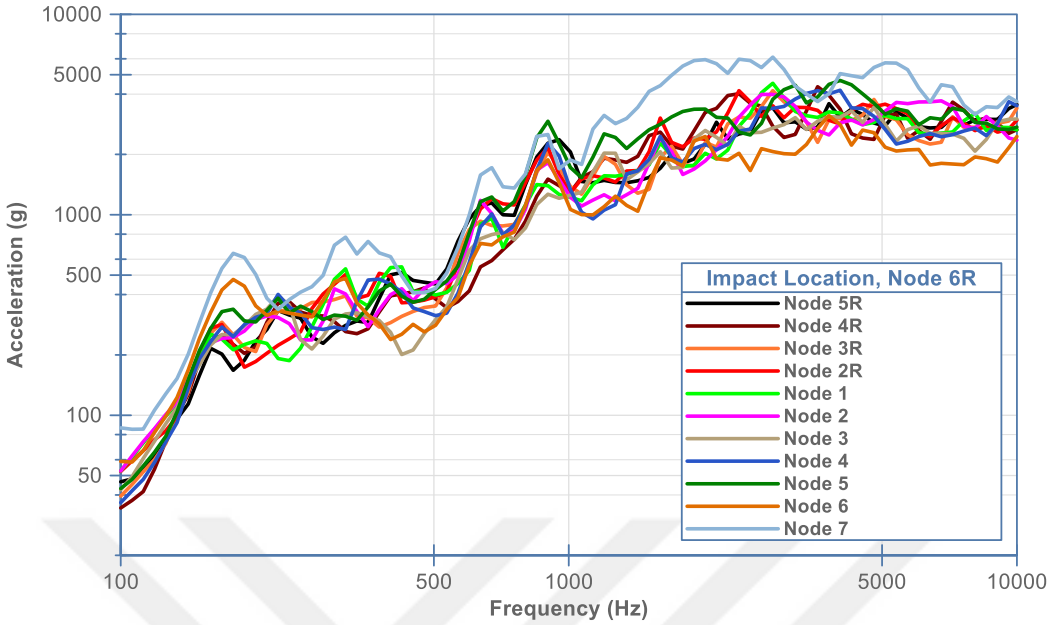


Figure 4.37. Pyroshock test result of impact location using 1500x1000x30 $mm^3$ plate at node 6R

The impact was carried out from Node 6r, and measurements were taken from eleven points in Figure 4.37. In the first mode at 178 Hz, there is high amplification on the opposite edge. The second and third mode are at 672 Hz and 900 Hz, respectively. Except for the edge point, the Node 4R to Node 2R area offers profiles suitable for testing. Because the modal amplification of the resonant plate at these positions are weaker. Thus, the test item is not exposed to unnecessarily high acceleration levels. A similar result was obtained by FE simulation at this point and indicated in Figure 3.19.

## 4.3 Pyrotechnic Valve Test

Pyrotechnic valves are used in chemical propulsion systems to control the flow one time. They are designed as closed or open in normal condition according to need. The valve is activated by the ignition current and goes into the opposite state of its original state. It creates massive shock during ignition, and components located close to these valves should consist of shock-resistant components.

Figure 4.38. Pyrotechnic valve

A sample pyro valve, which is shown in Figure 4.38, is tested to confirm that the firing can be done properly and measure the shock levels. The test configuration is given in Figure 4.39. The data was obtained from one accelerometer in the direction of in-plane (IP) and one accelerometer in the direction of out-of-plane (OOP) during the test.

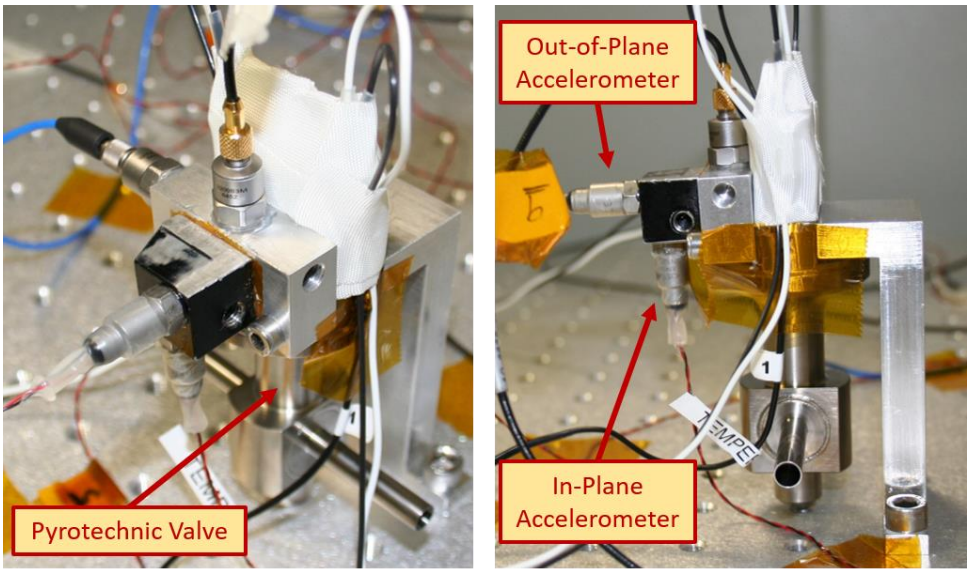


Figure 4.39. Test configuration of the pyrotechnic valve (I: Isometric view, II: Side view)

The shock time data of a sample test is shown in Figure 4.40 and Figure 4.41. The SRS graph corresponding to these time data is given in Figure 4.42.

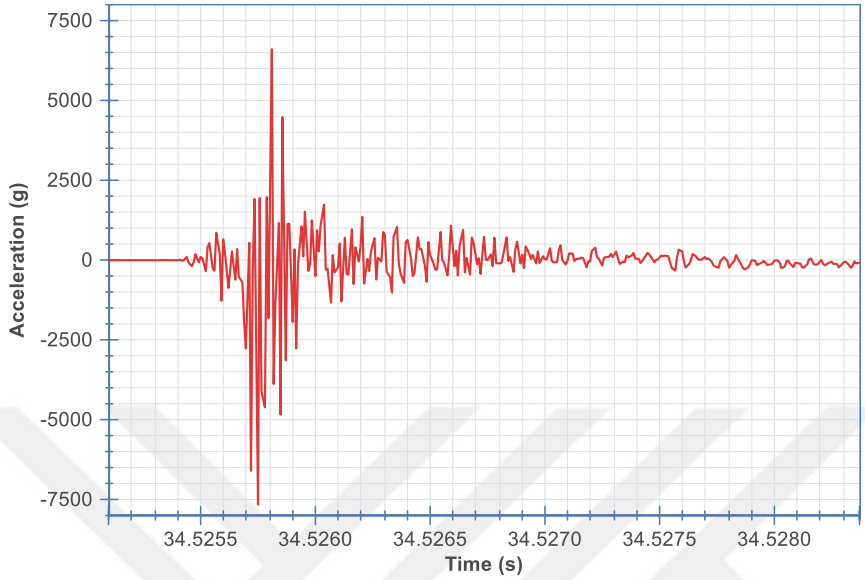


Figure 4.40. Pyrotechnic valve test OOP accelerometer time data

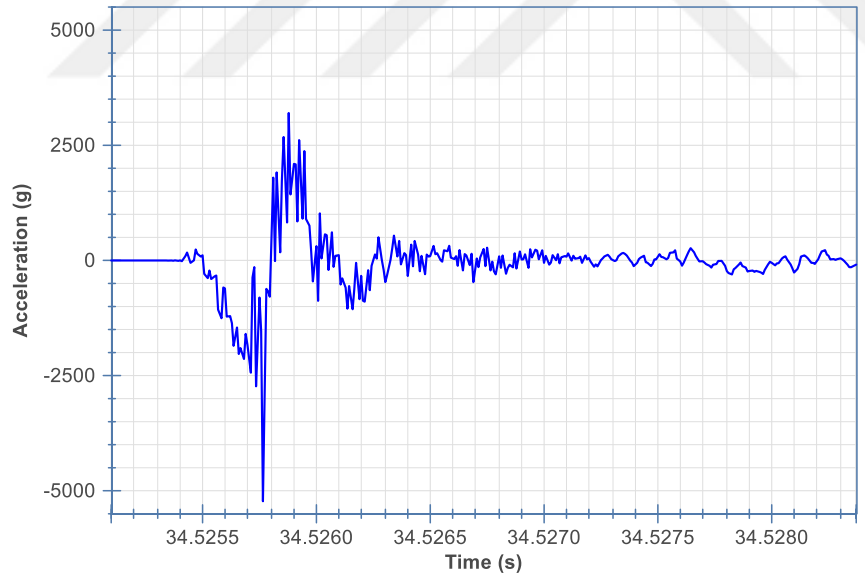


Figure 4.41. Pyrotechnic valve test IP accelerometer time data

The time data in Figure 4.40 and Figure 4.41 shows that the severe shock occurs within 0.28 ms at OOP and 0.5 ms at IP direction, and wave interaction and damping takes 1.6 ms.

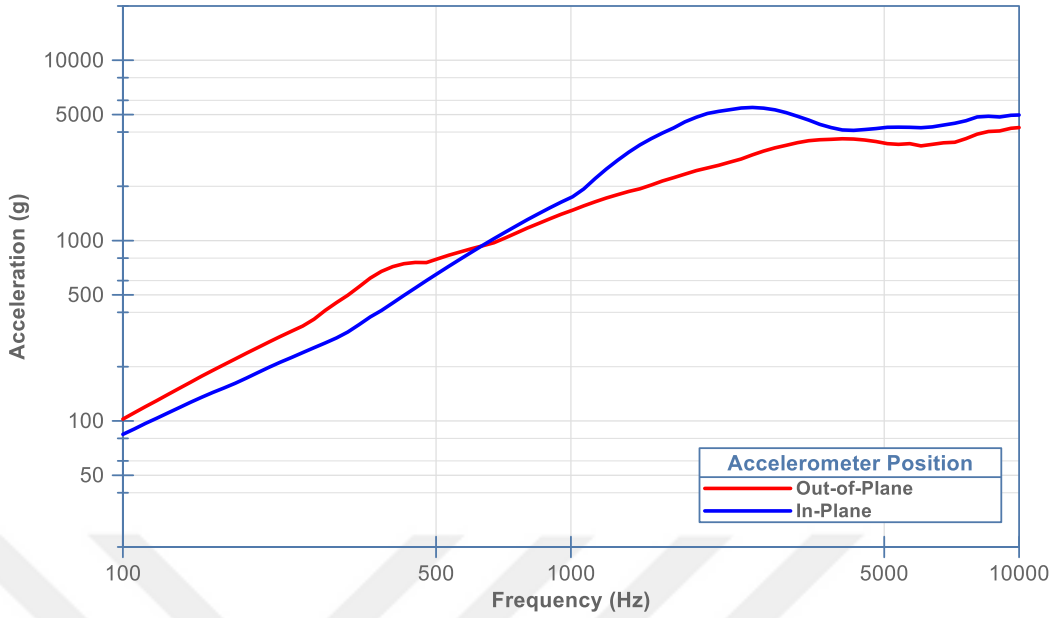


Figure 4.42. Pyrotechnic valve test SRS graph

The calculated SRS of these time data is shown in Figure 4.42. The most obvious difference from the shock simulated using the resonant plate is the absence of modal peaks in SRS data. In equipment qualification tests performed on the resonant plate, excessive loads are given at certain frequencies according to the modal characteristics of the plate. However, in reality, a smooth input load comes from the pyrotechnic equipment, as shown in Figure 4.42. Even more, equipment failure may occur if the resonant plate's modal load coincides with the modes in FRF of the equipment during the qualification test. As a result of this test, the shock level created by the sample shock source was measured. In the test facility, the pyroshock tests with resonant plate aim to qualify the equipment by creating similar profiles. Positioning analysis should be done on the plate, especially in order to avoid the excessive modal loads of the plate. Besides, it was understood that the shock sensitivity of the equipment which is located near the shock sources should be well evaluated. Equipment shock profiles vary according to their distance from the source in the space structures.

# CHAPTER 5

## COMPARISON OF NUMERICAL AND EXPERIMENTAL RESULTS

Analysis models and corresponding test configuration results have been compared under this chapter. The locations examined in the analysis predictions were determined on the resonant plate, and accelerometers were mounted in the out-of-plane direction. The SRS plots at these points were compared, and the results are indicated in the next sections according to the compared resonant plate sizes.

In the numerical models, the force profiles measured by the force sensor as shown in Figure 5.1 was applied as a concentrated force to the FEM model. The use and non-use of 10 layers of sheet paper as a mechanical filter were evaluated at each impact point.

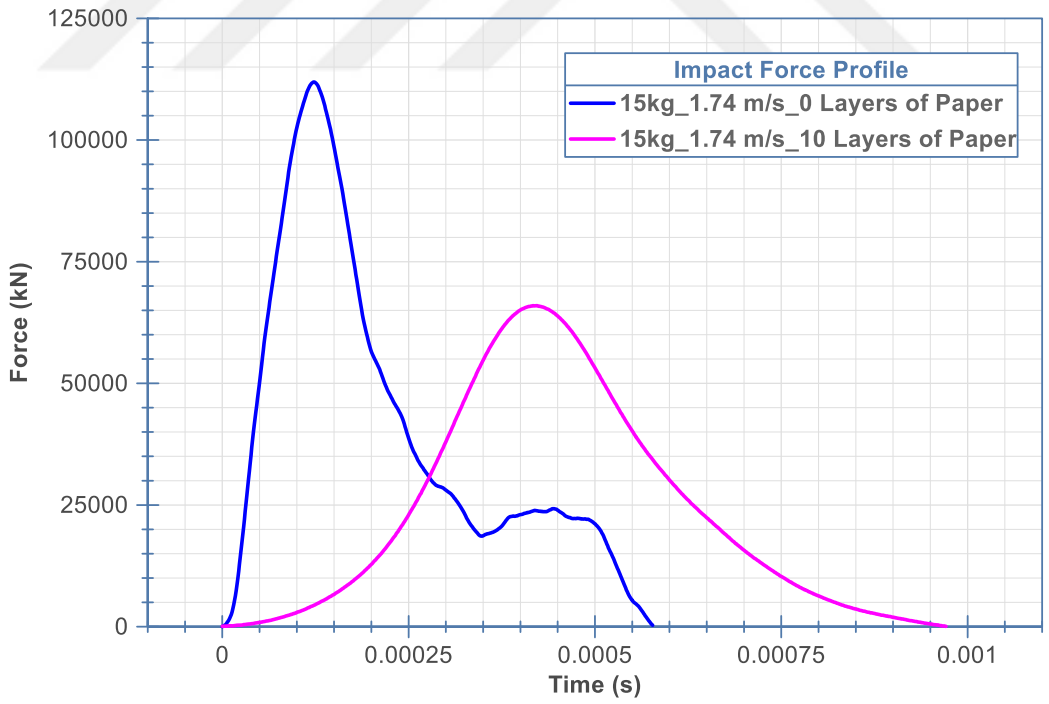


Figure 5.1. Force profiles of the hammer with a mass of 15 kg and a speed of 1.74 m/s according to the mechanical filter

## 5.1 Results with 1000x1000x50 $mm^3$ Resonant Plate

The test configuration is shown in Figure 5.2, and the FEA configuration is shown in Figure 3.2. The resonant plate was excited from Node 1 with a 15 kg hammer, which has a speed of 1.74 $m/s$.

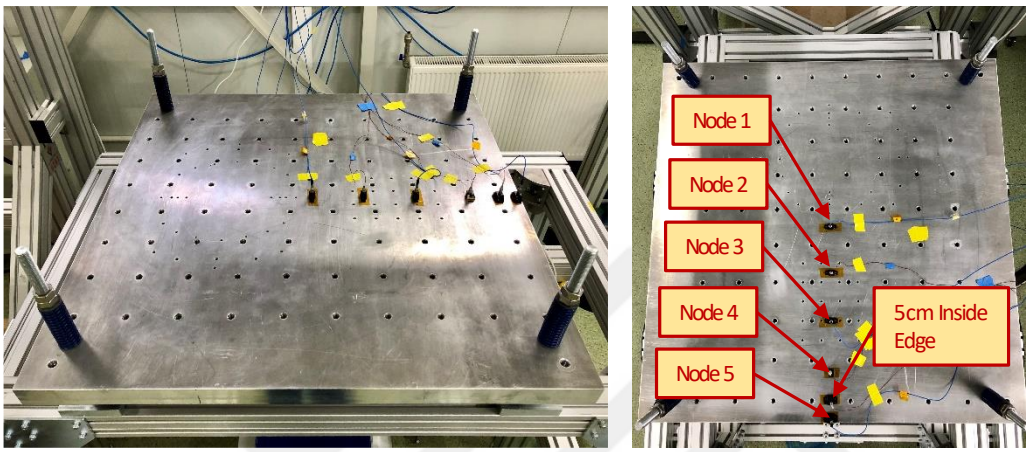


Figure 5.2. 1000x1000x50 $mm^3$ resonant plate pneumatic test system configuration (I: Side view, II: Front view)

### 5.1.1 Comparison Without Mechanical Filter

The results obtained in the absence of a mechanical filter are shown in Figure 5.3 to Figure 5.7.

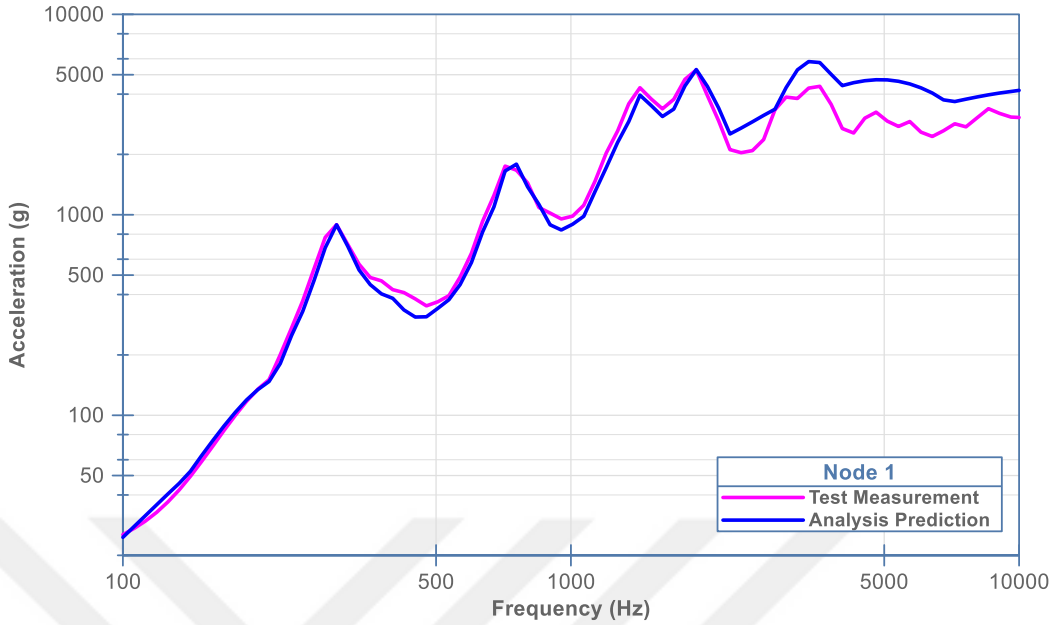


Figure 5.3. Comparison of the test and analysis results using 1000x1000x50 $mm^3$ plate excited from Node 1 without the mechanical filter at Node 1

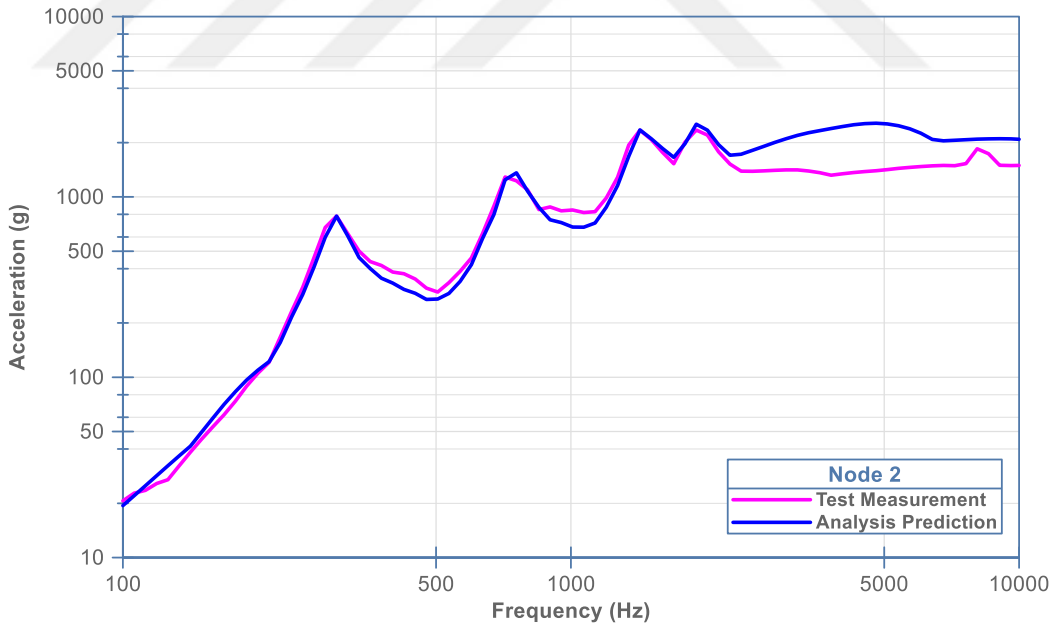


Figure 5.4. Comparison of the test and analysis results using 1000x1000x50 $mm^3$ plate excited from Node 1 without the mechanical filter at Node 2

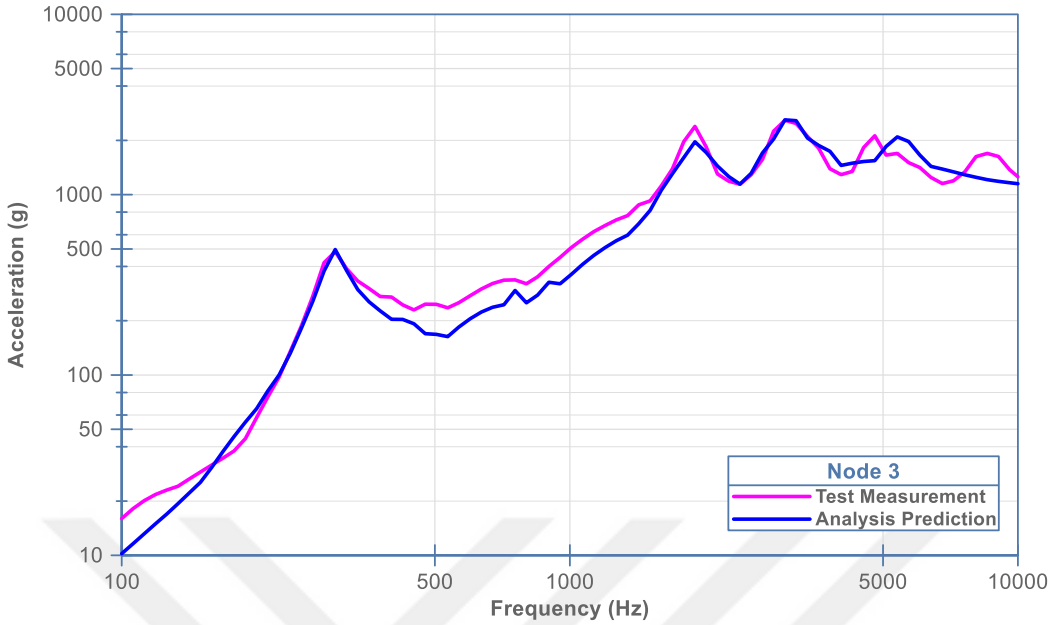


Figure 5.5. Comparison of the test and analysis results using 1000x1000x50 $mm^3$ plate excited from Node 1 without the mechanical filter at Node 3

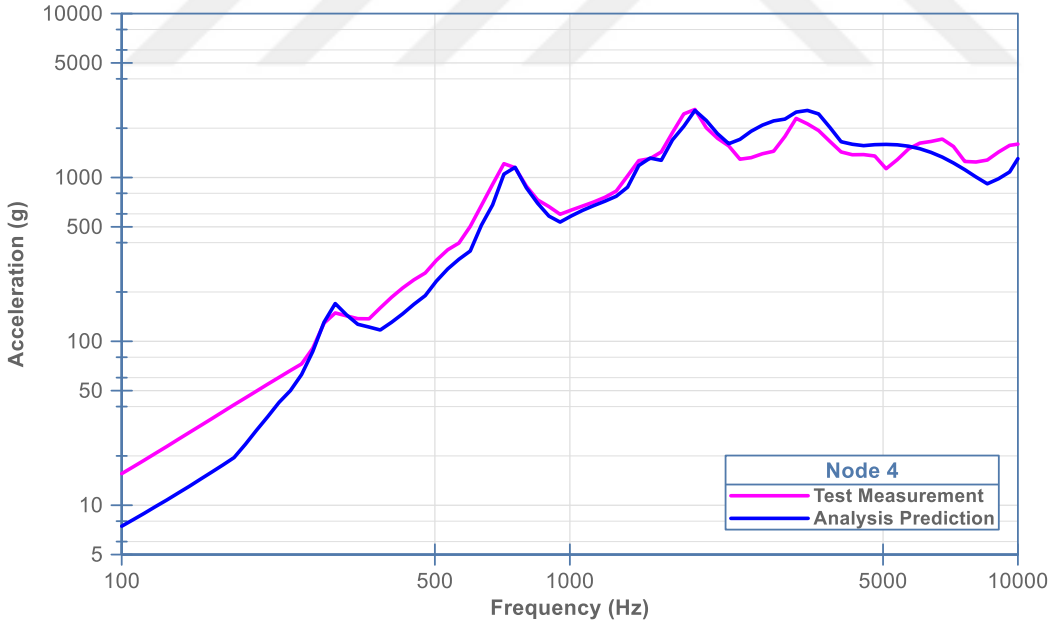


Figure 5.6. Comparison of the test and analysis results using 1000x1000x50 $mm^3$ plate excited from Node 1 without the mechanical filter at Node 4

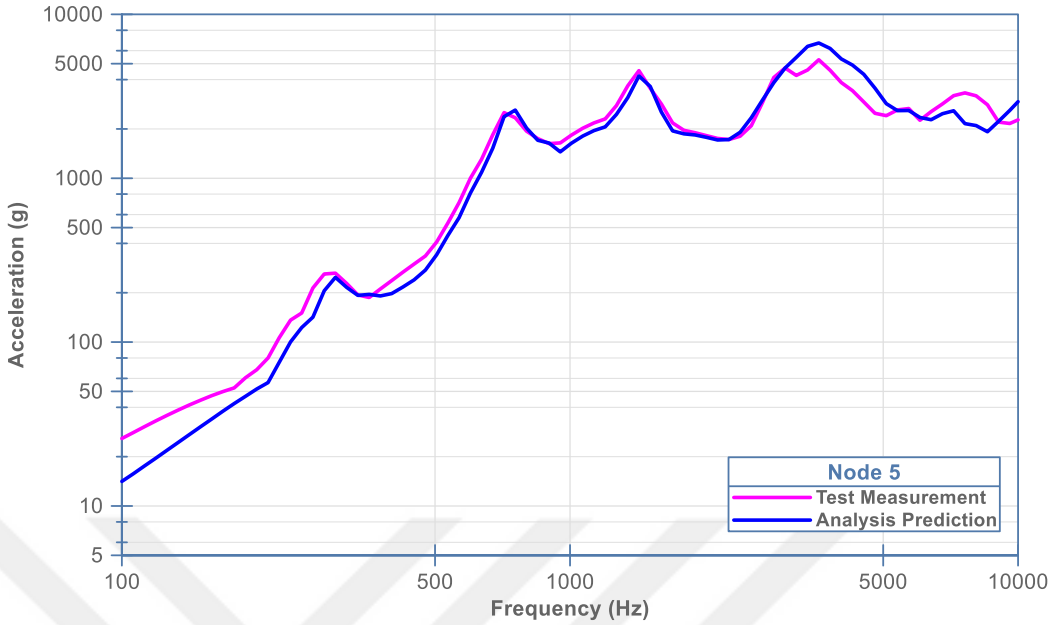


Figure 5.7. Comparison of the test and analysis results using 1000x1000x50 $mm^3$ plate excited from Node 1 without the mechanical filter at Node 5

Analysis predictions in all positions seem compatible with test results. Modal peaks are at the similar amplitude and frequency in test and analysis results. However, at initial frequencies, the analysis estimates seem to gradually decrease as move away from the impact location. Although the damping coefficient is defined with low values at those frequencies, the test levels could not be reached in regions far from the impact location. In addition, analysis predictions between 300 - 1500 Hz at the node 3 location seem to be low.

### 5.1.2 Comparison With Mechanical Filter

The results obtained in the case when ten layers of sheet paper were placed as a mechanical filter are shown in Figure 5.8 to Figure 5.12.

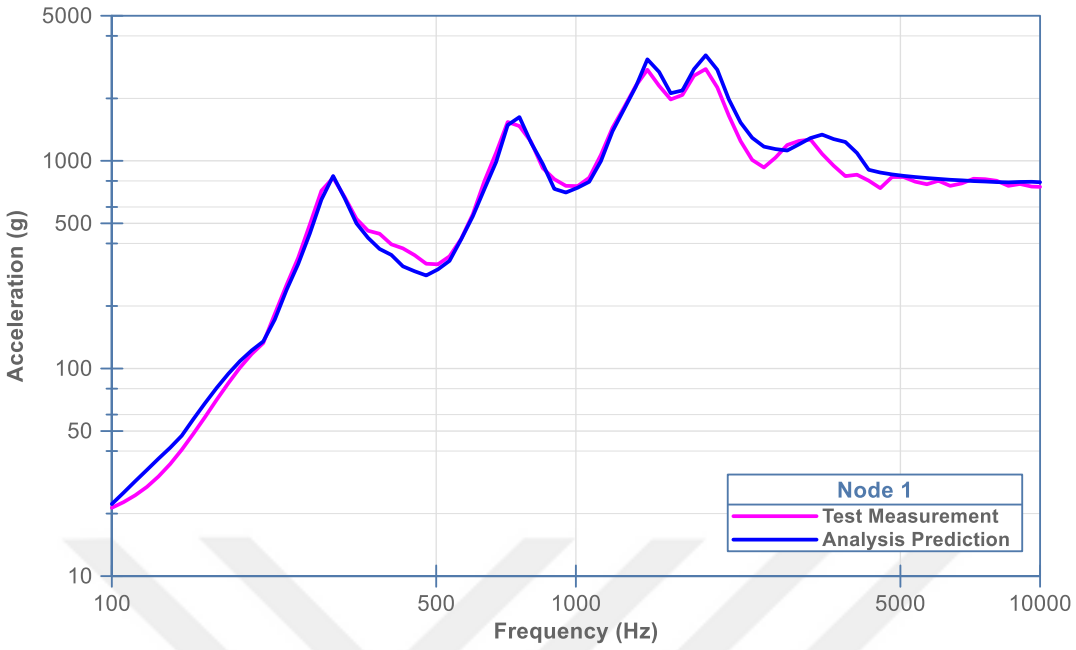


Figure 5.8. Comparison of the test and analysis results using 1000x1000x50 $mm^3$ plate excited from Node 1 with the mechanical filter at Node 1

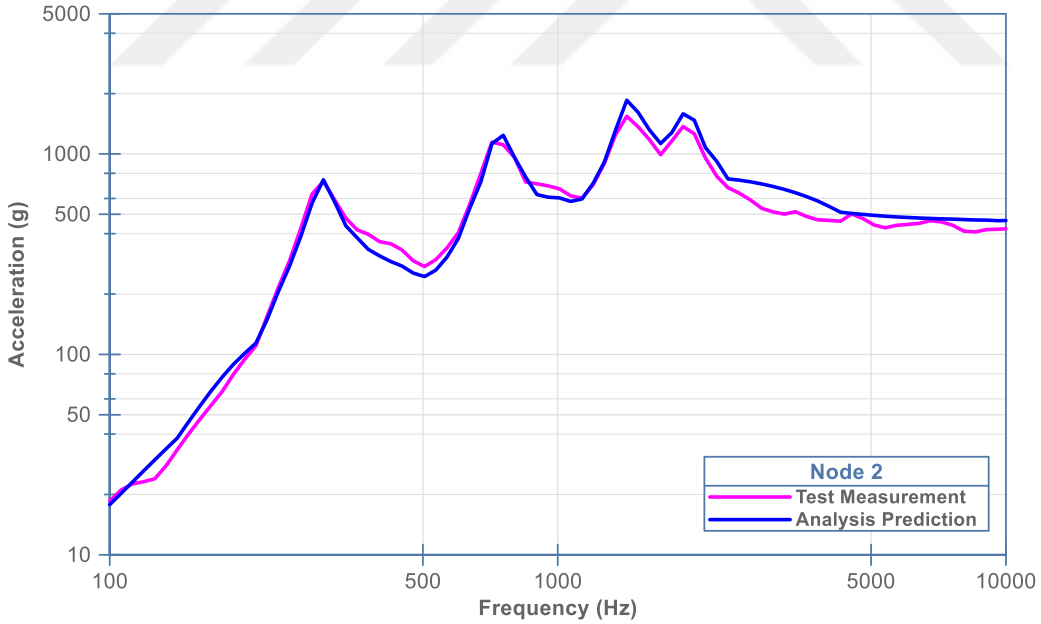


Figure 5.9. Comparison of the test and analysis results using 1000x1000x50 $mm^3$ plate excited from Node 1 with the mechanical filter at Node 2

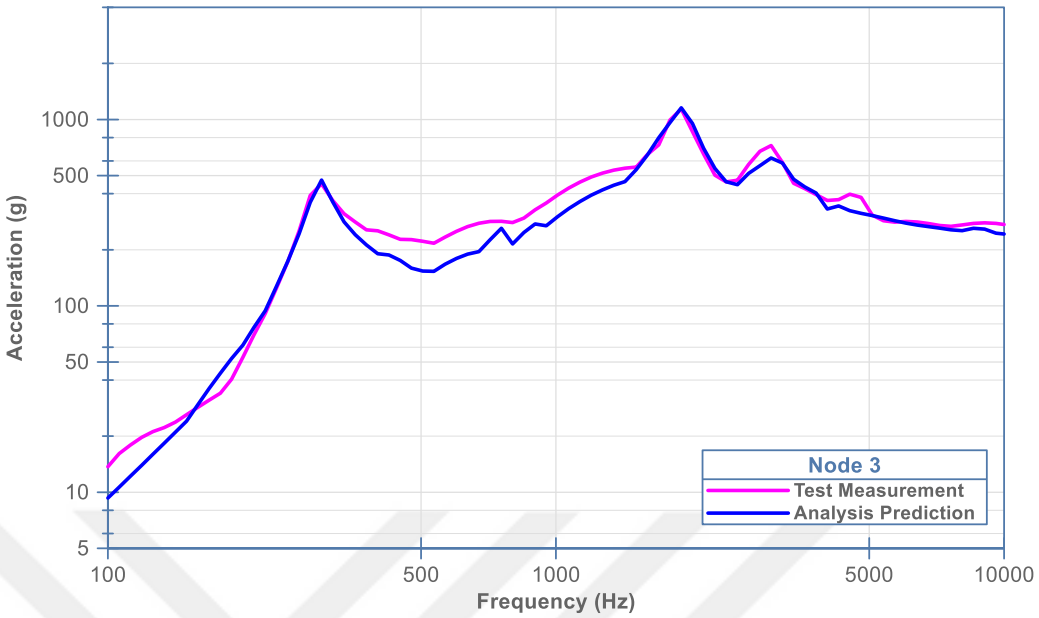


Figure 5.10. Comparison of the test and analysis results using 1000x1000x50 $mm^3$ plate excited from Node 1 with the mechanical filter at Node 3

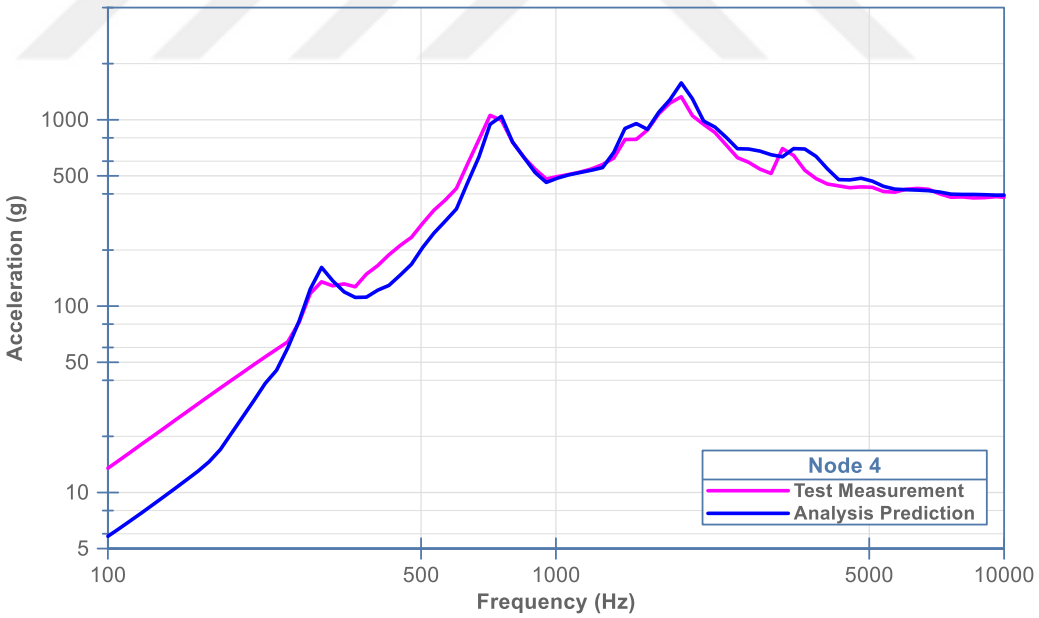


Figure 5.11. Comparison of the test and analysis results using 1000x1000x50 $mm^3$ plate excited from Node 1 with the mechanical filter at Node 4

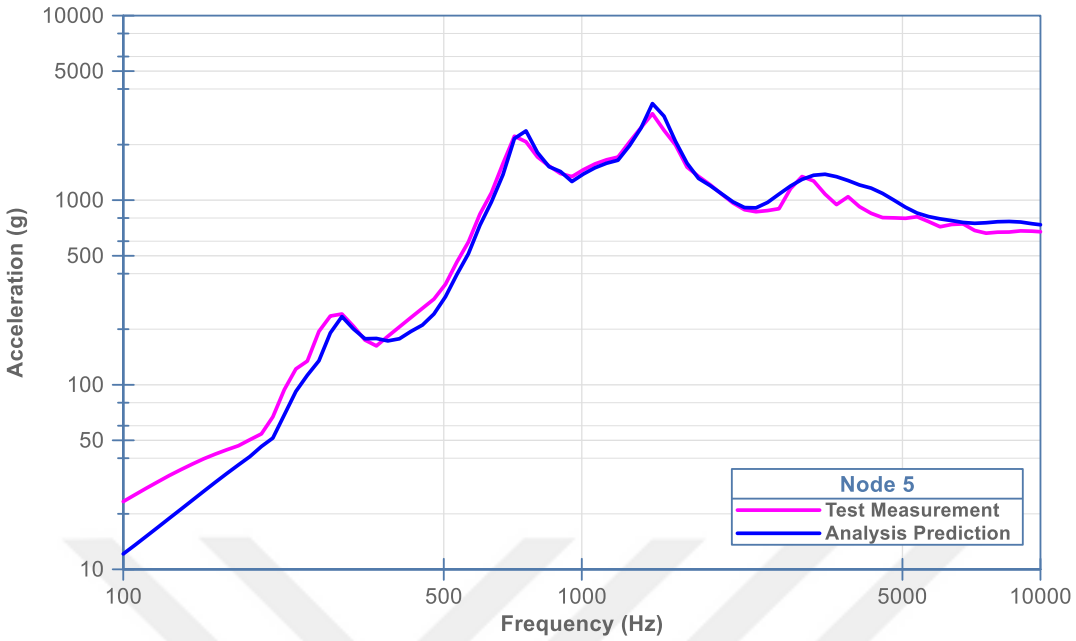


Figure 5.12. Comparison of the test and analysis results using 1000x1000x50 $mm^3$ plate excited from Node 1 with the mechanical filter at Node 5

The results are similar to Section 5.1.1 as the entire configuration is the same, except for the mechanical filter. Only the acceleration levels in the high-frequency region decreased due to the mechanical filter effect. The analysis and test results matched well in this high-frequency region.

## 5.2 Results with 1500x1000x30 $mm^3$ Resonant Plate

The test configuration is shown in Figure 5.13, and the FEA configuration is shown in Figure 3.4. Two different impact locations have been studied with this plate. In the first case, the impact from the Node 1 location in the middle of the plate and then the Node 6R location were examined. In all cases, the presence and absence of mechanical filter were investigated.

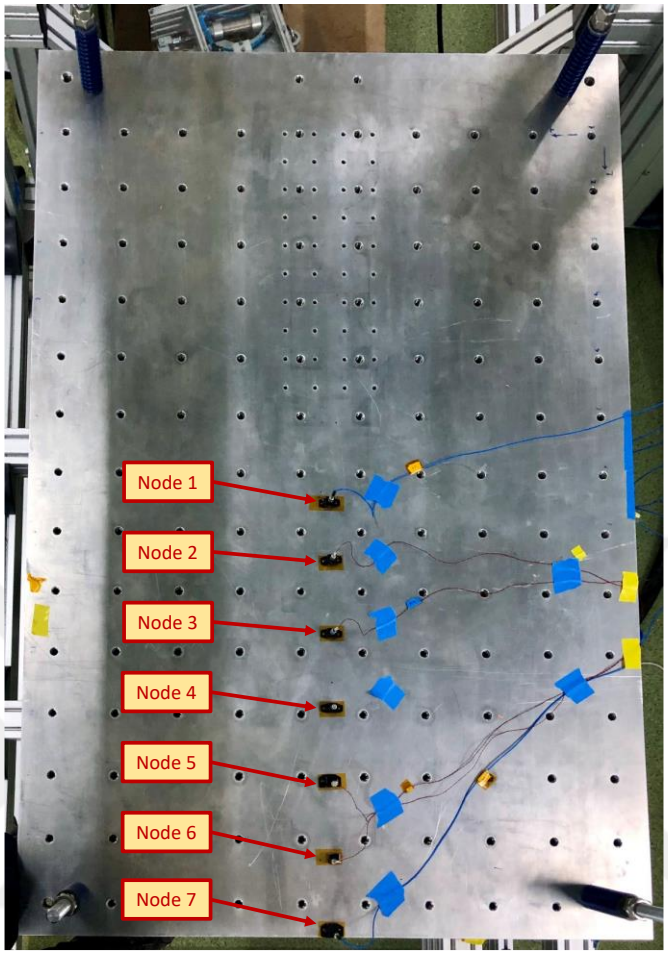


Figure 5.13. 1500x1000x30 $mm^3$ resonant plate pneumatic test system configuration (front view).

### 5.2.1 Impact From Node 1 Location

The resonant plate was excited from Node 1 with a 15 kg hammer, which has a speed of 1.74 $m/s$.

#### 5.2.1.1 Comparison Without Mechanical Filter

The results obtained in the absence of a mechanical filter are shown in Figure 5.14 to Figure 5.20.

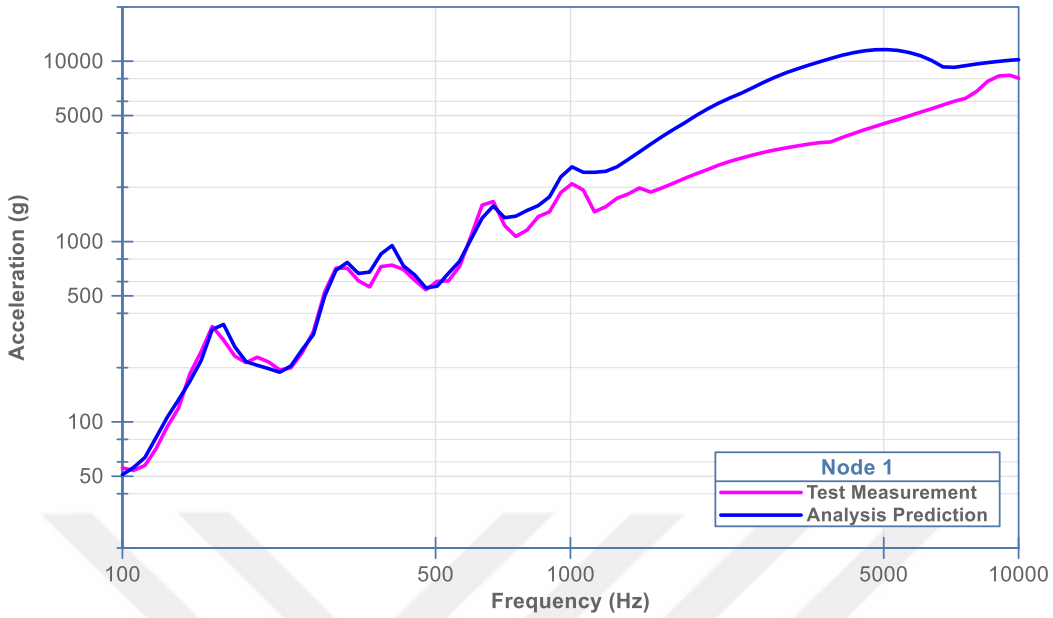


Figure 5.14. Comparison of the test and analysis results using 1500x1000x30 $mm^3$ plate excited from Node 1 without the mechanical filter at Node 1.

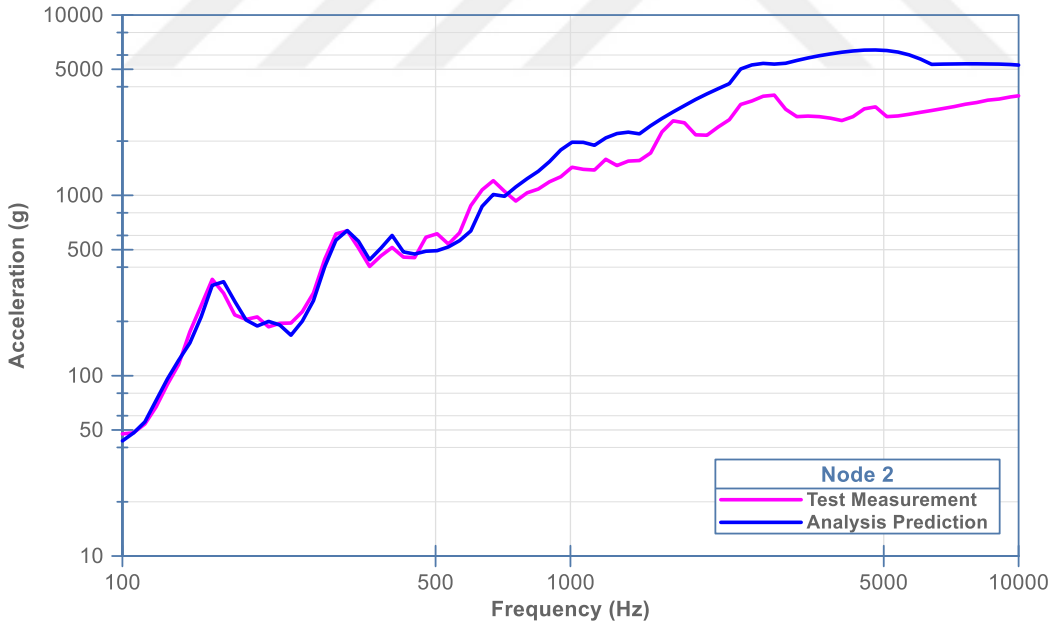


Figure 5.15. Comparison of the test and analysis results using 1500x1000x30 $mm^3$ plate excited from Node 1 without the mechanical filter at Node 2.

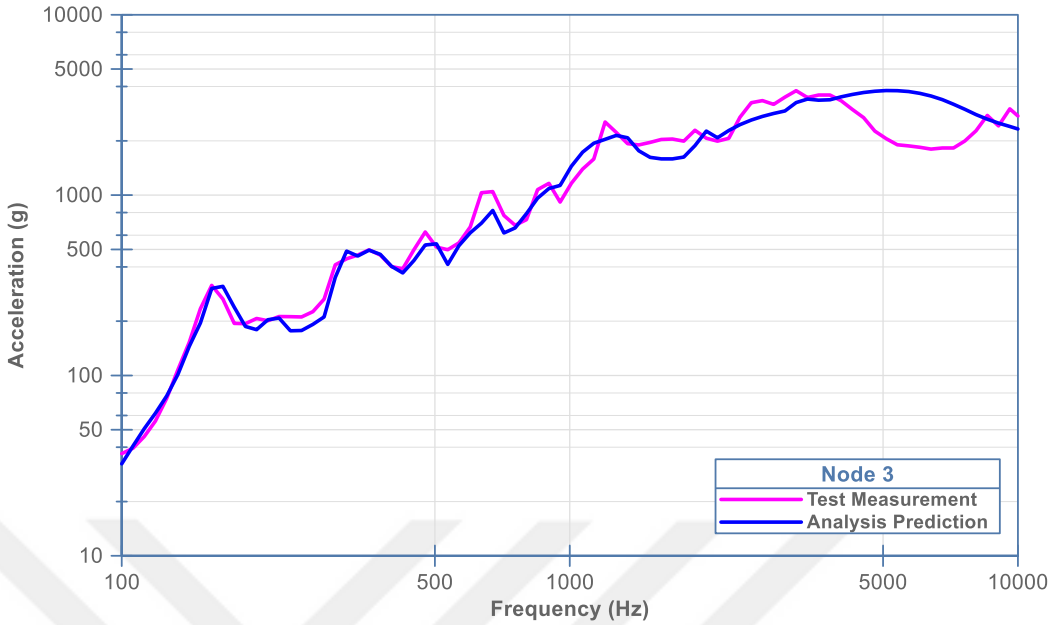


Figure 5.16. Comparison of the test and analysis results using 1500x1000x30 $mm^3$ plate excited from Node 1 without the mechanical filter at Node 3.

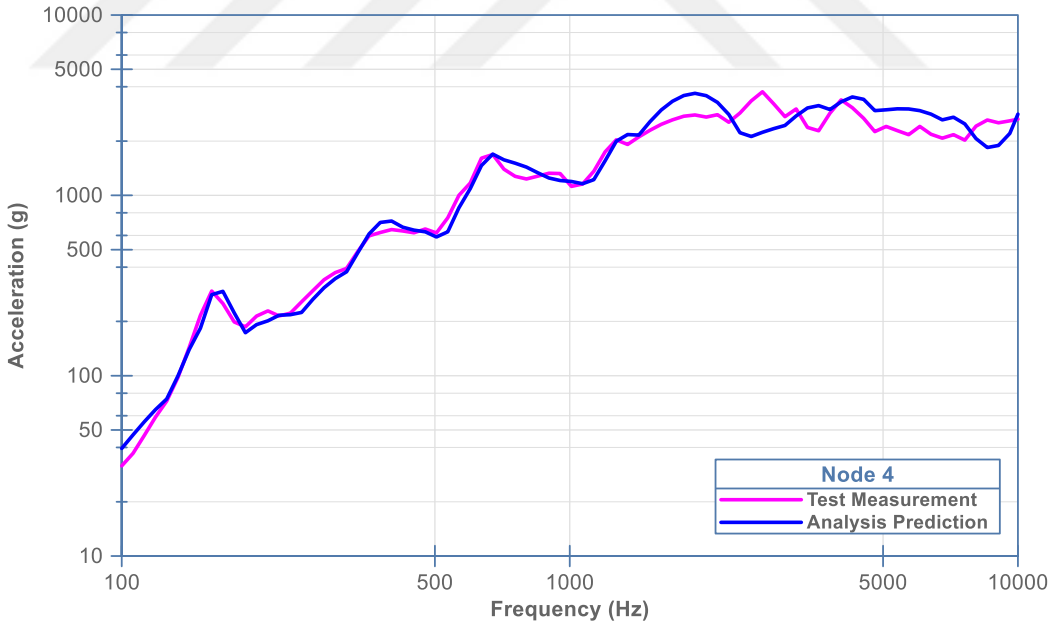


Figure 5.17. Comparison of the test and analysis results using 1500x1000x30 $mm^3$ plate excited from Node 1 without the mechanical filter at Node 4.

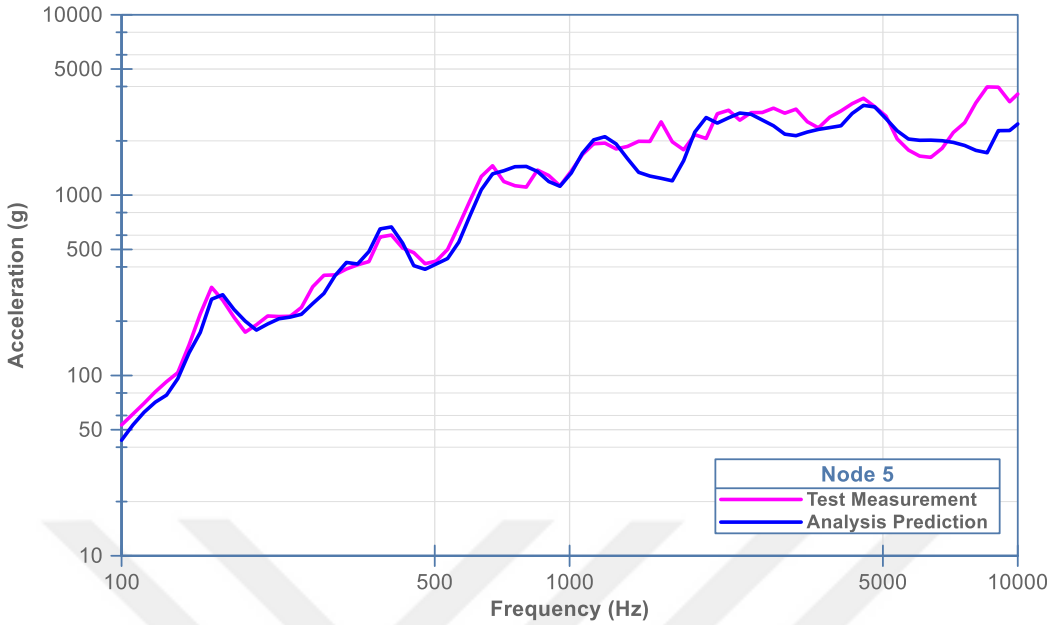


Figure 5.18 Comparison of the test and analysis results using 1500x1000x30 $mm^3$ plate excited from Node 1 without the mechanical filter at Node 5.

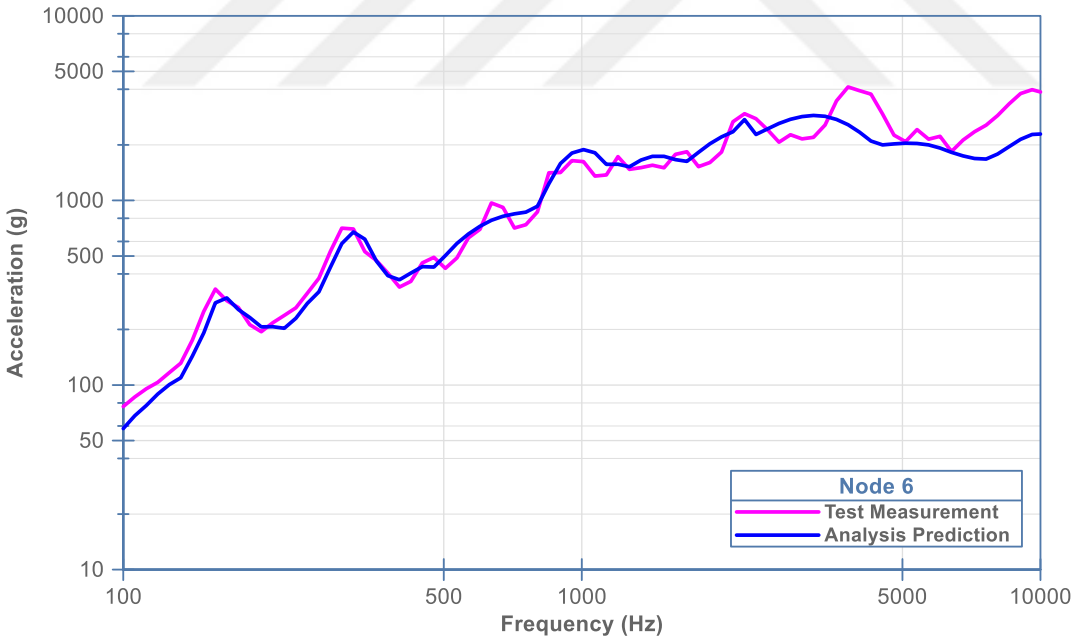


Figure 5.19. Comparison of the test and analysis results using 1500x1000x30 $mm^3$ plate excited from Node 1 without the mechanical filter at Node 6.

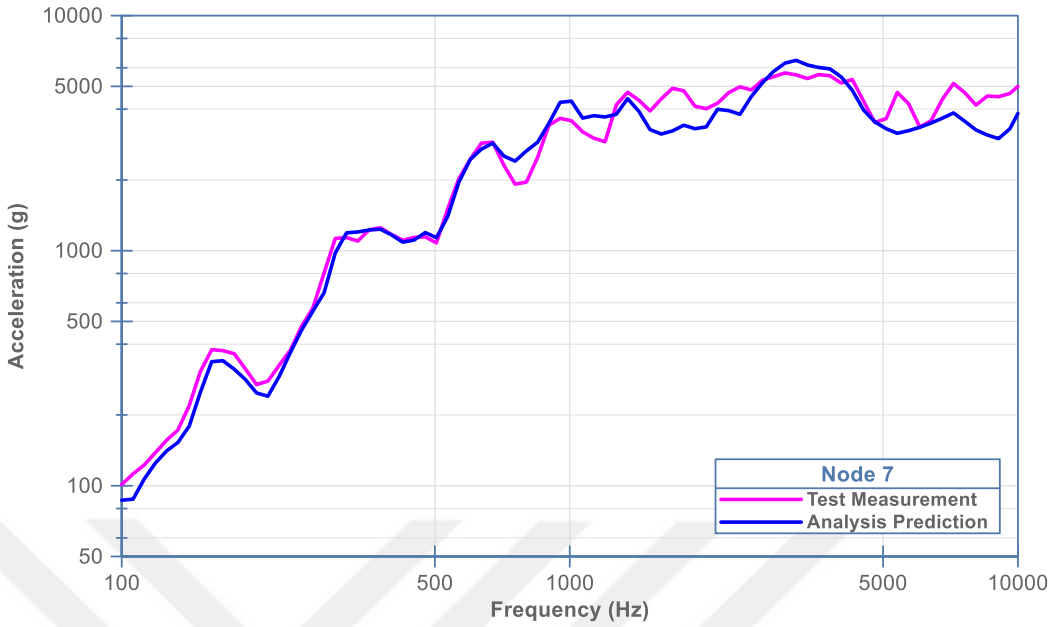


Figure 5.20. Comparison of the test and analysis results using 1500x1000x30 $mm^3$ plate excited from Node 1 without the mechanical filter at Node 7.

1500x1000x30 $mm^3$ plate, which is thinner and longer, shows a good approximation in analysis and test results. Modal peaks are generally matched. Also, unlike the 1000x1000x50 $mm^3$ plate in Section 5.1, the results appear to have a low error rate at points far from the impact location. However, the analysis estimates at high frequencies in the impact region in Figure 5.14 and Figure 5.15 remained higher than the test measurements. When this region is matched by changing the damping ratios, this time incompatible results are obtained at high frequencies at other locations. This situation arising in the thin plate needs to be worked on the optimization of damping rates. Since the test equipment is not placed in the impact zone, the damping ratio is chosen such that accurate results are obtained at regions further away from impact locations.

### 5.2.1.2 Comparison With Mechanical Filter

The results obtained in the case when 10 layers of sheet paper were placed as a mechanical filter are shown in Figure 5.21 to Figure 5.27.

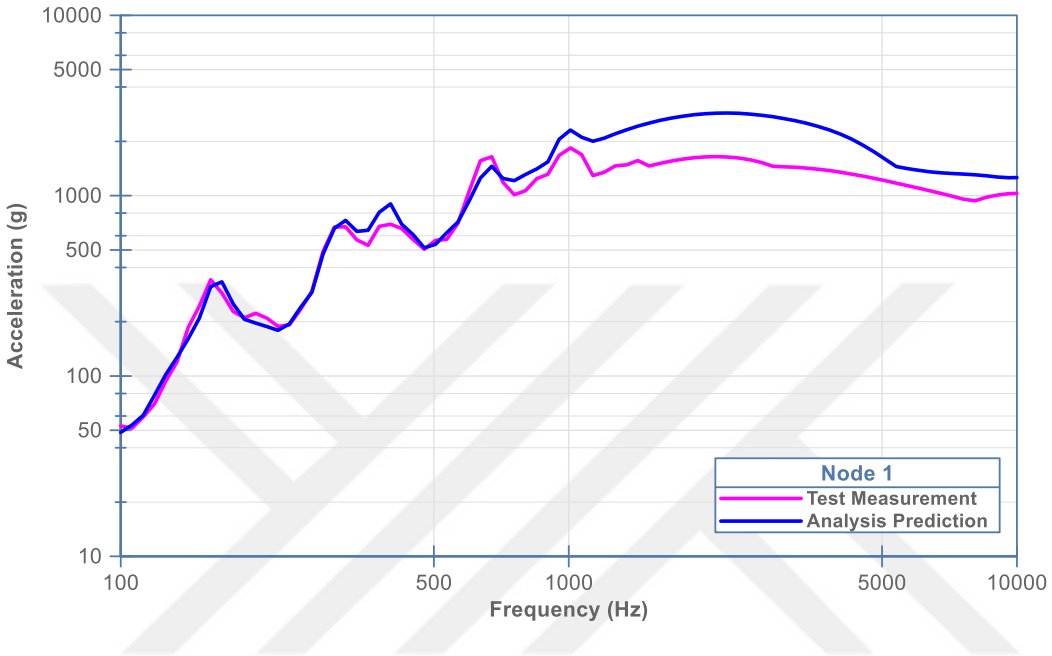


Figure 5.21. Comparison of the test and analysis results using 1500x1000x30 $mm^3$ plate excited from Node 1 with the mechanical filter at Node 1.

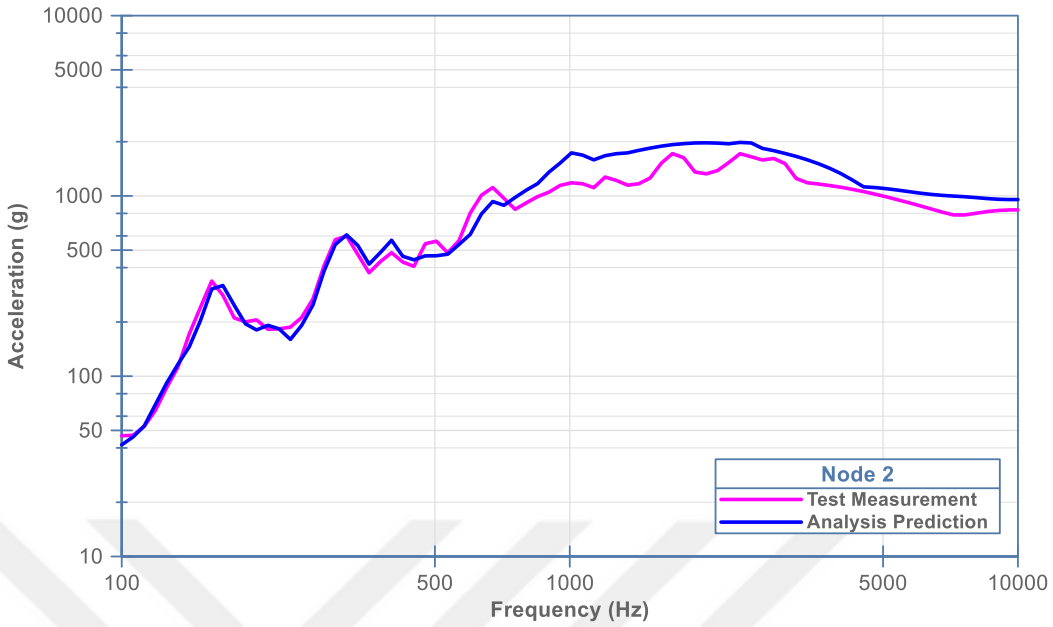


Figure 5.22. Comparison of the test and analysis results using 1500x1000x30 $mm^3$ plate excited from Node 1 with the mechanical filter at Node 2.

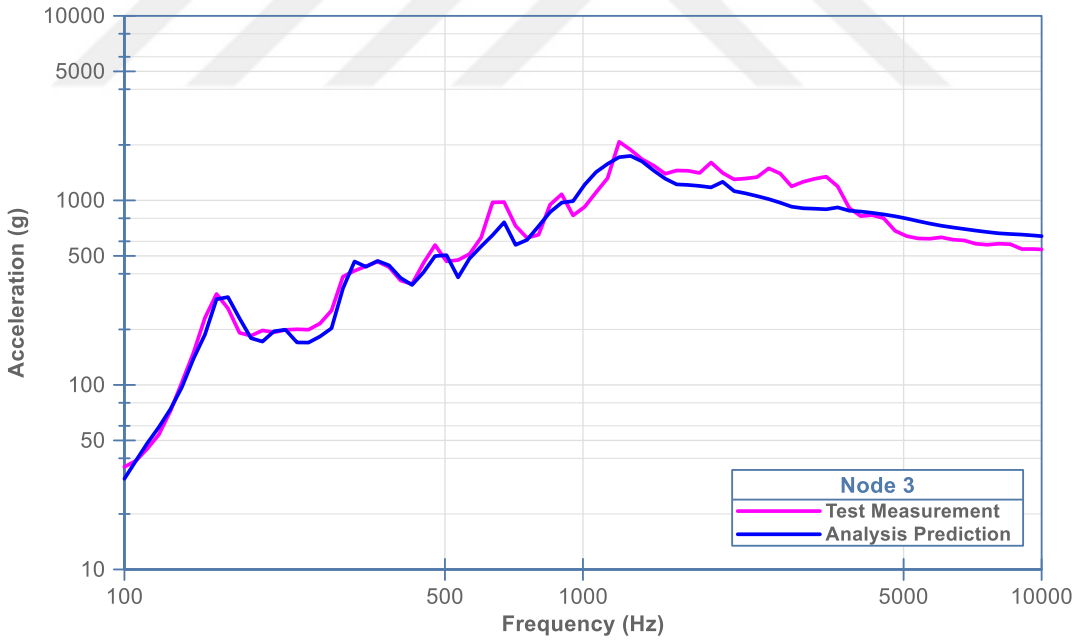


Figure 5.23. Comparison of the test and analysis results using 1500x1000x30 $mm^3$ plate excited from Node 1 with the mechanical filter at Node 3.

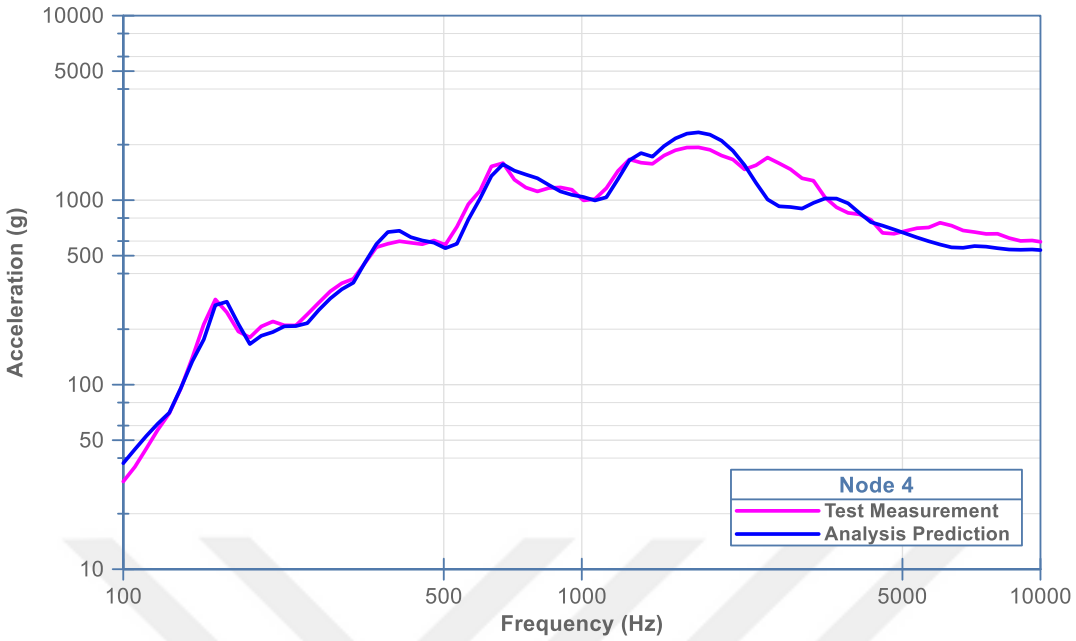


Figure 5.24. Comparison of the test and analysis results using 1500x1000x30 $mm^3$ plate excited from Node 1 with the mechanical filter at Node 4.

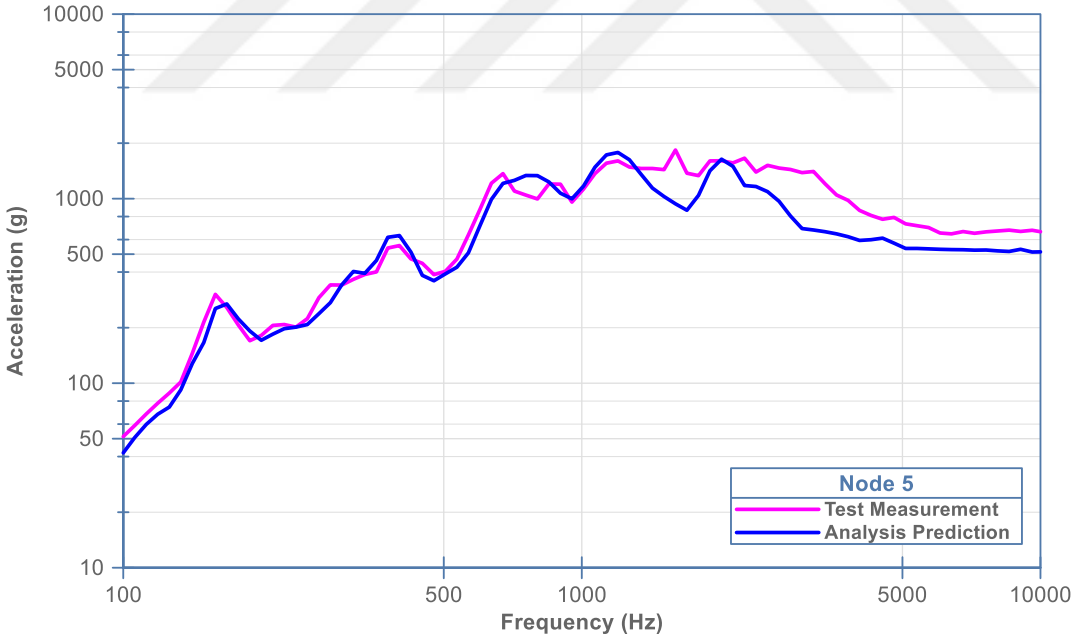


Figure 5.25. Comparison of the test and analysis results using 1500x1000x30 $mm^3$ plate excited from Node 1 with the mechanical filter at Node 5.

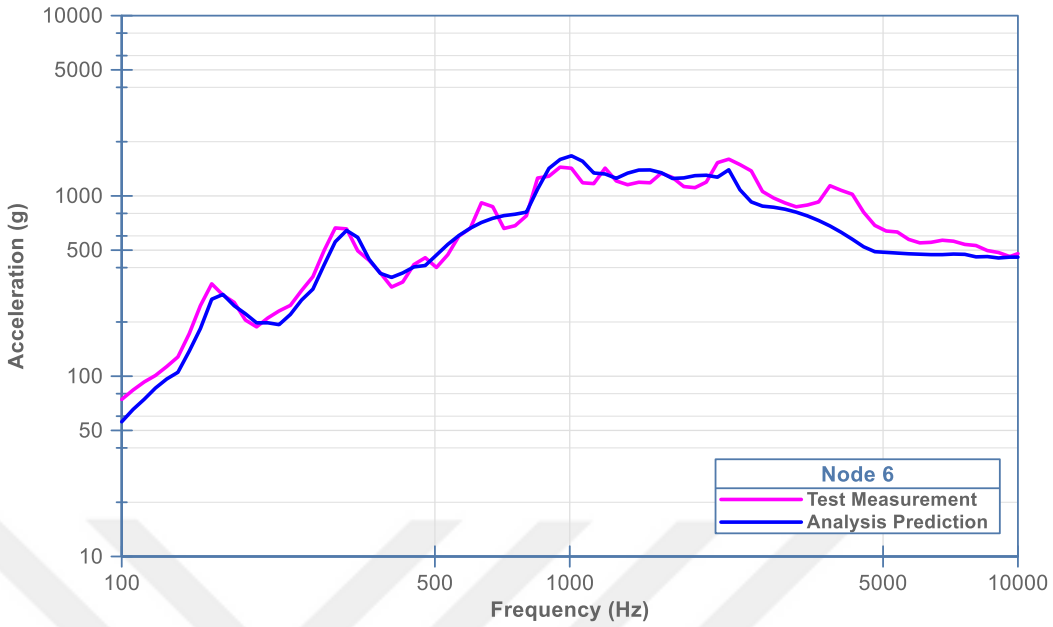


Figure 5.26. Comparison of the test and analysis results using 1500x1000x30 $mm^3$ plate excited from Node 1 with the mechanical filter at Node 6.

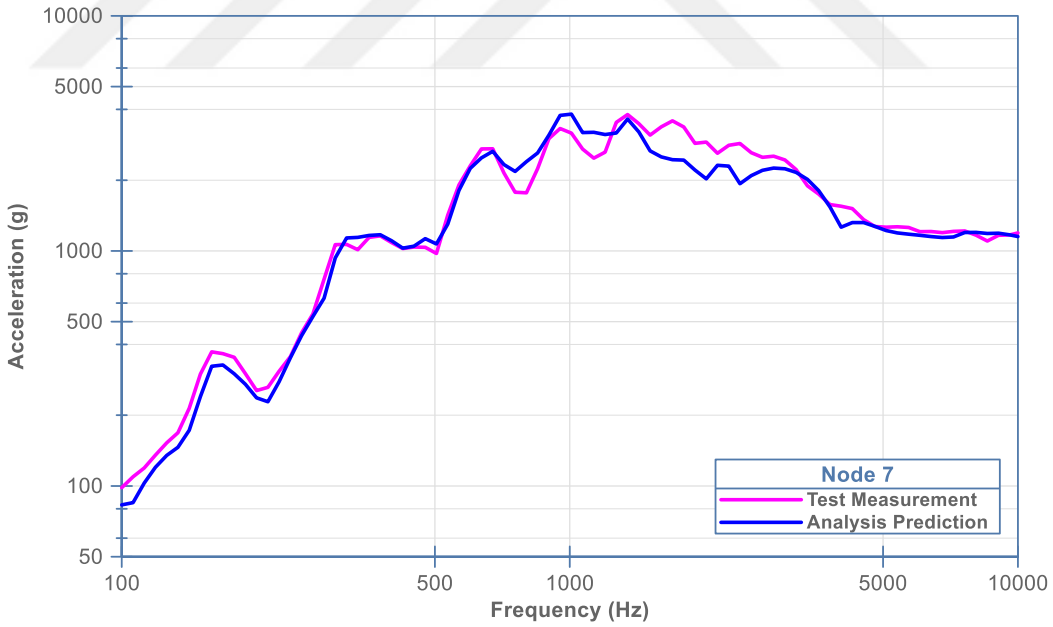


Figure 5.27. Comparison of the test and analysis results using 1500x1000x30 $mm^3$ plate excited from Node 1 with the mechanical filter at Node 7.

An attenuation at high frequencies was observed by using a mechanical filter apart from the results in Section 5.2.1.1. A good match was observed between analysis and test results.

### 5.2.2 Impact From Node 6R Location

The thinner and longer plate is excited from the point close to the edge, and it is aimed to observe the consistency between analysis and test results at the far points. The resonant plate was excited from the Node 6R with a 15 kg hammer which has a speed of 1.74 m/s.

#### 5.2.2.1 Comparison Without Mechanical Filter

The results obtained in the absence of mechanical filter are shown in Figure 5.28 to Figure 5.30.

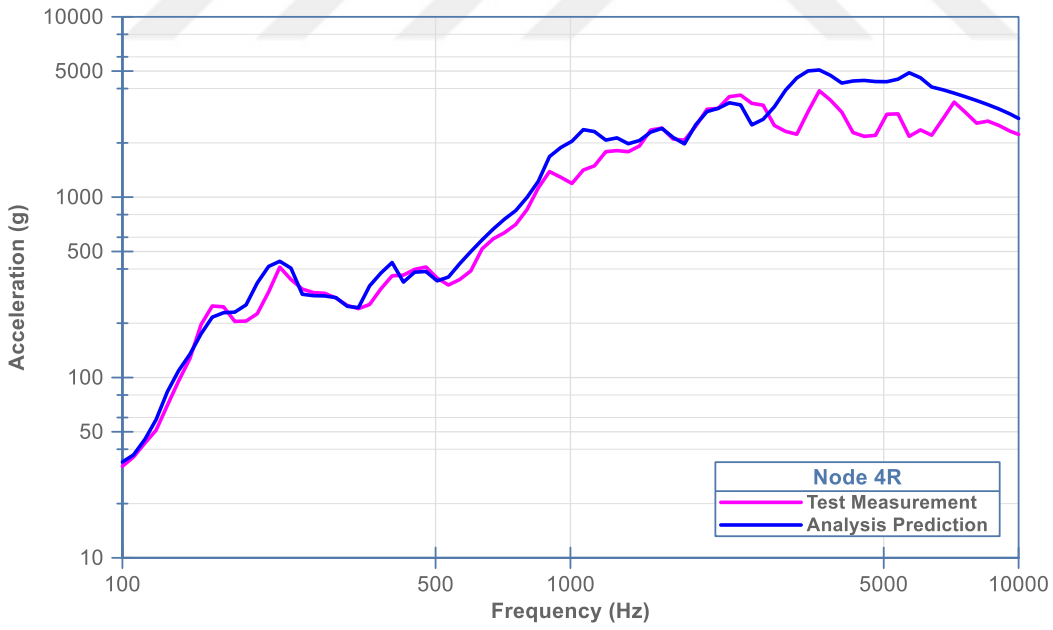


Figure 5.28. Comparison of the test and analysis results using 1500x1000x30 $mm^3$ plate excited from Node 6R without the mechanical filter at Node 4R.

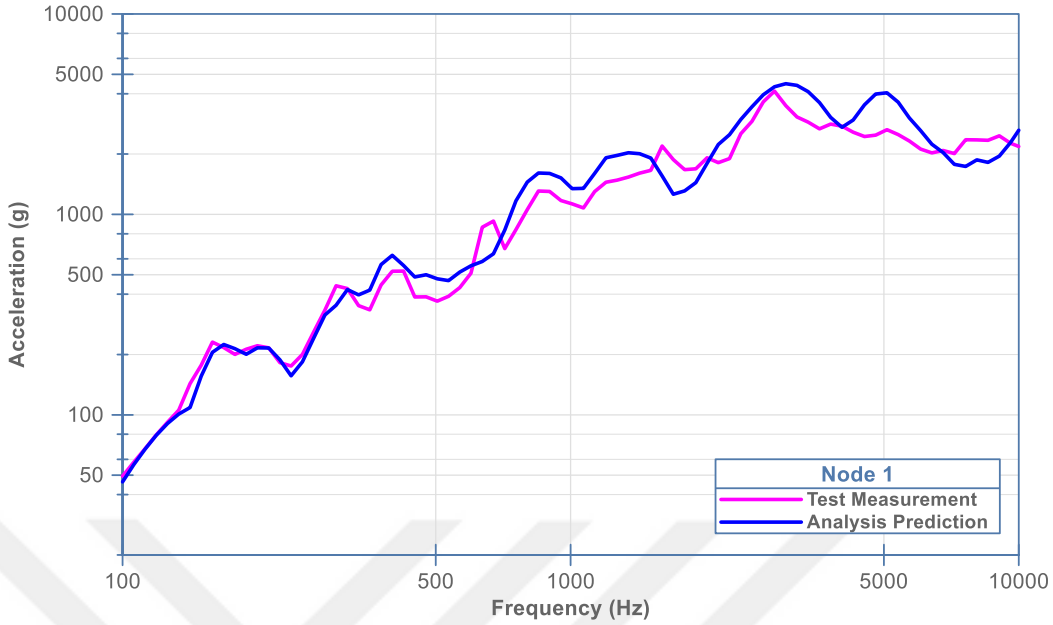


Figure 5.29. Comparison of the test and analysis results using 1500x1000x30 $mm^3$ plate excited from Node 6R without the mechanical filter at Node 1.

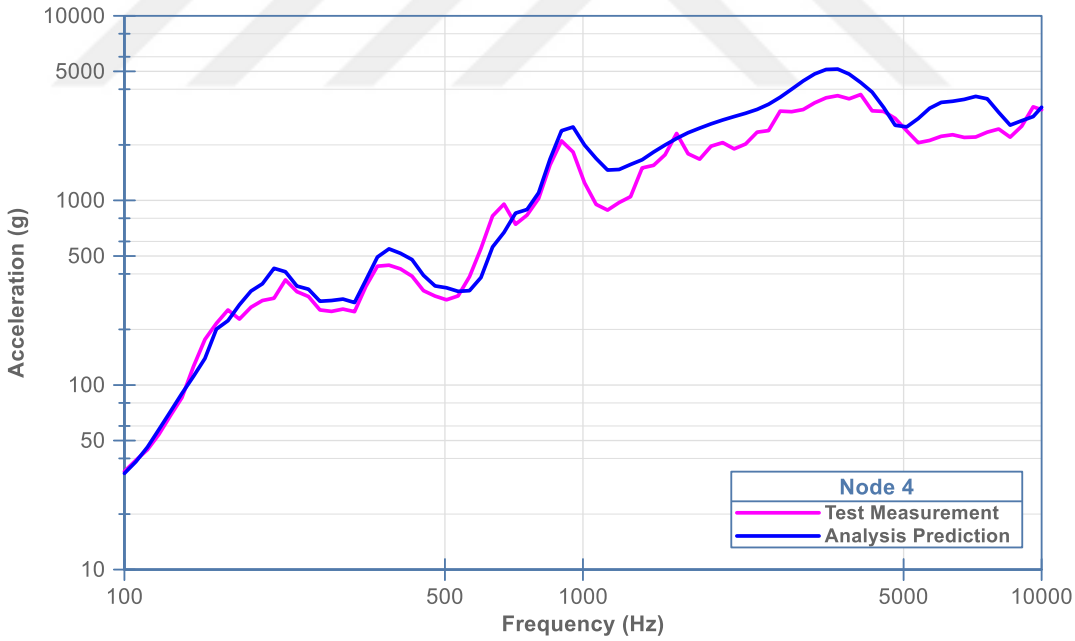


Figure 5.30. Comparison of the test and analysis results using 1500x1000x30 $mm^3$ plate excited from Node 6R without the mechanical filter at Node 4.

The match in the results was also observed in this case, although the analysis estimates remained higher after 1000 Hz. Greater damping rates should be defined in the analysis model for a better match.

#### 5.2.2.2 Comparison With Mechanical Filter

The results obtained in the case when ten layers of sheet paper were placed as a mechanical filter are shown in Figure 5.31 to Figure 5.33.

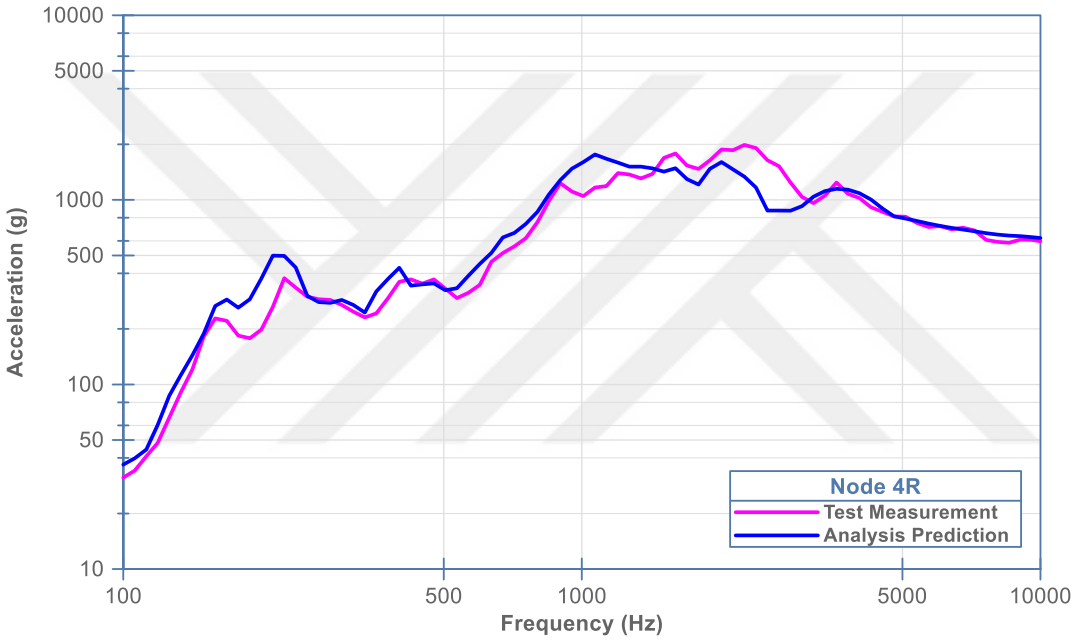


Figure 5.31. Comparison of the test and analysis results using 1500x1000x30 $mm^3$ plate excited from Node 6R with the mechanical filter at Node 4R.

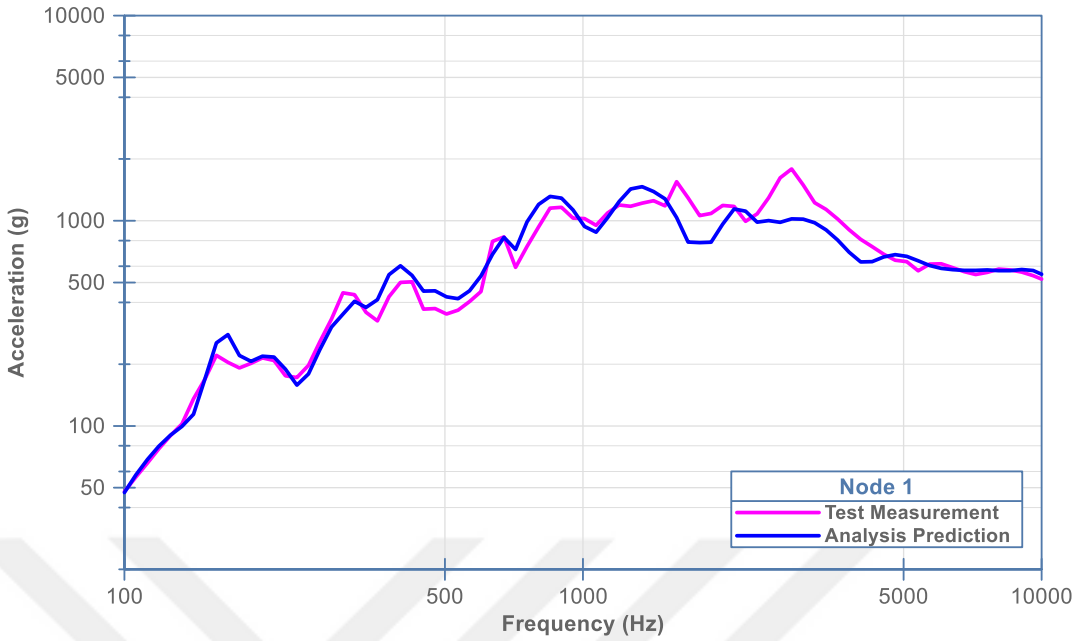


Figure 5.32. Comparison of the test and analysis results using 1500x1000x30 $mm^3$ plate excited from Node 6R with the mechanical filter at Node 1.

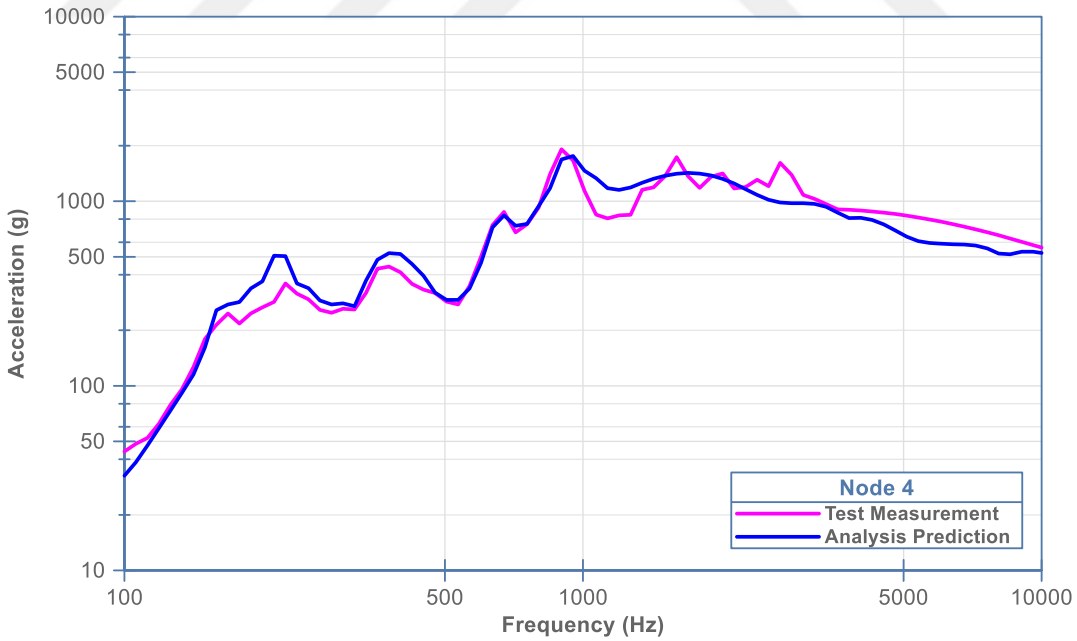


Figure 5.33. Comparison of the test and analysis results using 1500x1000x30 $mm^3$ plate excited from Node 6R with the mechanical filter at Node 4.

These results were obtained by adding the mechanical filter effect and more realistic damping rates to the analysis model of Section 5.2.2.1. In this way, similar values between analysis and test results after 1000 Hz were achieved. However, the analysis prediction is higher than the test measurement at the first mode (220 Hz). The damping rates should be increased.

In summary, choosing the correct force profile and appropriate FEM parameters was effective in the low error rates in the comparisons. Similar matches were obtained with the first analyses in the SRS modal peaks without damping ratios optimization. Minimal changes have been made by optimizing modal damping ratios.

# CHAPTER 6

# CONCLUSION

## 6.1 Conclusion

In this thesis, the pyroshock test system is numerically and experimentally investigated. The study starts with understanding the effects of shock test system parameters on SRS profile using the FEA, follows with the verification of these parameters in the experimental setup, and ends with a comparison of analysis and test results. In addition, a sample pyrotechnic shock source is tested, and the level of the shock is measured during its activating explosion. With this study, the shock profile that was actually tried to be simulated was observed. The strengths and weaknesses of the current resonant plate test method were evaluated in Section 4.3.

Firstly, the effect of test system parameters on the SRS and half-sine force profile was observed with the FEA model. Then the results were verified in the test facility. Some parameters such as hammer speed and hammer mass, whose effects were studied only on the SRS profile in the literature, were confirmed in this study. Besides, their effects on the impact half-sine force profile have also been investigated in this work. According to the studies made: Hammer mass changes the SRS slope, and the acceleration at the low frequencies increases with the addition of mass to the hammer. The hammer speed variation causes the increase or decrease of the entire profile. The thinning of the resonant plate enables the SRS profile to increase at all frequencies and shift the knee point slightly towards lower frequencies, while its thickening causes it to move to higher frequencies. The measurement location changes the SRS profile, but the trend of change is related to mode shapes of the plate. The SRS profile varies according to the dominant modes at that location. The impact location causes some modes of the plate to be excited more effectively. It has no easily traceable effect on the SRS profile. Consequently, the preparation process

for proper test configuration was shortened since the effect of test system parameters could be analyzed and learned through simulation.

The effect of the mechanical filter material on shock profiles is quite significant. This phenomenon can be seen from the results in Section 4.1. FEM modeling of these materials is considerably difficult. In this study, the effect of mechanical filter materials was directly reflected on the force profile, and those effects were successfully applied to the FEM model and verified in Chapter 5. In the literature, various mechanical filter materials are used in order to affect the high-frequency region of SRS. Commonly used materials are aluminum, rubber, hardboard, Delrin, etc. A remarkable novelty of this work is the use of sheet paper as a mechanical filter and allows precise control of higher frequencies by changing the number of layers. With the force sensor, the effect of the paper on the impact profile has been examined in detail. In fact, it provides the effect of different mechanical filters alone and allows more precise control of the impact profile. As a result, standard sheet paper can be used instead of supplying various mechanical filters.

Pyroshock behavior of equipment is usually examined by testing because there is no effective shock analysis method. However, analysis and test results are compared at specific locations with different resonant plates in Chapter 5, and numerical predictions show good agreement with test results. Here, the actual impact force profile has been implemented on the FE model. In this way, consistent and accurate results have been achieved with FE analysis. It has been observed that force measurement test data are essential for accurate modeling of the high-frequency regions of SRS in Section 4.1.2.2. In addition, correct element size, time interval, and damping rates are important for the proper modeling of the numerical shock simulation. Moreover, a shock analysis of space equipment could be performed with this approach by placing the equipment FE model on the resonant plate. Thus, the equipment could be analyzed at the preliminary design stage long before environmental tests, and its sensitivity to shock can be predicted.

As a result of this study, mechanical impact pyroshock test systems are well characterized, and a reliable finite element modeling approach is developed.

## 6.2 Future Work

In the future, a more accurate shock analysis of actual space equipment with the developed FE analysis approach can be performed. The numerical model can be verified using the test infrastructure. In addition, elastomer polymer materials can be studied as future work in order to dampen modal peaks formed due to the resonant plate characteristics. Thus, protective methods can be investigated for shock sensitive units. Another possible future work is related to the application of shock tests in one axis instead of three axes. The Pyroshock test is separately applied at three axes conventionally. In each axis, the test item is exposed to loads in cross directions due to its fixture's modal characteristics. It can be aimed to qualify the equipment in a single test by optimizing cross-directional loads in the fixture design.

## REFERENCES


[1] ESA-ESTEC, *Space Engineering Mechanical Shock Design and Verification Handbook, ECSS-HB-32-25A*, 1st ed. Noordwijk: ECSS Secretariat ESA Requirements and Standards Division, 2015.

[2] J. Binder, M. Mccarty, and C. Rasmussen, "Development of a Pyrotechnic Shock Simulation Apparatus for Space," *Am. Inst. Aeronaut. Astronaut.*, no. June, pp. 1–17, 2012.

[3] T. Irvine, "An Introduction To The Shock Response Spectrum," 2012.

[4] E. M. Jacobson, "Using Frequency Based Substructuring to Optimize Multi-Axis Resonant Plate Shock Tests," Michigan Technological University, 2019.

[5] S. J. Lee, D. H. Hwang, and J. H. Han, "Development of pyroshock simulator for shock propagation test," *Shock Vib.*, vol. 2018, no. Figure 1, 2018.

[6] D. H. Hwang, H. S. Park, and J. H. Han, "Development of a miniature point source pyroshock simulator," *J. Sound Vib.*, vol. 481, p. 115438, 2020.

[7] J.-B. Bernaudin, V. Cipolla, and P.-A. Grivelet, "Shock qualification methods for equipments," in *European Conference on Spacecraft Structures, Materials and Mechanical Testing 2005 (ESA SP-581)*, 2005.

[8] M. Jonsson, "Development of a Shock Test Facility for Qualification of Space Equipment," Chalmers University of Technology, 2012.

[9] S. Kiryenko, P. Gaetan, and J. Kasper, "ESA/ESTEC Shock Bench Presentation," in *European Conference on Spacecraft Structures, Materials and Mechanical Testing 2005 (ESA SP-581)*, 2005.

[10] E. Filippi, H. Attouoman, and C. Conti, "Pyroshock Simulation Using The Alcatel ETCA Test Facility," in *First European Conference on Launch Vehicle Vibrations*, 1999, pp. 1–12.

[11] J. Markl, "Analysis of a circular resonant plate for shock testing," Michigan Technological University, 2020.

[12] O. M. F. Morais and C. M. A. Vasques, "Shock environment design for space equipment testing," *Proc. Inst. Mech. Eng. Part G J. Aerosp. Eng.*, vol. 231, no. 6, pp. 1154–1167, 2017.

[13] N. Siam, M. Baunge, T. de Vutst, and R. Vignjevic, "Development of an efficient analysis method for prediction and structural dimensioning of space structures subjected to shock loading," Cranfield University, 2010.

[14] D. K. F. Ruess, B. Braun, “Equipment Shock Analysis for the Sentinel-3 Parabolic Mirror Assembly and Scan Assembly.” 2015.

[15] S. Jayaraman, M. Trikha, Somashekar, D. Kamesh, and M. Ravindra, “Response Spectrum Analysis of Printed Circuit Boards Subjected to Shock Loads,” in *12th International Conference on Vibration Problems, ICOVP 2015*, 2015, vol. 144, pp. 1469–1476.

[16] T. Kitamura, K. Yoshida, H. Seko, and Q. Shi, “Analysis of shock response for satellite separation,” in *International Conference on Noise and Vibration Engineering 2012, ISMA 2012, including USD 2012: International Conference on Uncertainty in Structure Dynamics*, 2012, vol. 3, pp. 2091–2101.

[17] SIMULIA, “ABAQUS User Assistance 2019, About dynamic analysis procedures,” 2020.

[18] SIMULIA, “ABAQUS User Assistance 2019,Transient modal dynamic analysis,” 2020.

[19] V. Giurgiutiu, *Structural health monitoring with piezoelectric wafer active sensors*, 2nd ed. Columbia: Elsevier Ltd, 2014.

[20] O. C. Zienkiewicz, R. L. Taylor, and J. Z. Zhu, “Plate Bending Approximation: Thin and Thick Plates,” *Finite Elem. Method its Basis Fundam.*, vol. 2011, pp. 407–466, 2013.

[21] T. Irvine, *An Introduction to Shock & Vibration Response Spectra*. 2013.

[22] A. J. Nathan and A. Scobell, *Harris’ Shock and Vibration Handbook*, vol. 91, no. 5. 2012.

[23] Siemens, “Shock Response Spectrum (SRS),” 2019. [Online]. Available: https://community.sw.siemens.com/s/article/shock-response-spectrum-srs#:~:text=4.1 SRS Calculations%3A Q-Factor,responds to a given input.

[24] ISO_Technical_Committee_GME/21, “Signal Processing - Part 4: Shock-response spectrum analysis, BS ISO 18431-4:2007,” *BS ISO Mech. Vib. Shock*, vol. 2, 2007.

[25] Kistler, “Instruction Manual Instruction Manual,” *Int. Bus.*, pp. 1–183, 2003.

[26] V. Mittal, M. N. M. Patnaik, S. S. Narayan, and D. Premkumar, “Development of Pyroshock Simulation Device (PSSD) for Spacecraft Application,” *J. Spacecr. Technol.*, vol. 29, no. July, 2018.

[27] N. Instruments, *NI PXIe-1073 User Manual*, no. February. 2011.

[28] N. Instruments, *PXIe-4480/4481 Dynamic Signal Acquisition User Manual*, no. October. Texas, 2016.

[29] Kistler, “Kistler Type 8743A... Accelerometers Specifications,” 2014. .

[30] Labview Sound and Vibration Measurement Help, “SVT Shock Response Spectrum VI,” 2018. [Online]. Available: https://zone.ni.com/reference/en-XX/help/372416L-01/sndvibtk/shock_resp_spec/#instance1.